

(NASA-D-155281) ADVANCED STIRLING RECEIVER  
DEVELOPMENT PROGRAM, PHASE 1 Final Report,  
Dec. 1988 - Jul. 1990 (Lockheed Sanders)  
119 p CSCL 10<sup>7</sup>

NP1-17452

Unclass

63/44 0332290

## NASA Contractor Report 185281

### Advanced Stirling Receiver Development Program

### FINAL REPORT - Phase 1

Charles A. Lurio  
*Lockheed Sanders Inc.*  
*Nashua, NH*

July 1990

Prepared for  
Lewis Research Center  
Contract NAS3-25471

**NASA**  
National Aeronautics and  
Space Administration



National Aeronautics and  
Space Administration

# Report Documentation Page

1. Report No. NASA CR 185281		2. Government Accession No.		3. Recipient's Catalog No.	
4. Title and Subtitle Advanced Stirling Receiver Development Program Final Report - Phase 1				5. Report Date 07/18/90	
7. Author(s) Charles A. Lurio				6. Performing Organization Code	
9. Performing Organization Name and Address Lockheed Sanders, Inc. 95 Canal Street Nashua, NH 03060				8. Performing Organization Report No.	
12. Sponsoring Agency Name and Address National Aeronautics and Space Administration Lewis Research Center Cleveland, Ohio 44135				10. Work Unit No.	
				11. Contract or Grant No. NAS3-25471	
				13. Type of Report and Period Covered Final 12/88 - 7/90	
				14. Sponsoring Agency Code	
15. Supplementary Notes Program Managers: Dovie Lacy & David Namkoong - Power Technology Division, NASA Lewis Research Center					
16. Abstract <p>Critical technology experiments were designed and developed to evaluate the Stirling cavity heat pipe receiver for a space solar power system. Theoretical criteria were applied to the design of a module for containing energy storage phase change material while avoiding thermal ratcheting. Zero-g drop tower tests, without phase change, were conducted to confirm that the bubble location required to avoid ratcheting could be achieved without the use of container materials that are wetted by the phase change material. A full scale TES module was fabricated, but not tested. A fabrication method was successfully developed for the sodium evaporator dome, with a sintered screen wick, to be used at the focal point for the receiver. Crushing of the screen during dome hydroforming was substantially reduced over the results of other researchers by using wax impregnation. Superheating of the sodium in the wick under average flux conditions is expected to be under 10K. A 2000K furnace which will simulate solar flux conditions for testing the evaporator dome was successfully built and tested.</p>					
17. Key Words (Suggested by Author(s)) Space Power Stirling Solar Receiver Heat Pipe Zero-g Fluids				18. Distribution Statement Unclassified - Unlimited	
19. Security Classif. (of this report) Unclassified		20. Security Classif. (of this page) Unclassified		21. No of pages	
				22. Price*	

# ***Advanced Stirling Receiver Development Program***

## **Final Report - Phase 1**

<b>List of Variables</b>	<b>vii</b>
<b>Chapter 1: Summary</b>	<b>1</b>
1.0 Summary	1
<b>Chapter 2: Introduction</b>	<b>3</b>
2.1 Program Background	3
2.2 Sander's Stirling Receiver Program	5
2.3 The Sanders Stirling Receiver Design	5
<b>Chapter 3: Stirling Heat Pipe Receiver Critical Technologies Issues</b>	<b>8</b>
3.0 Introduction	8
3.1 Critical Technology Issues	8
3.1.1 Thermal Ratcheting	8
3.1.2 Evaporator Dome Fabrication and Performance Testing	8
<b>Chapter 4: PCM Module Design and Testing to Avoid Thermal Ratcheting</b>	<b>12</b>
4.0 Introduction	12
4.1 Void Positioning to Avoid Ratcheting	12
4.2 Drop Tower Tests of Bubble Positioning	17
4.2.0 General Remarks	17

4.2.1 Theoretical Considerations	17
4.2.2 Test Equipment	18
4.2.3 Test Procedures	22
4.2.4 Test Results	22
4.3 Phase Change Material (PCM) Ratcheting Test	28
4.3.1 Module Design for PCM Test	28
4.3.2 Fabrication of PCM Modules	30
4.3.3 Test Equipment	33
4.3.4 Planned Operation of the Test Rig	36
<b>Chapter 5: Evaporator Dome (Heat Pipe) Fabrication and Test</b>	39
5.0 Purpose and Approach	39
5.1 Evaporator Dome Designs	41
5.1.0 General Remarks	41
5.1.1 Screen Wick Designs	43
5.1.1.1 Components	43
5.1.1.2 Characteristics	43
5.1.2 Electroformed Wick Design	46
5.2 Evaporator Dome Fabrication	46
5.2.1 Screen Wick Dome Fabrication	46

5.2.1.1 Application of Ni Layer on IN617 Plate	49
5.2.1.2 Stacking and Sintering of the Wick Layers	49
5.2.1.3 Impregnation of Wick with Paraffin	50
5.2.1.4 Hydroforming of Dome	51
5.2.1.5 Cutback of Wick	53
5.2.1.6 Dome Condition	57
5.2.1.7 Evaluation of Screen Wick Domes	57
5.2.2 Electroformed Wick	64
5.3 'Heat Pipe' Cylinder	66
5.3.1 Design and Construction	66
5.3.2 Estimation of Sodium Fill Requirements	71
5.3.3 Fill Technique Issues	78
5.3.3.1 General Considerations	78
5.3.3.2 Preparation for Filling	81
5.3.3.3 Filling and Sealing	82
5.4 Furnace	83
5.4.1 Requirements	83
5.4.2 Design Options	83
5.4.3 Selected Furnace Design	86
5.4.4 Instrumentation	91

5.4.5 Qualification Testing	92
5.4.5.1 Heat Balance of the Furnace	93
5.5 Planned Test Procedure	97
<b>Chapter 6: Conclusions</b>	<b>101</b>
<b>Appendix A: Letter on Electroforming Technique</b>	<b>102</b>
<b>Appendix B: Checklist for Furnace Startup</b>	<b>105</b>
<b>References</b>	<b>107</b>

## List of Variables

$A_1$	Phase Change Material (PCM) Module area exposed to heating in test rig
$A_2$	Interior area of PCM module test rig
$A_w$	Cross-sectional area of wire strand in a wick
$H_L$	Pressure head required to overcome flow resistance in wick
$M$	Wires/length in screen
$P_l$	Pressure in liquid
$P_v$	Pressure in vapor
$Q$	Power
$S_c$	Spacing between wire centers in wick
$T_v$	Vapor temperature
$T_w$	Wall temperature
$T_{sl}$	Temperature at solid-liquid interface
$T_{lv}$	Temperature at liquid-vapor interface
$\Delta T_{crit}$	Critical temperature rise in fluid for bubble nucleation
$\Delta T_{sp}$	Superheat across wick
$V$	Fractional volume of wire in a wick
$\dot{V}$	Flow Rate in wick
$b$	Width of plate
$d$	Wire diameter in a wick
$f$	Interleaving factor in a wick
$g$	Gravitational acceleration
$h$	Maximum wicking height, parameter in flow (permeability) test
$h_{fg}$	Heat of vaporization

$k$	Thermal conductivity
$k_l$	Liquid thermal conductivity
$k_w$	Wick thermal conductivity
$k_{em}$	Effective thermal conductivity across mesh and sodium
$q$	Power flux
$r$	Radius of curvature
$r_e$	Effective bubble radius
$r_n$	Nucleation site radius
$t$	Plate Thickness
$t_m$	Thickness of single or multiple layers (of common type) of screen
$\alpha$	Contact angle
$\alpha_0, \alpha_1$	Angles in flow permeability test
$\beta$	Parameter in plate stress formula
$\gamma$	Half of wedge angle in drop tower test modules
$\delta$	Sodium condensate layer thickness
$\delta_w$	Wick thickness
$\varepsilon$	Emissivity, wick porosity
$\varepsilon_1$	Emissivity of PCM module surface in test rig
$\varepsilon_2$	Emissivity of interior surface of PCM module test rig
$\theta$	Angle between wires in wick
$\kappa$	Permeability of wick
$\mu$	Dynamic viscosity
$\nu$	Young's modulus
$\nu_l$	Liquid kinematic viscosity
$\rho$	Radius ratio in generalized container (from Concus and Finn)
$\rho_l$	Liquid sodium density



$\rho_v$	Vapor density
$\sigma$	Surface tension, Stefan - Boltzmann constant
$\sigma_{max}$	Maximum stress in plate

## Chapter I

### Summary

#### 1.0 Summary

In an effort to develop high efficiency power sources for space missions beyond 1995, NASA has been reexamining thermal engine power conversion cycles, among these the Stirling engine. Under a previous program an advanced solar receiver concept (cavity heat pipe) was developed that incorporates several innovative design features. The main innovation was to conceive the receiver as a large, nearly isothermal sodium heat pipe. Two critical technology areas were identified as requiring detailed development and testing. These tests were to be developed and performed under the present program.

The first critical technology area considered was the potential for mechanical distortion of the thermal energy storage module containing the Phase Change Material (PCM) that stores heat for use during eclipse periods. Such distortion (thermal ratcheting) can arise when the increase of PCM volume upon melting is not accommodated. A wedge-shaped module was designed that should minimize the chances of thermal ratcheting. The second technology area was an improved means of transporting heat in the solar receiver to the working gas of the dynamic cycle. It was proposed to accomplish this by designing the entire interior surface of the receiver to be a heat pipe. The work concentrated on the hemispherical dome at the focus of the incoming solar energy. The convex side of this dome faces the interior of the receiver and must be capable of wicking and evaporating a sufficient supply of sodium to power the system without dryout and burnthrough.

A criterion was developed for placement of void space in the PCM modules to prevent thermal ratcheting. Theoretical analysis and drop tower testing were performed using single phase fluids to investigate module geometries that would promote the required void location. The results showed agreement with theoretical predictions. There is a good possibility of being able to meet the criterion, and of being able to do so without the need to resort to container materials that are wetted by the phase change material. Full scale modules were fabricated from Haynes 188 alloy with the intention of performing 200 melt-freeze cycles on the actual PCM under 1-g conditions. Redirection of the program due to cost and other technical issues prevented performance of these tests. It is believed that only zero-g experiments with the PCM will allow a final determination of the suitability of a particular module design.

Evaporator domes were designed that should exhibit sodium superheating of well under 10K at average solar flux conditions. A successful procedure was developed for fabrication of screen wicked domes using sintering and wax impregnation to prevent tearing and reduce compression of the screen during hydroforming. A three stage hydroforming process alternating with stress relief anneals allowed the required deformation of the Inconel 617 base plate alloy.

To evaluate the performance of the evaporator domes using liquid sodium required a major effort to design and build a heat source with sufficient flux and temperature

capability. An induction heated furnace was built and successfully tested to within 30K of the projected required temperature of 2000K. The furnace was also designed to allow observation of the concave surface of the evaporator dome as a safety measure and performance test during operation. Unfortunately, technical schedules and cost considerations also prevented the evaporator dome test from being carried out.

## Chapter II

### Introduction

#### 2.1 Program Background

Demand for greater electrical power for spacecraft systems has always been a difficult problem for the designer. Spacecraft users would ideally like to have a supply as convenient and seemingly endless as that available from ground-based power grids. Given the continuing reality of exorbitant costs of transport to Low Earth Orbit (LEO), such ideals are not easily achieved. Instead, the emphasis has been on minimization of power requirements and power system mass to accomplish a given mission. Another strong emphasis has been on absolute maximization of reliability, even if at the cost of some increased mass. One manifestation of this is the 'no moving parts' philosophy. Thus, solar photovoltaic arrays have always been chosen over thermal engine cycle systems, though the latter have the potential for significant improvements in efficiency.

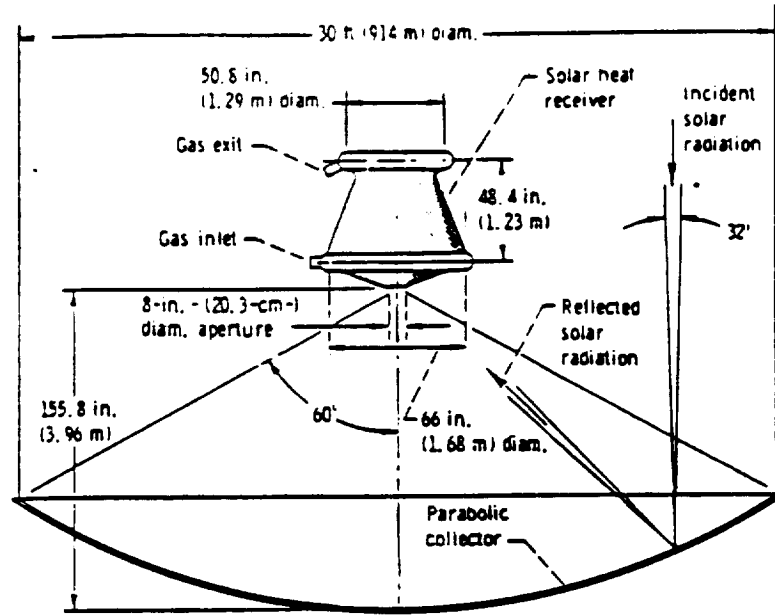
Thermal engine cycles were actually the original systems considered to provide spacecraft power, well before the first Sputnik was launched in 1957, for the simple reason that photovoltaics had not yet been developed (Ref. 1). The early, low efficiencies of solar cells motivated both NASA and the Department of Defense (DoD) to carry out extensive research on thermal engine systems in the early 1960's under the Sunflower and ASTEC programs respectively (Ref. 2).

Similar programs continued through the 1960s. Two important issues were to develop a thermal engine operating at high temperature (for high efficiency while avoiding low temperature, high mass radiators) and a solar receiver capable of fulfilling heat transfer and energy storage requirements.

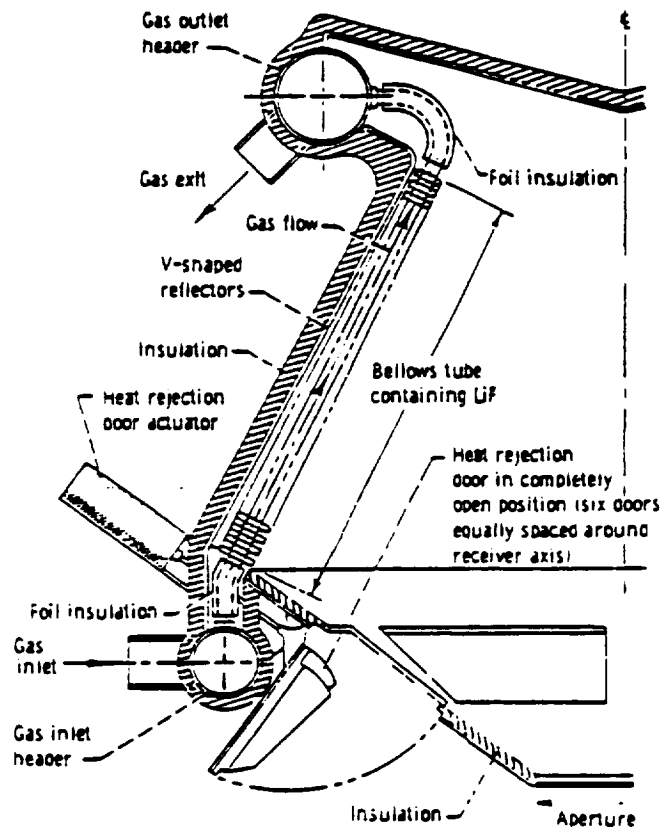
Energy storage for the thermal engine cycle presents both a unique problem and a unique opportunity. As in any other system operating in LEO, it will experience eclipse periods lasting about one-third of each orbit. Photovoltaic systems have used heavy, inefficient batteries to provide spacecraft power during these periods, but this approach should be avoided with the thermal engine, which is apt to wear out more quickly with many start/stop cycles. It was recognized early that a concept which provided a good 'fit' to the thermal engine was that of using a Phase Change Material (PCM) in the receiver that would store energy as its heat of fusion. Such materials avoid the battery storage step and, (depending on the degree of receiver insulation) will provide storage efficiencies of 80-90% or more. The melting point of the selected PCM sets the peak temperature of the thermal engine cycle.

By 1971 NASA had constructed a prototype solar receiver for a Brayton power cycle out of Nb-1Zr alloy, incorporating gas flow tubes along the walls, each surrounded by a jacket of LiF (melting point 1121K) PCM (Figure 2.1, Ref. 3). An accordion type geometry and a tapered quantity of LiF were used to prevent PCM shifting and accommodate the temperature rise of the gas flowing along the tube. Unfortunately, the program was cut short after only limited testing had been performed (Ref. 4).

Little additional work was done on spacecraft thermal engine systems until the early



(a) Solar heat receiver, solar collector combination.



(b) Solar heat receiver cross section.

ORIGINAL PAGE IS  
OF POOR QUALITY

Figure 2.1 Solar Brayton System, LiF Storage (Ref 3)

1980s. The revival was spurred by renewed work on space station concepts. With power requirements of tens of kilowatts and up, the efficiency advantage of the thermal cycles again became attractive. Of particular interest was that thermal cycle solar collector areas would be substantially smaller than those of photovoltaic systems. As a consequence, requirements for fuel to compensate for atmospheric drag on the station could be substantially reduced.

In this recent work on thermal engine systems, NASA's Lewis Research Center has concentrated its efforts on Brayton and Stirling engines and the receivers required to accommodate them. Though some work has been performed to increase the peak cycle temperature by examining a higher melting point PCM (Refs. 5,6), concern about engine alloy capabilities has led to the selection of  $\text{LiF-CaF}_2$  (melting point approx. 1040K) as the baselined storage medium.

NASA's studies of a solar receiver for the space station were based on a conservative design to ensure that it would work without requiring an extensive development program. This conservatism incurred some penalties, such as a relatively high receiver mass. To develop alternative designs that would prevent these penalties while retaining the reliability of the space station receiver design, NASA contracted an effort under the Advanced Heat Receiver Conceptual Design Study (AHRCDs). This contract was awarded to Lockheed Sanders (then known as Sanders Associates, Inc.) and was performed over the period March 1986 - July 1988.

## 2.2 Sanders's Stirling Receiver Program

From the early 1970's onward, Sanders designed and constructed a series of solar thermal engine receivers for terrestrial use under both internal and Department of Energy (DoE) funding. This experience was applied to the development of alternative receiver concepts for both Brayton and Stirling engines under the AHRCDs. Subsequently, NASA awarded to Sanders the follow-on Advanced Stirling Receiver Development Program (ASRDP), a projected four year effort to develop and construct a  $40\text{kW}_t$  ( $7\text{kW}_e$ ) Stirling engine receiver based upon the selected alternative.

The ASRDP is comprised of two phases. The first phase consisted of two tasks; the second of three optional tasks which were to be exercised at NASA's discretion. Unfortunately, technical and programmatic problems led to the cancellation of the work before completion of the first phase. The primary problems were that the cost of, and unforeseen difficulties in, developing the critical technology research for the receiver had been consistently underestimated. Nonetheless, the present author believes that valuable technical contributions have been made.

## 2.3 The Sanders Stirling Receiver Design

The Stirling receiver design developed under the AHRCDs was the basis for the effort performed under the current ASRDP and is briefly discussed below. A full description of the design details is contained in the final report of the AHRCDs (Ref. 7).

Figure 2.2 illustrates a cutaway view of the cavity heat pipe receiver. (Relative dimensions are not necessarily accurate. (The PCM modules are referred to in the figure as Thermal Energy Storage (TES) modules.) The first feature to note is that

# Cavity Heat Pipe Stirling Receiver

WITH FINNED TUBE/SHELL HEATER HEAD

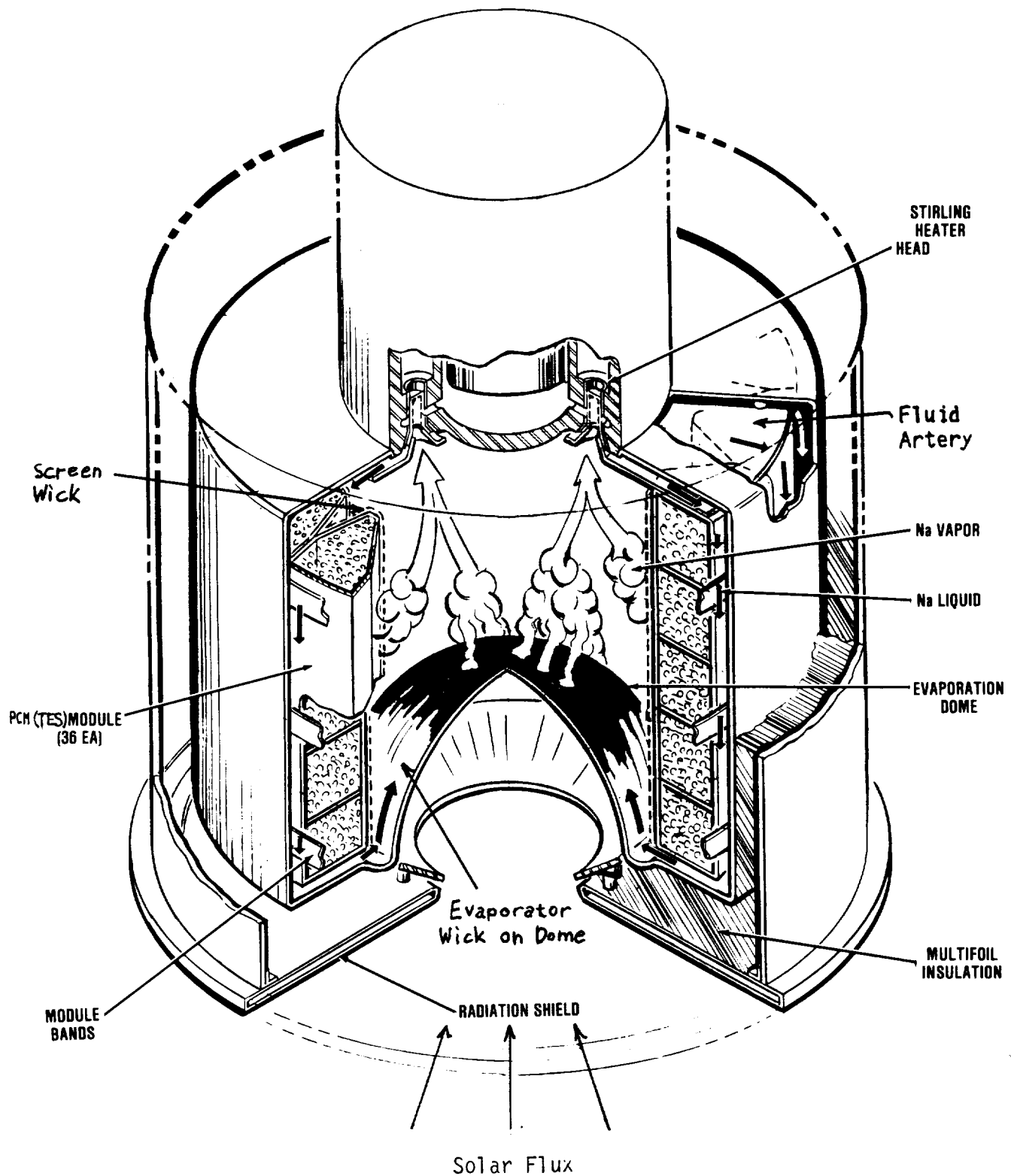


Figure 2.2 Cross-Section Cavity Heat Pipe Stirling Receiver

the receiver cavity is a closed container forming a heat pipe. Sodium is used to transport energy, and is present both as a liquid and as (ideally) the only component of vapor within the cavity. Wicking material, baselined as a screen mesh, covers all surfaces of the core chamber cavity, where it constrains the liquid to be in contact with the surfaces and to transport it to heat transfer surfaces. Areas that have even a slightly higher temperature than others will have a locally higher vapor pressure of sodium, which will evaporate off and carry the excess heat to cooler parts of the chamber. This tendency toward isothermal surfaces provides greater flexibility in the design, since the Stirling heater head and PCM modules need not be in direct contact with each other or constrained to a particular geometry and location by the solar flux distribution produced by the collector optics. Effectively the solar distribution has been relocated to the simpler geometry (yet still challenging design problem) of the evaporator hemisphere. The result is that a more compact, less massive receiver is possible.

During insolation, sunlight impinges on the concave surface of the receiver dome. Sodium flowing within the wick of the dome evaporates off the surface and condenses on both the engine heater head and the PCM modules, providing sufficient power to operate the engine and melt the storage material simultaneously. Condensate from the heater head tubes is wicked into an artery (annulus) behind the PCM modules, flows 'down' and 'under' the modules by capillary action, and is finally wicked into the screen covering the evaporator dome to repeat the cycle. Similarly, sodium condensing on the PCM modules flows through screen wicks between these modules, into the annular artery and onto the dome.

When the receiver enters eclipse, the dome cools and the PCM modules become the hottest surfaces in the chamber, evaporating off a net positive supply of sodium onto the heater head tubes as the storage material freezes. The liquid sodium condensing on the tubes is once again wicked into the annular artery, but this time flows out onto the module surfaces to supply the evaporation. Some sodium will also condense onto the dome (which is losing heat by radiation to space) and may be drawn back into the annulus to add to the supply for evaporation from the PCM modules.



## Chapter III

### Stirling Heat Pipe Receiver Critical Technology Issues

#### 3.0 Introduction

Although the previously designed Sanders solar receiver had several attractive innovations, it also presented a number of design challenges. The objective of the Phase I effort of the ASRDP was to develop and perform experiments to examine certain critical technology issues associated with the cavity heat pipe receiver.

#### 3.1 Critical Technology Issues

##### 3.1.1 Thermal Ratcheting

One of the difficulties that arises during cyclic testing of a thermal energy storage material is the phenomenon of thermal ratcheting (Ref. 8). This is a consequence of the density change of a substance when changing phases, and is illustrated schematically in Figure 3.1. When the material melts, the liquid formed takes up a larger volume than the solid, and must be able to expand into a void space. If such a void space is not available, high stresses will be built up in the adjacent container wall and cause wall distortion. This distortion can accumulate with each thermal cycle; thus it is called a 'ratcheting' effect. The volume changes that occur on melting can be substantial. For example, LiF undergoes about a 30% increase in volume (Ref.8) while the LiF-CaF<sub>2</sub> eutectic assumed here expands by about 26% (Ref. 9).

Besides selecting a substance with little or no volume change on melting -- an option that was beyond the scope of the present study -- there are at least two possible approaches to alleviating this problem. One is just to increase the gauge or strength of the container until it can cope with phase-change induced stresses without distortion. This may mean that the liquified PCM will cause stress sufficient to break through the adjacent, still solidified material. The penalty to this approach is the increased mass of container material.

The second approach is to design the container so that the zero-g void location will provide an escape path for the melting PCM. This was the course taken in this program. Moreover, by providing near-isothermal heating of the PCM modules, the cavity heat pipe design should improve the chances of providing such an escape path.

##### 3.1.2 Evaporator Dome Fabrication and Performance Testing

The evaporator dome must be able to transport the required heat flux from the incoming solar energy to the sodium vapor. This implies several conditions:

- a. The temperature drop across the screen wick on the dome (superheating) is low enough to avoid bubble formation, which could result in local overheating

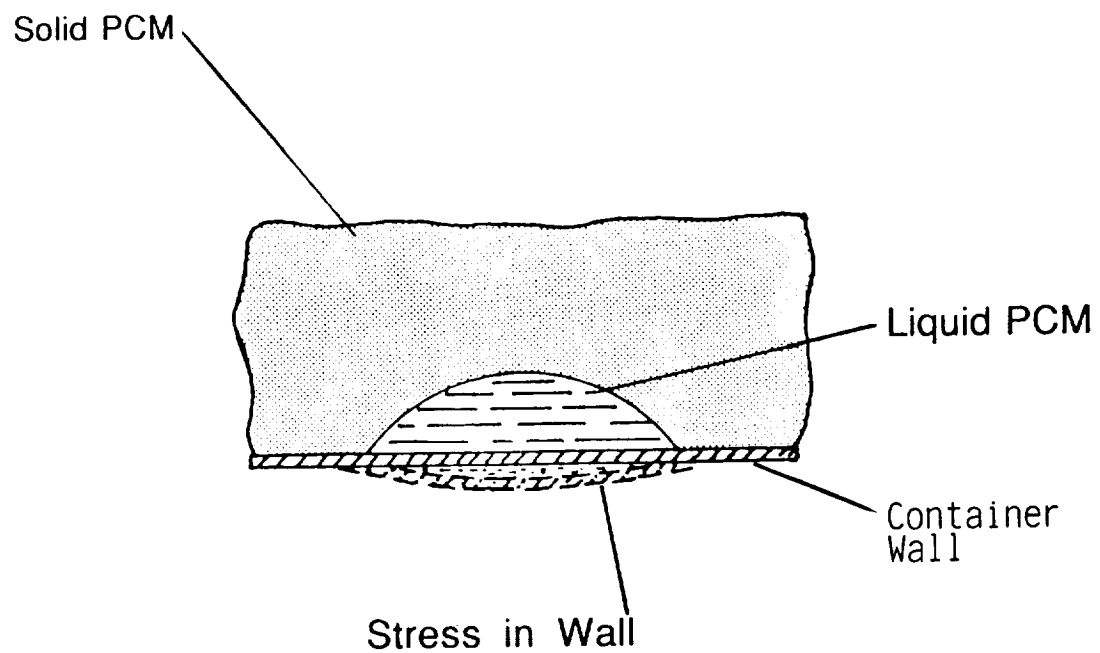


Figure 3.1 THERMAL RATCHETING

and melting of the dome.

b. There is adequate sodium flow through the wick. The pumping capability of the wick pore surface must be able to overcome pressure losses through the wick structure as well as gravity if the dome is to be tested in one-g.

c. Also desirable is the ability of the wick to 'self-prime' with sodium. This means that if the dome is placed in a pool of sodium, there is adequate pumping within the body of the wick (not at the surface) to draw the sodium up to the apex of the dome.

Meeting these conditions results in conflicting requirements. To reduce flow losses, it is desirable to increase the thickness of the wick (i.e. increase permeability) but this increases the temperature drop across the sodium and the consequent chances of bubble formation. Since the pumping capability of the screen surface is inversely proportional to the effective pore radius, a fine screen is desirable there, but if this same screen is used throughout the wick it will increase flow losses.

Estimating the allowable superheating in a wick is more difficult than it may at first appear. The classical theory is dependent upon balancing the vapor pressure in a bubble with the surface tension that tries to cause it to collapse. There is a critical temperature rise between the surface of the liquid and the dome surface that will result in sufficient local increase in vapor pressure for a bubble to grow, assuming a large enough nucleation site. This may be expressed as

$$\Delta T_{crit} = T_{sl} - T_{lv} = \frac{2\sigma - (P_v - P_l)}{r_n h_{fg} \rho_v}$$

where  $T_{sl}$  and  $T_{lv}$  refer to the solid (dome surface) -liquid and liquid-vapor interfaces respectively. The heat of vaporization,  $h_{fg}$  and vapor density,  $\rho_v$ , enter through the use of the Clausius-Clapeyron equation to estimate vapor pressure change with temperature. The greater the surface tension,  $\sigma$ , the larger the required superheat to allow bubble growth; whereas the superheat required goes down as the nucleation site radius  $r_n$  increases. Since the surface of the liquid is not a plane but forms a meniscus in the wick, a correction term appears as the difference between vapor pressure outside the wick ( $P_v$ ) and liquid pressure in it ( $P_l$ ).

The difficulty with this formulation is that the size of  $r_n$  is virtually impossible to determine *a priori*. Adkins notes that Chi's estimate of this radius for clean heat pipes ranges from  $2.54 \times 10^{-5}$  in the presence of noncondensable gasses to  $2.54 \times 10^{-7}$  without them (Ref.10,p.18). This represents a range, for our particular conditions, of about 50K to one hundred times that. As it happens, though, for the evaporator wick design selected the effect of  $(P_v - P_l)$  can be substantial, and at maximum reduces the value of the critical superheat (with the higher value of  $r_n$ ) to about 10K. (Further detail is given in a later section.) One of the design goals here was to achieve a temperature drop across the wick of that value or less. (Basic sodium property data used in this report is from Refs. 11 and 12)

Before the evaporator performance can be tested, it must first be fabricated. As will be discussed later, this in itself presented a formidable challenge.

## Chapter IV

### PCM Module Design & Testing To Avoid Thermal Ratcheting

#### 4.0 Introduction

At least two major problems must be dealt with before successful Phase Change Material (PCM) thermal storage modules can be built. The first is that of material compatibility of the module with the interior and exterior environment. The interior environment consists of the PCM and whatever contaminants are present. As a rule, molten fluorides are relatively benign in the absence of contaminants such as water and oxygen. For example,  $\text{MgF}_2$  can react with water to produce hydrofluoric acid. The work done by J. Daniel Whittenberger at NASA LeRC with Haynes 188 and the eutectic  $\text{CaF}_2 - \text{LiF}$  has shown insignificant effects on the alloy when the eutectic is outgassed under about  $10^{-7}$  torr vacuum.

#### 4.1 Void Positioning to Avoid Ratcheting

The previous chapter focused on the importance of positioning the void to prevent thermal ratcheting in the PCM modules. To do this essentially means that the following thesis statement must be satisfied:

The void space in the solidified phase change material must make contact with a heated wall such that the fluid may expand into the void as soon as (or shortly after) melting has begun.

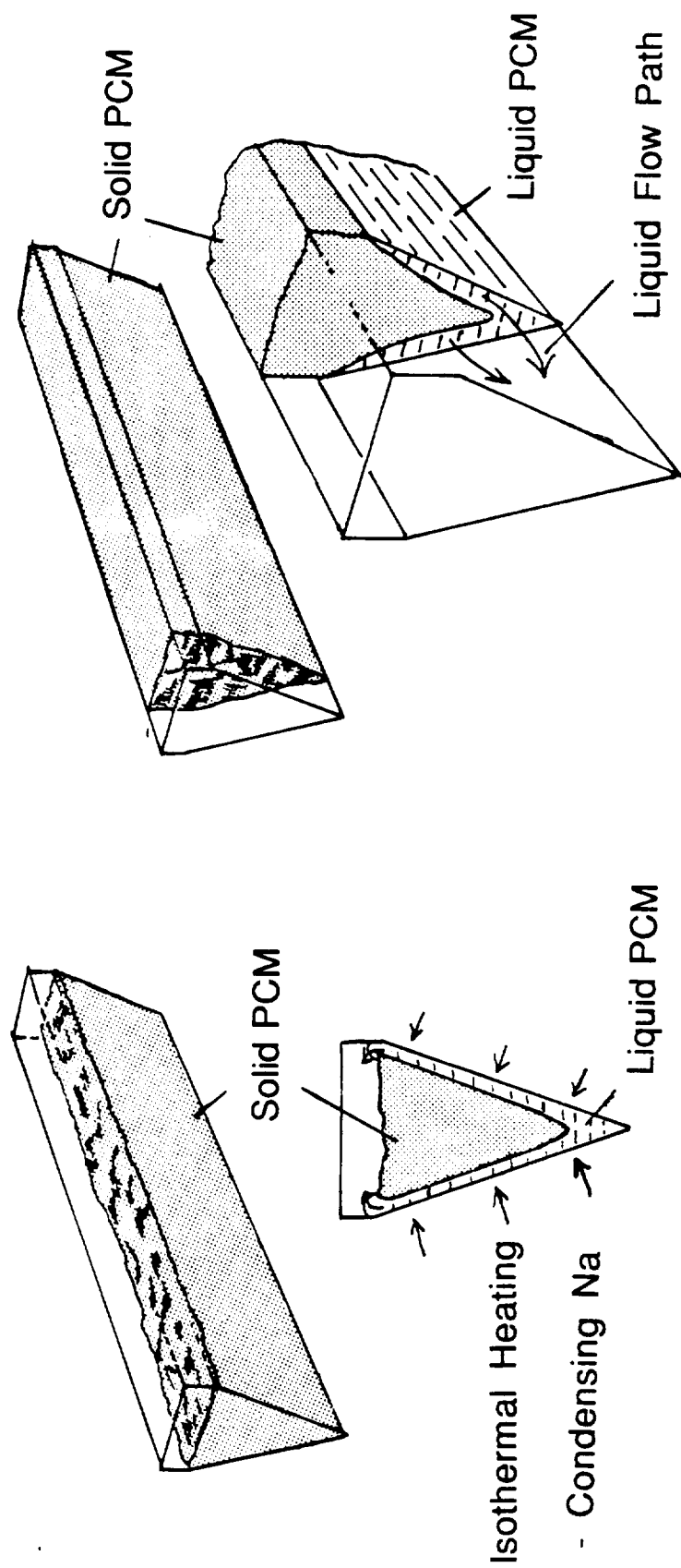
Figure 4.1 shows modules of the general configuration proposed for the cavity heat pipe receiver. The two cases are not intended to represent actual void locations under zero-g conditions, but they illustrate the potential for liquid flowing into a void space in order to avoid liquid pressure build-up. Note that the likelihood of satisfying the statement is improved due to the broad areas of near isothermal heating provided by Na condensation.

To predict void location in a PCM container through melting and freezing cycles is a formidable exercise. There are two reasons for this: first, the number and complexity of potentially significant transport phenomena under microgravity conditions; second, the dearth of reliable property data needed to model these phenomena along with the sensitivity of these properties to subtle chemical changes over time.

A full computer model incorporating the transport phenomena has been under development by D. Namkoong of NASA Lewis and J.B. Drake of Oak Ridge National Laboratories (ORNL) for certain restricted PCM module configurations (Ref.13). The characteristics of these phenomena can be summarized as follows:

##### Fluid Wetting

Liquid contact angle (related to surface tension,  $\sigma$ ) and module geometry (e.g. acuteness of angles between walls) will restrict void location in the absence of phase change.



Isothermal heating generated by condensing vapor (Na) uniformly creates a liquid flow path along the module wall accessible to the void.

Figure 4.1 Illustration of "Thesis Statement"

Further detail on the theoretical and practical application is provided in the section of the drop tower tests. Contact angle is very sensitive to small impurities in the melt, but for fluorides, values may be around  $60^\circ$ .

#### Aspiration

As a solid surface forms and propagates through a melt there will be a gradient of lowered pressure in the liquid at the boundary due to the shrinkage of the substance with phase change. This will draw more liquid towards the boundary.

#### Marangoni Effect

This is the bubble motion within a melt arising from a thermal gradient across the bubble. The consequence of this gradient will be a reduction in surface tension from the cold to the hot end of the bubble, since  $d\sigma/dT$  is negative. Surface tension expresses the discontinuity in tangential stress across the boundary; the fluid adjacent to the high tension end will tend to be moved in that direction, so that the bubble will move the opposite way (toward the hotter fluid) (Ref. 14). For the modules here the velocity could be up to several cm/sec. Since this effect depends on surface tension, it too is highly sensitive to melt impurities.

#### Vapor Transport

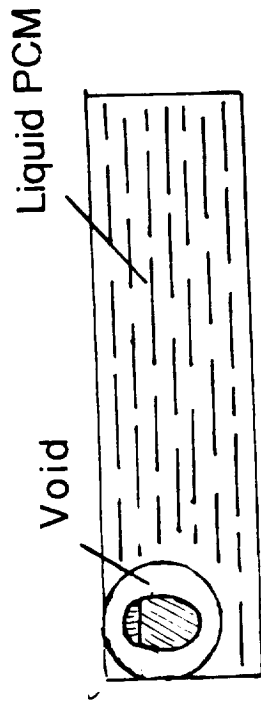
The upper limit for this will likely be in the order of a few  $\text{mg}/\text{cm}^2 \cdot \text{sec}$ .

Figures 4.2a,b show the results of a qualitative evaluation of melting - freezing behavior in the Sanders PCM modules considering the above factors. It is assumed in one case that the fluid wets the wall "well" (with low contact angle) and in the other that a surface coating results in poor wetting. In both cases we start from a "plug" of material frozen into one end of the module under 1-g conditions, leaving more than just the void volume associated with shrinkage.

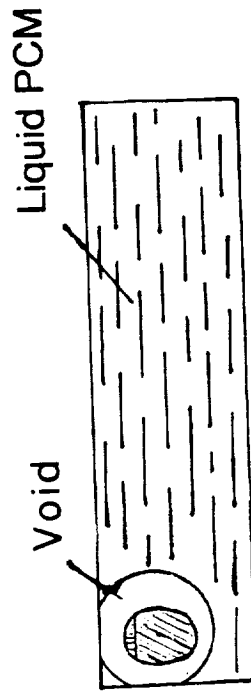
Note that for the non-wetting case it is postulated that the wetting angle is sufficiently large to prevent the fluid from filling in several of the corners, particularly the acute angle at the "bottom" of the "V" shape.

For the wetting case, the melted material allows the formation of a bubble which is nearly spherical but which contacts the "heated" walls in the areas indicated by the diagonal hatching. Compared with a small bubble, the motion of this one is relatively constricted. The PCM refreezes starting with the inner surface of the "V" from which heat is drawn out into the receiver cavity. Liquid moves toward the freezing surface; in the meantime the void space opens up more due to the phase change volume shrinkage. The Marangoni effect tends to move this void toward the hottest remaining fluid at the side opposite the apex of the "V". Remelting of the liquid is nearly uniform at the heated walls and allows the fluid to expand into the void space touching them.

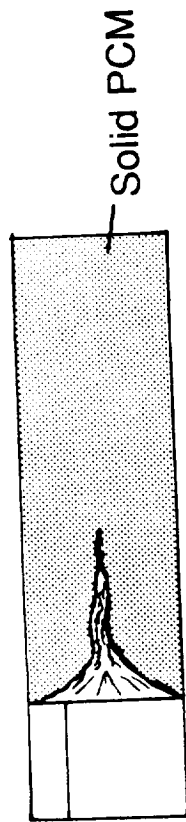
With non-wetting conditions the fluid may freeze into a shape similar to that shown in part 3 of Figure 4.2b. The fluid may now expand into a longitudinal channel during melting.



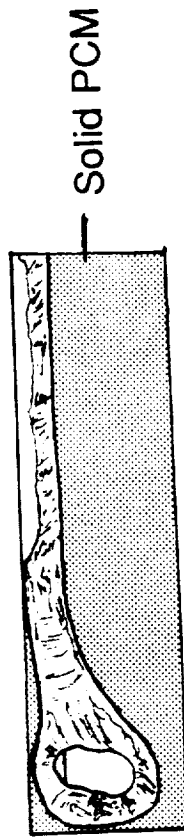
2. After Melting



4. After Remelting



1. Initial Solid Position



3. Refrozen

Repeat cycle in 3., 4. indefinitely

Figure 4.2a Scenario for Melting/Freezing Cycle in Zero- $q$  (wetting fluid)



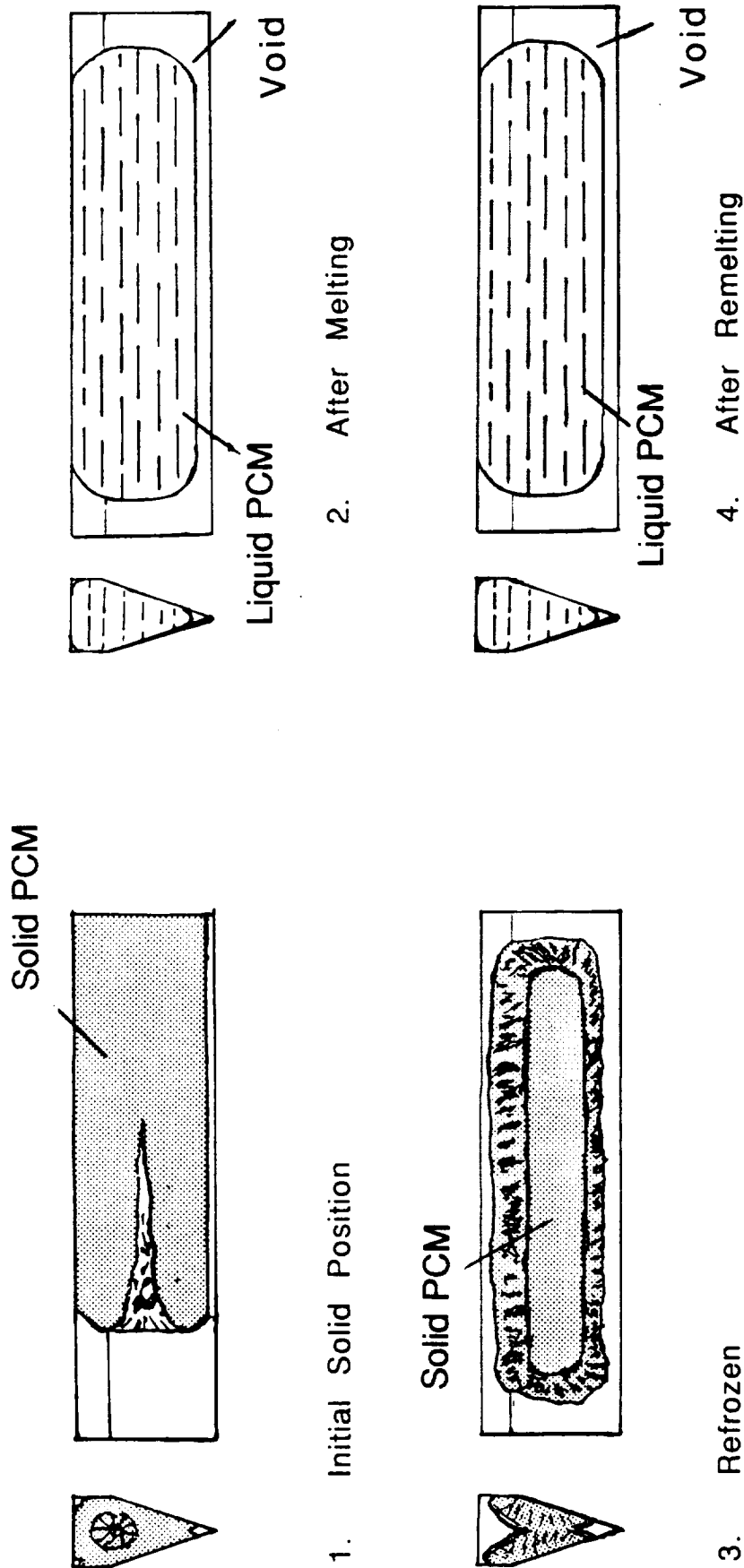


Figure 4.2b Scenario for Melting/Freezing Cycle in Zero-g (non-wetting fluid).

## 4.2 Drop Tower Tests of Bubble Positioning

### 4.2.0 General Remarks

After developing the void positioning criterion discussed above the objective was to apply theoretical and experimental methods to determine if it indeed could be satisfied. While it would have been most desirable to test full scale PCM modules under actual melting and freezing conditions in zero-g, this was impractical. In the same way, a decision was made against attempting freezing of the PCM during the twenty seconds of free fall provided by parabolic trajectory flight. The small size of the test modules needed as well as the complications and cost of preparing the required equipment were critical considerations.

The remaining option was use of the NASA Lewis 5 second drop tower. Attempting a test with phase change in that facility would have required very high freezing rates possibly resulting in unrepresentative crystal structures (although a German group is attempting this, Ref. 15). Instead, our tests examined the equilibrium positions of voids in room temperature liquids (mimicking the liquid PCM) of varying wetting angles on containers of two slightly different dimensions.

### 4.2.1 Theoretical Considerations

On the simplest level it may be stated that the void position in a liquid container in free fall will be determined by the minimization of total surface energy. Unfortunately, this statement (in common with its analogues in other areas of research) is of limited utility.

Changes in surface tension with time from slow chemical reactions, initial conditions or contamination and obstructions are among the factors that would be difficult to quantify theoretically. Moreover, without the disturbing forces provided by convection, metastable states can exist for indefinite periods. Nonetheless, the theoretical treatment is useful to point out general trends and thus the baseline suitability of a particular container.

For assistance in the prediction of void position the consulting services of Dr. Paul Concus (a professor at the University of California at Berkeley and Senior Scientist at the Lawrence Berkeley laboratory) were retained. This section results from his analysis; he also reviewed the interpretation of the test results.

A wedge geometry was initially assumed for the container. This is quite similar to long zero-g channels that have been considered in the past and the basic theory is well understood.

The approach was to treat each of the corners at the bottom wedge, top and sides as if it were part of an infinite wedge with a different angle in each case. The criterion for liquid extending indefinitely along the wedge by capillary action is  $\alpha + \gamma < 90^\circ$ , where  $\alpha$  is contact angle and  $\gamma$  is one-half the wedge angle. One consequence of the wetting theory is that the test of void position should give information for two different wetting angles. The obvious result is for the actual liquid and void fraction; the less obvious one is for a fictitious liquid of supplementary contact angle and liquid

fraction equalling the actual void fraction. In other words, in the second case liquid and void switch places. This fortuitously allows the testing of non-wetting fluids using wetting ones. Of course practical complications may make this difficult.

For the drop tower work, the test vessel geometry was as shown in Figure 4.3 a, b, c with the two wedge angles but identical lengths. A third geometry was ultimately chosen for the PCM phase change tests for reasons of volumetric efficiency. Time, budget and technical complications prevented drop tower tests of this last design which was based on that in a paper by Concus and Finn (Ref. 16).

Some effort was made to characterize wetting angles for various proportions of distilled water and ethanol using a sessile drop; however given the limits on available time and resources it proved impossible to overcome the problem of a changing contact angle with time. In the end, two fluids were used for the drop tower testing, one designated as having a low wetting angle (about  $15^\circ - 30^\circ$ , composed of 50% ethanol by volume) the other as having a high one (approximately  $80^\circ - 90^\circ$  and containing only distilled water).

Given the outline above, some general predictions were made regarding the placement of voids in the test vessels. For example, applying the wedge wetting criterion to all corners in either of the vessels tested the void location predicted is as shown in Figure 4.4. This assumes the use of the good wetting fluid and a fairly full container (note that for clarity the void bubble has been shown as opaque and its contact area with the wall is cross-hatched). With the less wetting fluid the wedge wetting rule suggests that the "V" would not have to be wetted for its entire length and might not wet at all given the correct initial conditions.

This theoretical background will be referred to in the discussion of the test results later on.

#### 4.2.2 Test Equipment

The drop tower vessels were manufactured from 3/16" thick Type II UVA plexiglas except for the end plates, which were 1/4" thick and provided slots into which the side walls fit. A filler type adhesive was used and a fill port drilled into one end of each vessel. Masking tape was used except at the joining of the last piece (the long piece opposite the V wedge) to avoid squeezing out excess glue into the corners.

Up to four containers can be mounted horizontally in the aluminum frame; two others can be mounted vertically (Figure 4.5). All of the containers can be rotated along their long axis (by  $90^\circ$ ) so that either their side wall or top cover plate is visible to the camera in the drop tower vehicle. (To show the horizontal vessels with the V wedge opening 'downward' by definition in 1-g would require rotating the entire frame). By changing the orientations, the initial (1-g) void location can be tested for its effect on the free fall equilibrium.

Before assembly, the plexiglass surfaces were cleaned by the procedure recommended by Mr. Ray Sotos, director of NASA Lewis 145 meter drop tower (zero - g facility). This consisted of:

- a) wash with Alconox detergent
- b) multiple distilled water rinse

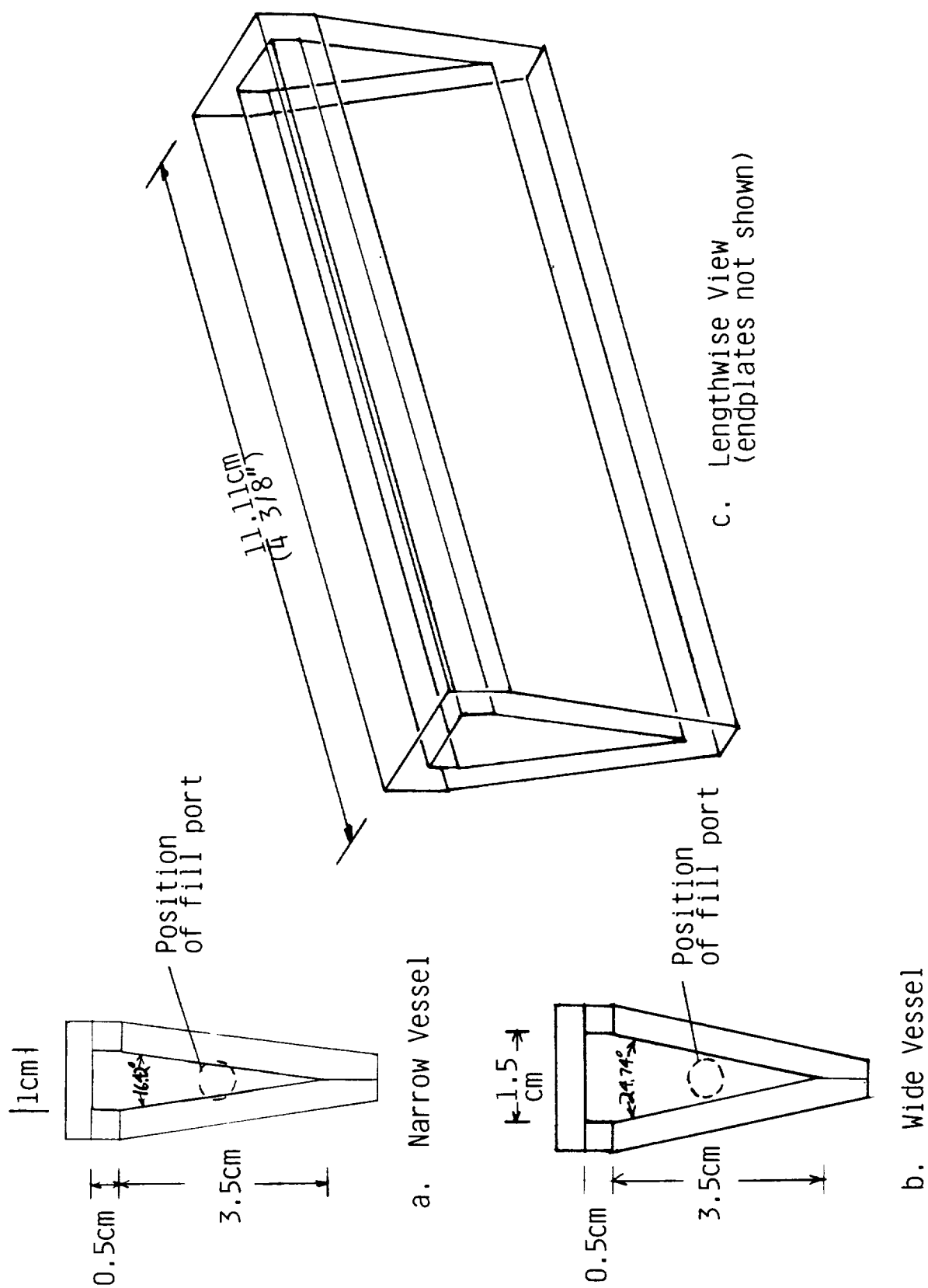


Figure 4.3 Drop Tower Test Vessels

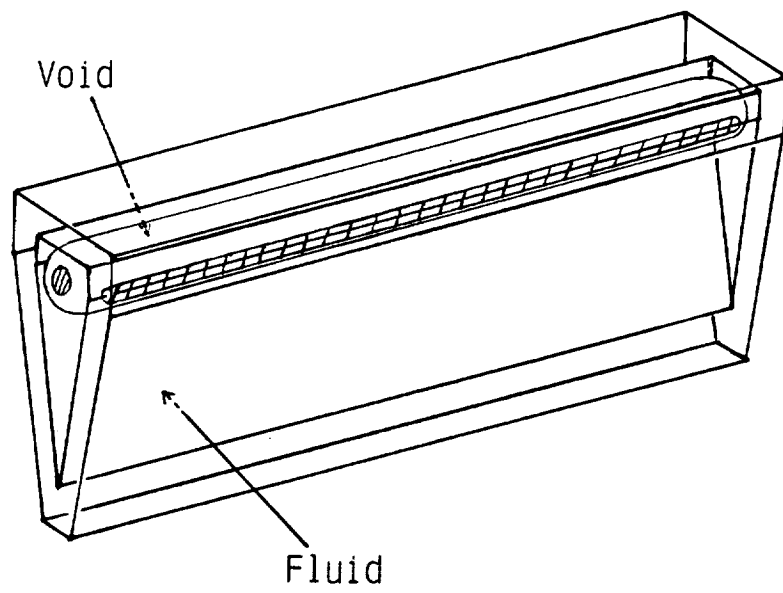


Figure 4.4 Expected Void Position in Container



- c) rinse with diluted ethanol
- d) multiple rinse with distilled water

This procedure was repeated before the closing piece (top plate) of the vessel was glued in place. Afterwards, the vessels were oven annealed for several hours to relieve internal stresses from the cutting and assembly processes.

Mr. Sotos provided valuable advice and suggestions on the design and construction of the test vessels. Since the drop tower is evacuated, it is necessary that vessels withstand 1.5 atm internal over-pressure. To set the (worst case) wall thickness, the largest area side wall was approximated as a fixed edge plate and the Timoshenko maximum stress formula applied,

$$\sigma_{\max} = \frac{\beta q b^2}{t^2}$$

Here  $q$  is the internal pressure,  $b$  is the width,  $t$  is the thickness while  $\beta$  is set by length / width ratio and Young's modulus  $\nu$ . (The last of these is not readily available for the plexiglass, but  $\sigma_{\max}$  should be accurate within ~ 15% for  $.30 \leq \nu \leq .35$ ).

#### 4.2.3 Test Procedures

The completed test assembly (except for the fluids, which were shipped separately) was transported by hand to the Lewis facility. Testing was carried on according to established procedures by Mr. Sotos and his staff. Data was gathered by high speed (approximately 400 frames per second) 16 mm movie camera. A back lighting box provided illumination and a digital clock showed time since vehicle release in hundredths of a second. Cleaning and annealing was performed between each drop, the latter to relieve drop-induced stresses or surface crazing from ethanol evaporation.

A blue tint was added to the fluids at the test facility to improve visibility. Previous work there had shown this tint to have no perceptible effect on the fluid wetting characteristics.

#### 4.2.4 Test Results

A total of four drops were made during the test sequence. The second was a repeat of the first but with correction of overexposure and addition of more blue tint. As best as could be discerned the results of the first two drops were virtually identical in terms of void numbers, position and size.

The equilibria reached in drops 2, 3 and 4 are sketched in Figures 4.6 through 4.8. (These are side views rather than cross-sections through the container.) Little or no fluid motion was apparent after the first second or so of free fall. A 'wide' or 'narrow' angle wedge is designated 'W' or 'N' respectively and the liquid and its fill fraction is shown in each case. These data are also summarized in Table 4.1. In a number of cases - particularly for some bubbles, where the radius of curvature was relatively small - the liquid-vapor interface appeared as a prominent darker region. This is indicated in the figures by 'half-hatched' lines on the liquid side of this boundary. In

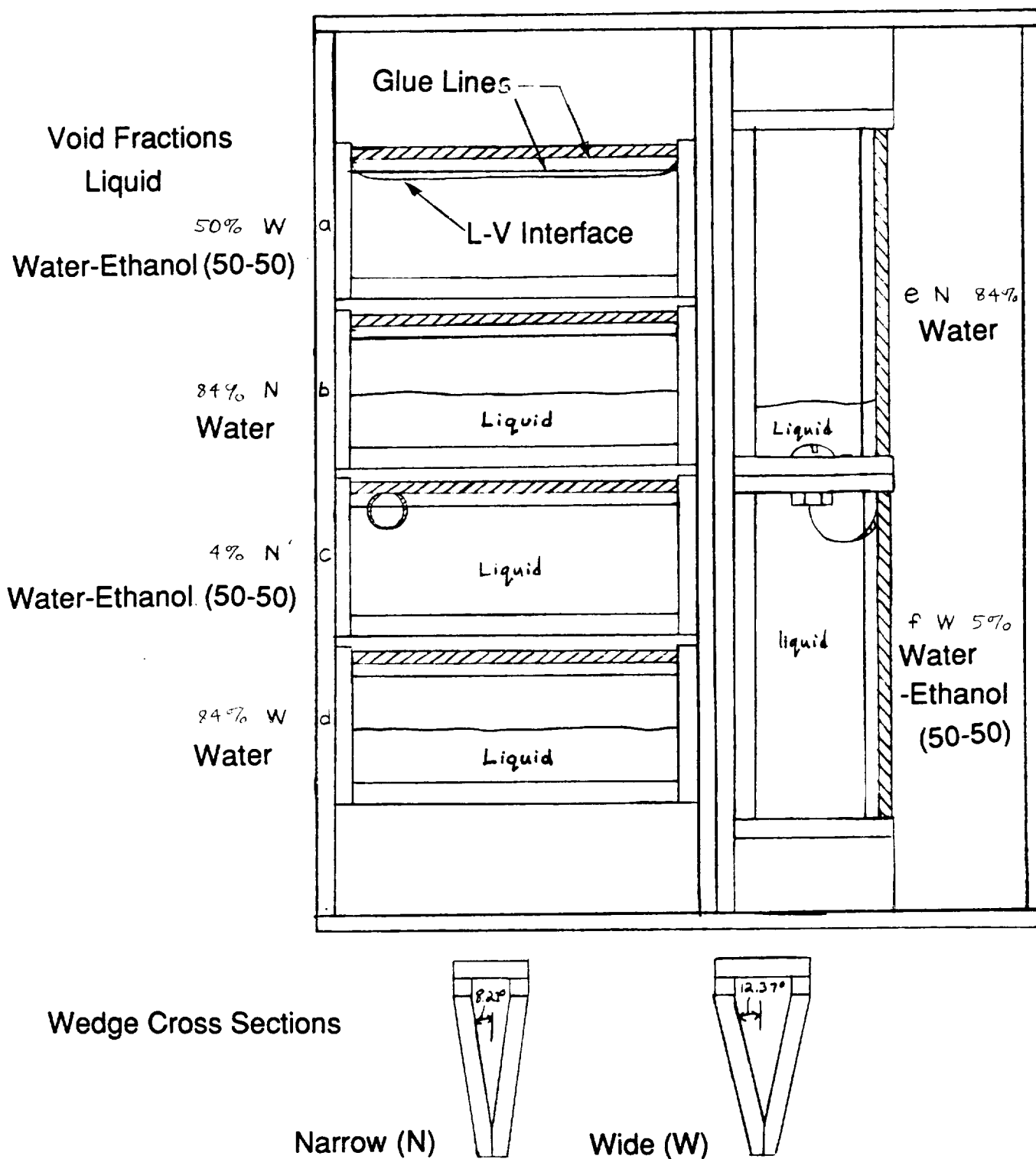


Figure 4.6 Bubble Positions During Second Drop



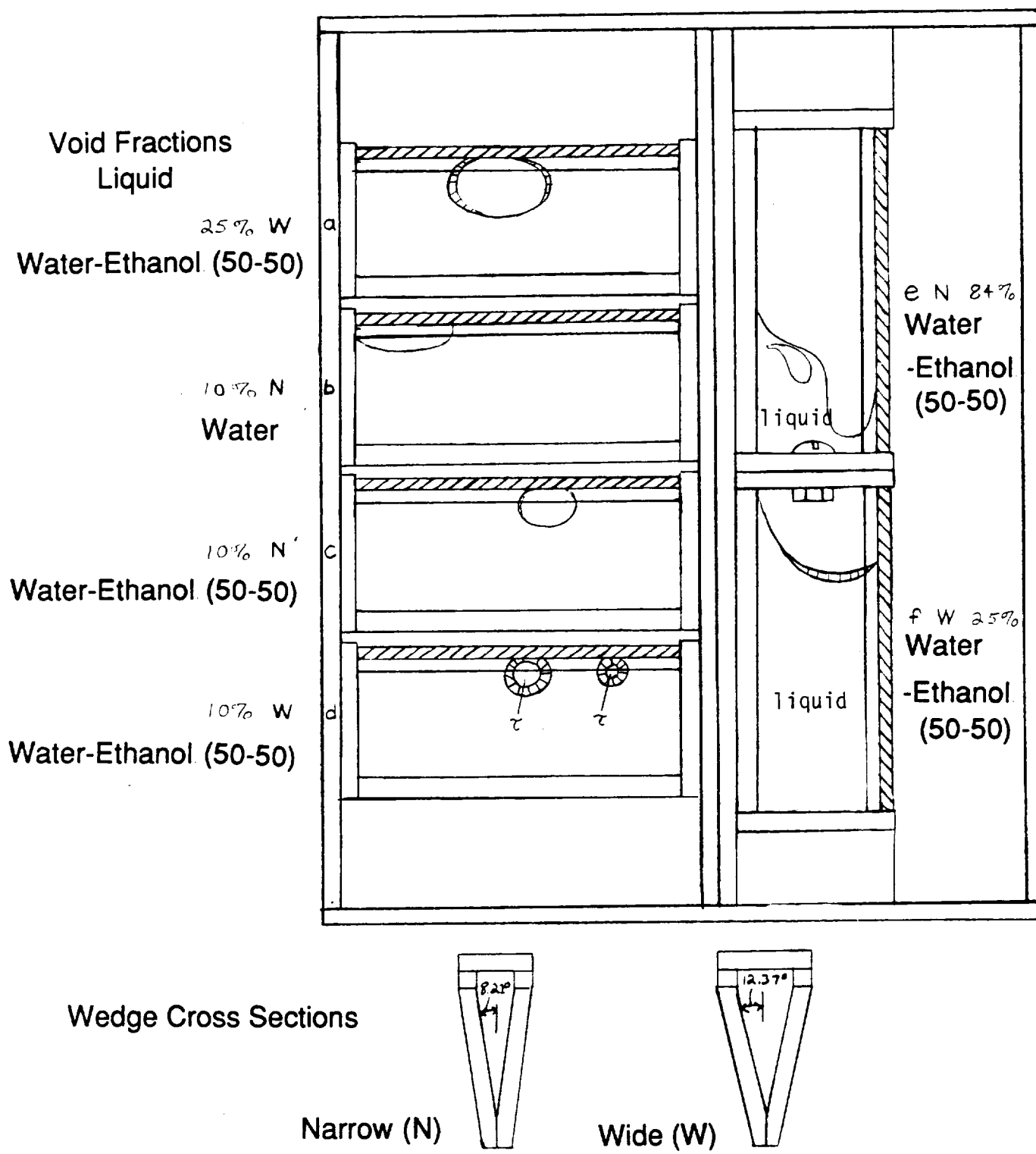


Figure 4.7 Bubble Positions During Third Drop

(Fill fractions and liquids used correspond exactly to Third Drop)

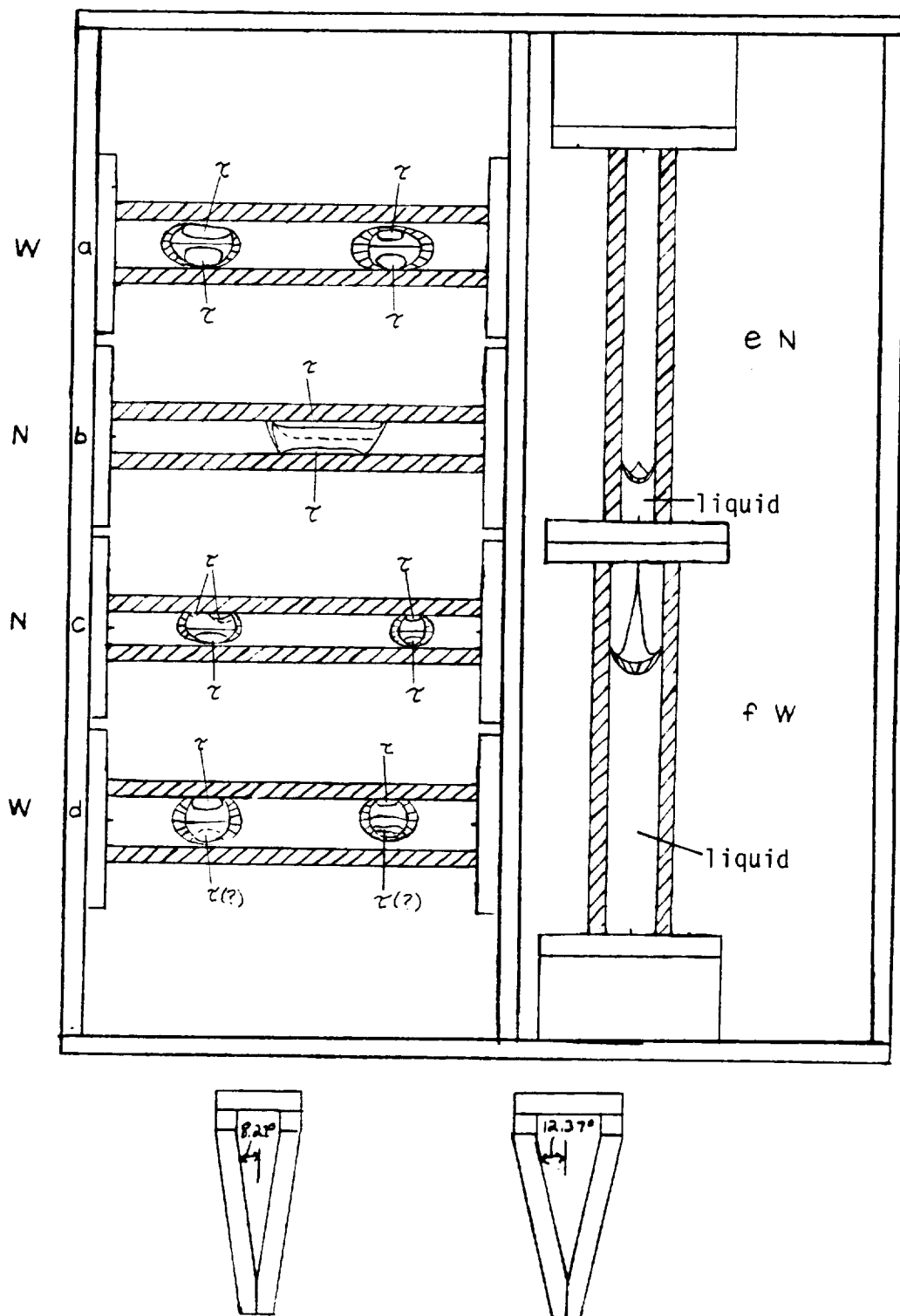


Figure 4.8 Bubble Positions During Fourth Drop with Containers Rotated 90°

Table 4.1 Conditions in Drop Tower Tests

Frame Position Test	a	b	c	d	e	f
Second Drop	Wide Mixture 50%	Narrow Water 84%	Narrow Mixture 4%	Wide Water 84%	Narrow Water 84%	Narrow Mixture 5%
Third Drop	Wide Mixture 25%	Narrow Water 10%	Narrow Mixture 10%	Wide Mixture 10%	Narrow Mixture 84%	Wide Mixture 25%
Fourth Drop	Wide Mixture 25%	Narrow Water 10%	Narrow Mixture 10%	Wide Mixture 10%	Narrow Mixture 84%	Wide Mixture 25%

Modules  
Rotated  
90  
degrees

"Mixture" is 50% distilled water, 50% ethanol.  
Both fluids use blue tint.

areas where the contact region of the bubble with the wall is not immediately clear from the contours this region is designated with a  $\tau$ .

In containers b and d of Figure 4.6 (second drop), both using the high contact angle distilled water, the initial position of fluid (due to gravity) was in the wedge. The fluid did not climb up the end corners in zero-g, which is in accord with the theory, since  $1/2(90^\circ) + \gamma > 90^\circ$  where  $\gamma$  is  $> 45^\circ$ . There was an irregular contact line along the walls, probably attributable to the microscopic roughness effect discussed by Myshkis (Ref. 17) or to dust contamination. (This effect appears to be far less pronounced for the better wetting fluid, which seems to be qualitatively sensible). Container e again used distilled water. That the fluid did not climb up the narrow wedge angle would imply that  $8.21^\circ + \gamma > 90^\circ$  or  $\gamma > 81.79^\circ$ .

In container a, with the wetting fluid, we had expected from the theory that it would run along the top edges, possibly forming the "hot dog" shaped void illustrated earlier. The fluid may have been prevented from running along these edges by excess glue from the assembly process. (As noted before, the piece opposite the wedge was the last glued on, and excess glue could therefore not be prevented by masking.)

Vessels c and f each show a single void bubble, and each appears to meet our design criterion of contact with the slanted walls of the wedge (corresponding to the heated walls of the PCM container). In the first drop (the one not shown here), the bubble in c was in contact with the end of the container as well as the top. The minimum void fractions for spheres just touching the side walls are  $\sim 2.1\%$  and  $\sim 4.7\%$  for the narrow and wide vessels respectively. (The total volumes are 25.00 and 37.51 cm<sup>3</sup>). The minimum void volume for the 'hot dog' shape just touching the walls is 50% in the wide container.

Note that there is a clear tendency for the voids to retain contact with the walls that they were touching under 1-g conditions.

In drop 3 (Figure 4.7) further variations are seen. The void fractions were modified to search for boundaries of different types of behavior and only one vessel using the pure distilled water was retained.

Halving the void in container 'a' resulted in an ovoid gas volume. It does not appear that the fluid extends the entire length of the top edges. In c the increased void compared to the last time slightly elongates the bubble, but when water is used (in b), it is very far from spherical, which is consistent with the theoretical result that the less wetting fluid is not inclined to spread along the top edges.

For vessel d the bubble has broken into two parts, each of which appears to satisfy the wall contact criterion.

In the wide vessel f, the water / ethanol wets up the sharp angle but less so at the outer edges. If the theory is applied assuming nonwetting at these edges (i.e. no hysteresis or excess glue causing an obstruction to wetting) this would require;

$$\begin{array}{l} 45^\circ + \gamma > 90^\circ \\ \gamma > 45^\circ \end{array} \quad \} \text{ From the } 90^\circ \text{ edges}$$

which still satisfies the condition for wetting the wedge that

$$12.37^\circ + 45^\circ < 90^\circ$$

unless  $\gamma$  were very large indeed. It would be surprising if the value of  $\gamma$  for the wetting fluid were  $45^\circ$  or larger, so there may indeed be more at work here than the theory alone.

The results in vessel e were distorted by signs of an apparent leak i.e. bubbles forming from the base of the "V" joint, but the final drop was performed before this was noticed.

The final drop (Figure 4.8) was conducted with the same conditions as in the third, except that the vessels were rotated by  $90^\circ$ . Overall the results were similar, except for two changes. First, pairs of bubbles formed in containers a and c in addition to d. Second, the "leak" deduced to have been present in vessel e showed no obvious evidence of being present.

The appearance of multiple bubbles in the containers is of some concern since it is imaginable that a large number might form that are not in contact with the wall. However Concus suggests - and examination of the films seems to confirm - that the formation of two bubbles simply represents one of the major dynamic modes in the transition from one-g to zero-g conditions. One observes the fluid at the bottom of the initial one-g bubble "pinching up" somewhere in the middle while to either side a bubble forms that retains contact with the wall.

The behavior of the fluid in container e contradicted the theory, which would predict that a fluid wetting the wedge in "f" would surely wet the narrower one in e, although this behavior may have been related to the presence of a leak.

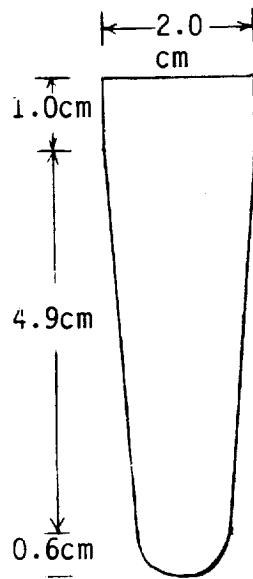
Despite the practical uncertainties, it appears that the fluid positioning theory of Concus provides a workable rationale for designing containers and designating void fractions that will meet the criterion for void position to avoid thermal ratcheting, without resorting to the difficult task of providing a nonwetting container. Nonetheless, it would be essential to perform tests in zero-g with an actual PCM to confirm this with the added factor of phase-change cycling.

### 4.3 Phase Change Material (PCM) Ratcheting Test

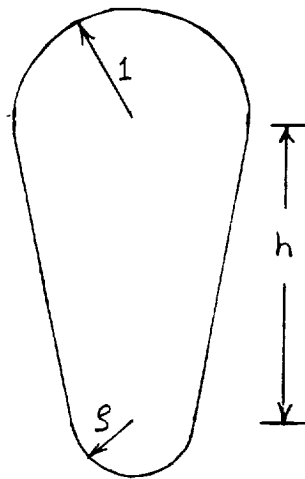
#### 4.3.1 Module Design For PCM Test

The drop tower results suggested a good possibility of meeting the criterion to avoid ratcheting in long narrow vessels with a pointed wedge. However, several considerations resulted in a modification of the vessel cross section. It is believed that the modification will not materially affect our ability to meet our criterion; indeed, it may improve it.

This new shape is shown in Figure 4.9 along with a similar shape for which a wetting theory had been developed in the paper by Concus and Finn (Ref. 16). According to Concus, the wetting behavior in our selected shape should be substantially the same.



a. Selected Geometry of PCM Module Cross-Section



b. Generalized Geometry from Concus and Finn (Ref. 16)

Figure 4.9 Variations in PCM Module Geometries

Given the indicated angle  $\alpha$  as well as the value of  $\rho$  (ratio of the smaller to the larger cross-section radius), Figure 2 of the paper shows critical maximum liquid contact angles for wetting along the length of the vessel in the narrower part. Treating the "radius" of the squared off end of our vessel as 1 cm,  $\rho = 0.6$ , and the critical contact angle is about  $180^\circ$ . This compares with about  $92^\circ$  as a maximum contact angle for wetting the narrow V- wedge tested in the drop tower. Recalling the earlier discussion of ratcheting, a fluid which does not wet the entire length of the vessel will be more likely to provide an escape path for liquid during melting. Thus it appears that for a reasonable range of contact angles, the vessel with the rounded tip will be more advantageous. However, this advantage may be reduced because of wetting along the remaining  $90^\circ$  corners. While it would have been possible to design a container with precisely the cross-section found in the Concus and Finn paper, this would introduce mechanical complications in providing a flow channel for sodium beyond the outer radius of the modules in the solar receiver chamber.

Aside from the possible benefit in wetting behavior, there are two primary advantages to the chosen cross section. First, with the rounded tip, stresses in the container wall (arising from the sodium pressure in the receiver chamber) are reduced. Creep requirements can then be met using a thinner wall. Second, the new shape provides a lower surface area/volume ratio, which should lead to a lower mass receiver.

The actual dimensions of the module (cross section and length) were based upon a rough estimate for meeting certain geometric requirements of the receiver with a given quantity of fluoride. These include: a "clear diameter" at the center of the receiver of  $\sim 30$  cm; a packing of adjacent modules large enough for sodium condensation but small enough to maximize volume occupied by PCM; and an overall length/diameter ratio close to one for the receiver, again to minimize surface area to volume. A total of about 64 modules are required, each 47.5 cm in length and accommodating a 10% void space for the molten fluoride.

#### 4.3.2 Fabrication of PCM Modules

For the test, two modules were fabricated from the Haynes 188 0.050" alloy furnished by NASA Lewis. A finished module is depicted in Figure 4.10. A "collar" was added to allow the module to be welded into the test chamber such that the same surfaces will receive and lose heat from the sodium as in the cavity receiver design. Also, a fill tube of type 304 stainless steel was added. It would have been preferred to use a tube of the Haynes alloy, but it proved impractical to obtain. Whittenberger at Lewis advised that the steel / Haynes combination was likely to be acceptable for the duration of the testing; the Haynes manufacturer had no data on such combined welds. The sequence of fabrication is depicted in Figure 4.11. After cutting approximately sized pieces, the top cover and trough were bent using steel forms. They were then welded together using metal backing forms to avoid excessive distortion. A cut-out on the internal aluminum form prevented excess heating of it. Steve Ernst of the Haynes company suggested that it would be desirable to minimize "burn through" in the weld that produces exotic oxides. Prior to the final weld, several test welds were made; also, argon gas was blown onto both sides of the seam during welding. Despite the backing a slight bowing occurred. After this the single welded long piece as well as all other parts were cleaned in acetone and distilled water and air dried. This cleaning method had been suggested by Bruce Gillies of ETEC.

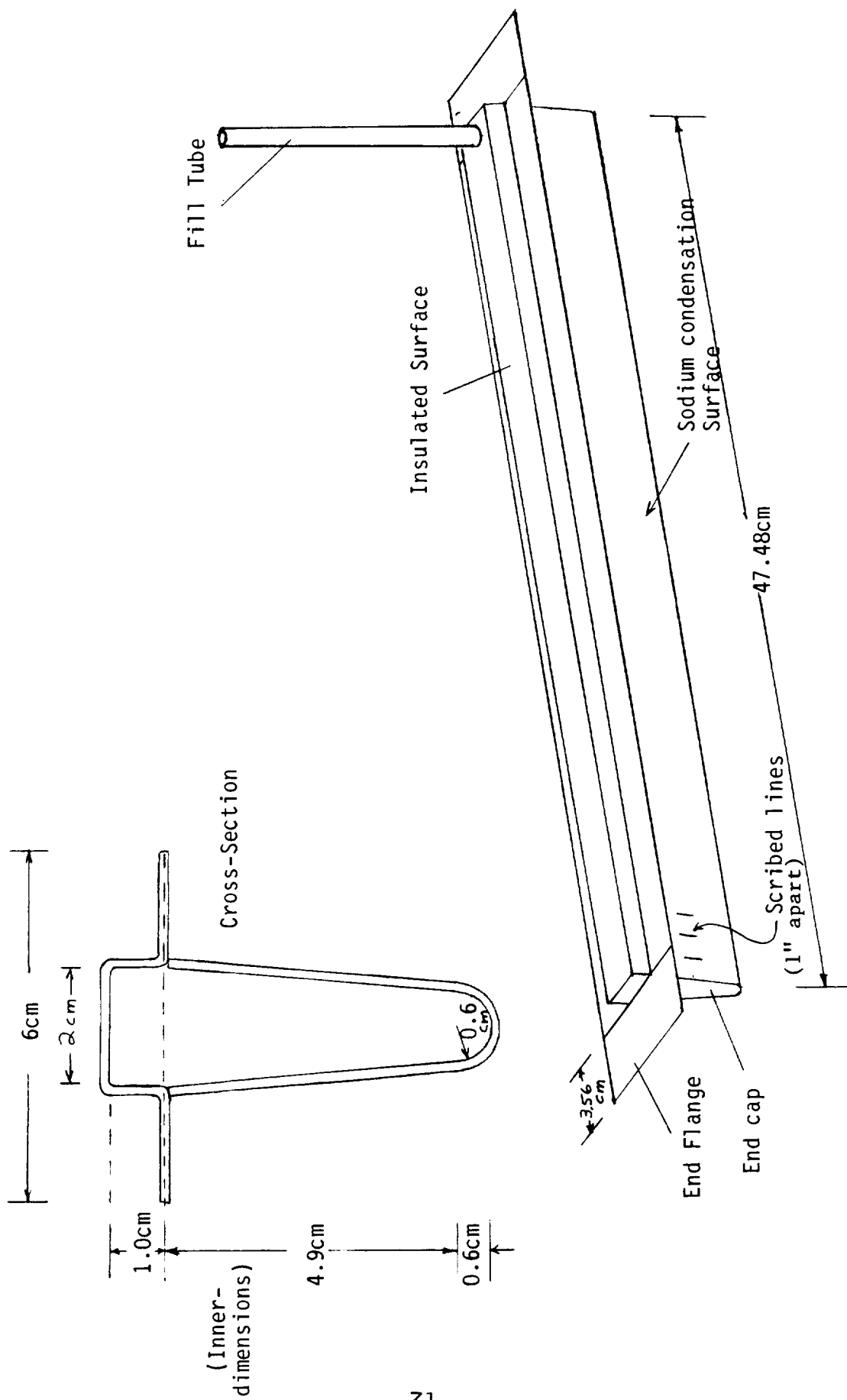


Figure 4.10 PCM Module Design



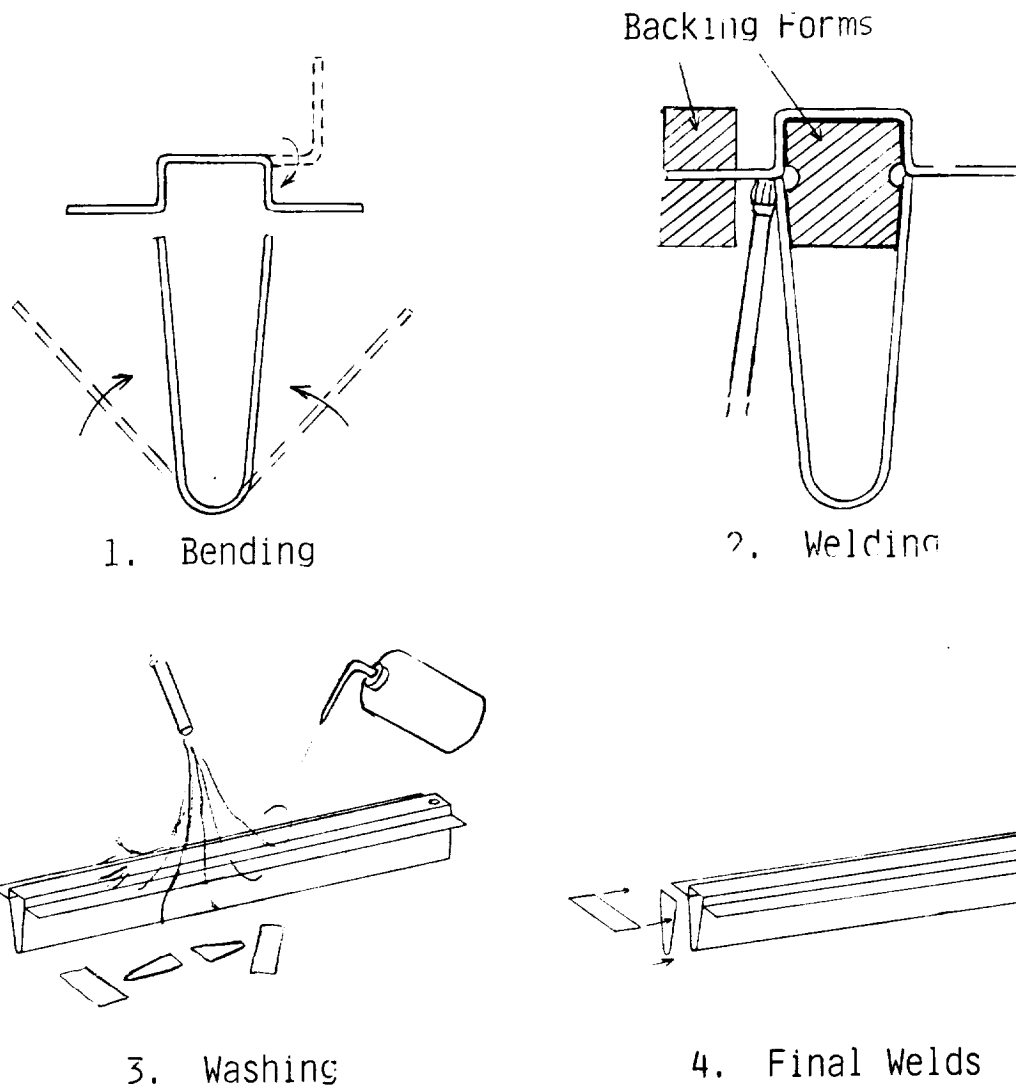


Figure 4.11 PCM Module Assembly Sequence

The end caps and collar ends were then welded on. Annealing in an argon atmosphere was performed following the instructions of Dr. George Lai of Haynes, who recommended annealing following any cold work of the metal. The module was heated to 1450° K (2150° F) and maintained for 1 - 2 minutes, then rapidly quenched in a blast of argon. Afterwards it was extremely clean, and no further washing was performed.

Finally, the fill tube was welded into place and a helium leak check performed on each module.

### 4.3.3 Test Equipment

In order to simulate the type of heating that the PCM module would encounter in the actual solar receiver (near isothermal heating by condensing sodium vapor) the modules were installed in the cylindrical (stainless steel) chamber shown in Figure 4.12. Liquid sodium is vaporized from a reservoir at one end, condenses on the modules, then drips down onto a screen and flows back to the reservoir. Dynatherm Corporation of Cockeysville Maryland, constructed the cylinder, purchased the ceramic heater unit, cleaned the chamber and filled the reservoir with sodium before sealing. (They recommended the use of the screen wick along the bottom half of the cylinder though it only provides about 6" of vertical pumping capacity. The cylinder does not have to act precisely as a heat pipe in order to be effective). Each half of the ceramic heater (maximum operating temperature of 1210°C) is rated at 1290W maximum for single phase, 230VAC.

The heating chamber was mounted at a 45° angle (the fill pipes at the high end) for testing. It is not possible to reproduce the free-fall liquid fluoride position in one-g, but this mounting does provide a test of a worst case condition for meeting the criterion to avoid ratcheting. ("The melting liquid must have access to an open void space") If one can be reasonably confident (by the results of the drop tower tests) of being able to place a bubble in the wide part of the wedge to meet the criterion, then the worst condition would be a bubble at one end of the module, so that the liquid has the longest path to transverse. The experiment then effectively becomes a test of the isothermal heating quality of the vapor chamber; if this quality is not adequate, the melting eutectic would be blocked on its way to the void space and ratcheting could occur.

The plan was to fill only one of the two modules in the heating chamber with fluoride eutectic in order to provide a 'control' module for wall distortion. Both modules are marked with ticks at one inch intervals along the center lines of their slanted faces.

Thermocouples can be mounted in the indicated thermowells penetrating the chamber. Others were to be fixed to the top surface of the modules to detect the melting and freezing cycles of the PCM.

In order to make the PCM melt and freeze a method must be provided to heat and cool the test chamber. It was assumed that the melting and cooling periods are close to those for an actual low orbit space power system (about 59 minutes to melt and 35 minutes to freeze). Due to its relatively low packing density (1.733 gm/cm<sup>3</sup>) the eutectic powder will fill only about 83% of the module volume after melting (liquid

Positions of Thermowells from  
end of Tube at "0":  
A: 1.072m (42.21")  
B: 0.837m (32.96")  
C: 0.255m (10.04")  
D: 0.255m (10.04")  
E: 0.546m (21.5")  
(other side)

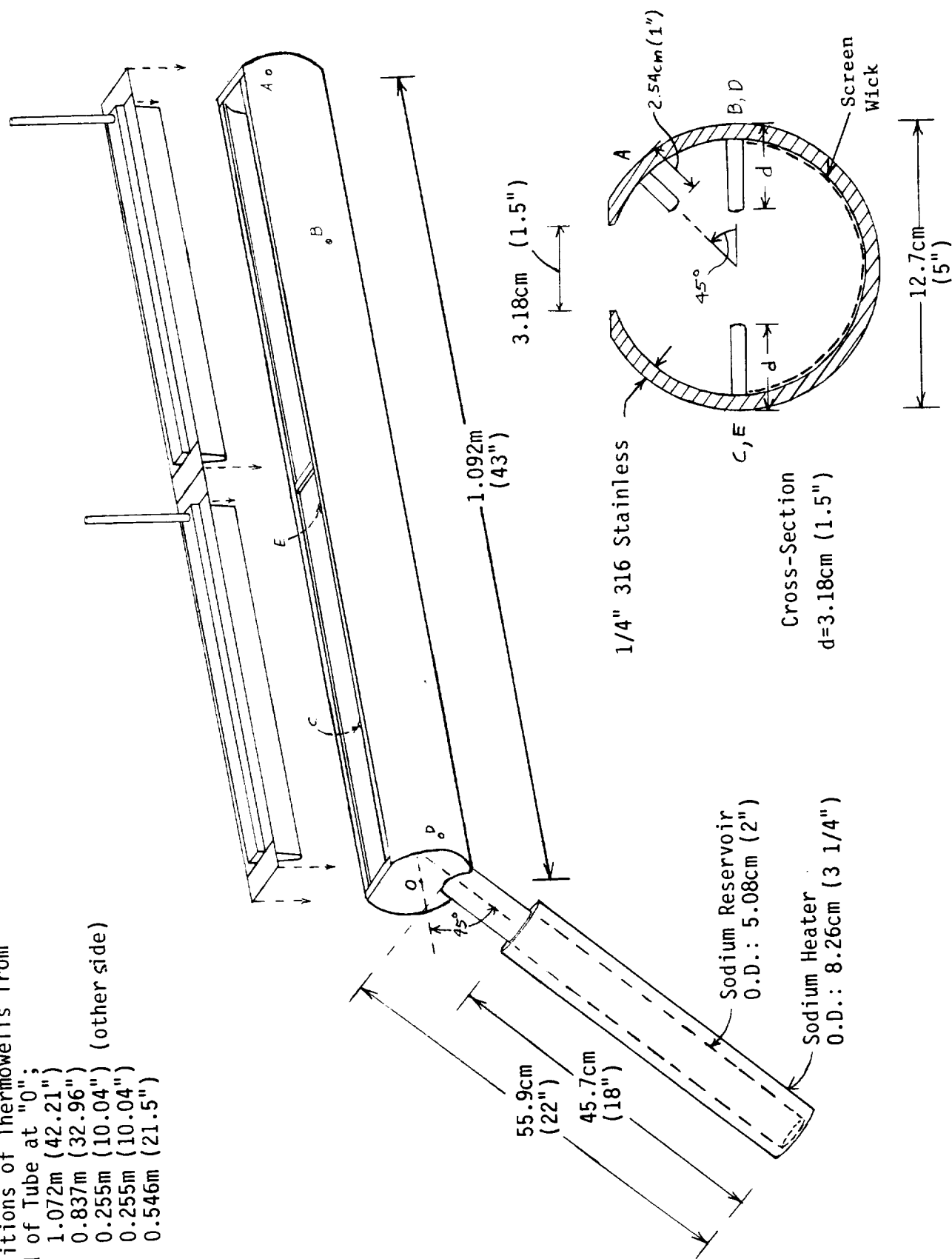


Figure 4.12 PCM Module Test Chamber

density about  $2.087 \text{ gm/cm}^3$ ). If no more powder is added after the initial melting, the storage capability of the module will be  $6.45 \times 10^5 \text{ J}$ . Therefore 182 Watts are required for melting and 307 Watts are released during freezing.

If there were a continuous screen wick covering the modules and having sufficient pumping capability from the sodium reservoir the module could be cooled by evaporating sodium and condensing it on the cylinder walls. But this was judged to present a difficult problem when installing the modules into the cylinder. Instead, radiative cooling to the cylinder was assumed. That means that the cylinder and the sodium reservoir must be cooled sufficiently to allow the module to release the required heat in the time available.

The required cooling may be estimated as follows: Approximate the module inside the cylinder as a concentric cylinder. From Siegal and Howell (Ref. 18), the radiative transfer rate  $q$  per unit area for such a condition is given by

$$q = \frac{Q}{A_1} = \frac{\sigma(T_1^4 - T_2^4)}{\frac{1}{\epsilon_1} + \left(\frac{A_1}{A_2}\right)\left(\frac{1}{\epsilon_2} - 1\right)}$$

for the module surface (area  $A_1$ ) a specular or diffuse reflector, and for the inner surface of the chamber cylinder (area  $A_2$ ) a diffuse reflector. The respective emissivities are the epsilons labeled '1' and '2'. If one is solving for  $T_2$ , the temperature of the cylinder, one notes that the smaller the ratio  $A_1/A_2$ , the closer  $T_2$  can be to  $T_1$  for the transfer of heat at a given rate. Clearly one wants  $T_2$  close to  $T_1$  to expend the minimum effort in cooling the large cylinder rather than the PCM module itself, and thus we want  $A_1/A_2$  small; it is actually about 0.12. However, if the surface of the chamber cylinder is specular, the formula drops the factor of  $A_1/A_2$  and the value of  $T_2$  needed is lower than before. To reduce the specularity of the cylinder, the vendor sanded the inner surface.

The emissivities are also important. It was assumed that in the environment of highly pure sodium surface oxidation will be minimal and they were both set at 0.2 (probably on the high side for the Inconel, but about right for the stainless steel).

The result is  $T_2 = 893 \text{ K}$  for a diffuse cylinder and  $736 \text{ K}$  for a specular one. Given a cylinder mass of about 20.5 kg and specific heat of  $627 \text{ J/kg} \cdot ^\circ\text{K}$  one must remove  $1.89 \times 10^6 \text{ J}$  in the first case and  $3.91 \times 10^6 \text{ J}$  in the second. (Keep in mind that all this heat must be removed before the PCM may cool at the required rate). The liquid sodium reservoir must be cooled at the same rate as the cylinder, since the vapor from the former will keep the latter hot. The cooling requirement for sodium with the larger temperature drop is about  $2.69 \times 10^6 \text{ J}$ , giving a total of  $3.94 \times 10^6 \text{ J}$  when the cylinder is added. Adding the module cooling gives  $4.58 \times 10^6 \text{ J}$ , or a loss rate of about 2180 W over 35 minutes. To reverse the process over 59 minutes requires 1293 W, which must be provided by ceramic heaters with a combined maximum rating of 2580 W. Sufficient insulation must be available to allow effective heating, as the radiative loss from the bare cylinder at 10400 K would be about 20

kW (assuming a well oxidized surface, with  $\epsilon$  approximately equal to .7).

To meet both the heating and cooling requirements, it had been intended to use a set-up where an insulated metallic annulus surrounds the cylinder and heating elements. When heating, the air flow through the annulus is stilled; when cooling, a ducted fan blows through it. The 2180 W cooling requirement is relatively modest (comparable to a hand held hair dryer). The number of layers of fiber insulation (Johns Manville cerablanket) and the air flow rate would have been adjusted to accommodate to the loss rates determined by the actual heat transfer conditions found during set-up.

#### 4.3.4 Planned Operation Of The Test Rig

The test plan was to cycle the PCM module through 200 melting and freezing cycles, of the respective durations noted above. (This could be somewhat accelerated although the effect of thermal ratcheting can vary due to changing crystal structure with different freezing rates. Also, the supercooling effect noted below has a tendency to become more pronounced with increasing cooling rates.) The total time required for the cycling is 39.2 days, or about eight weeks. For safety it had been assumed that except for an initial preheat and final cool-down, the assembly would only operate during daytime hours on week days, i.e. when personnel would be available to occasionally monitor the equipment.

A strip chart would have been used to keep a record of the PCM and chamber temperatures. To improve safety the rig would have been operated in a room separate from the control equipment. (However, information provided by A. Ducao of Dynatherm Inc. indicates that fluorides are not particularly reactive with molten sodium.)

Before operating the system, the module would have been filled with PCM powder. Fluorides have a strong propensity toward reacting with residual water (producing hydrogen) and oxygen and thus an evacuation of the module while melting the PCM was planned. Following the recommendation of J. Daniel Whittenberger of NASA Lewis, it was intended to use an oil trapped roughing pump while holding the PCM for an hour or two at just above the melting point. Then the fill tube would have been pinched and welded closed.

There was some concern about whether the PCM would supercool to any significant degree, i.e. drop below its nominal melting point before beginning to freeze. The intention was to examine this in several freezing cycles before the main test began. The appearance of supercooling could affect the details of the automatic control scheme.

The nominal cycling process is presented in Figure 4.13. During melting, the controller would have been set to a temperature  $T_1$ , exceeding the melting point of the fluoride by some relatively small amount. It was expected that the temperature of the PCM would have flattened out as the melting point was reached and then remained there until melting was complete. The time for melting would have been adjusted to the desired value using a variac to set the power input given a quantity of insulation.

After melting the PCM temperature would have risen to  $T_1$ . At that point a switch

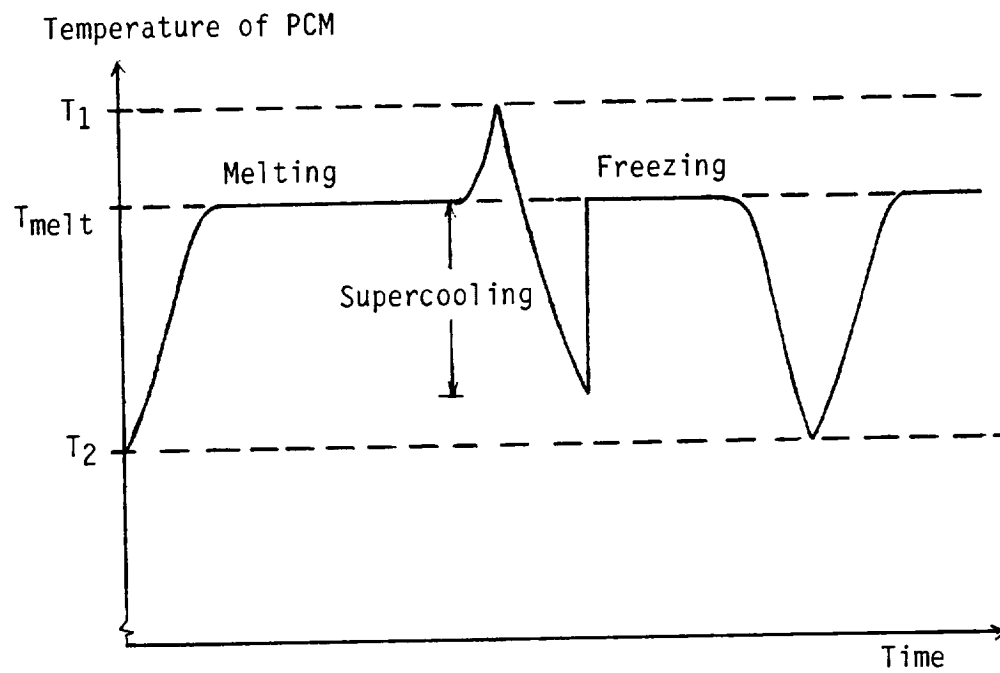


Figure 4.13 PCM Cycling Sequence

would have changed the controller setting to  $T_2$ , below the melting point. The heater would have gone off (or reduced to a much lower value) and the cooling air switched on. The power would have returned to its melting condition value and the air flow turned off when the PCM temperature dropped below  $T_2$ . To be certain that freezing had been completed the value of  $T_2$  would have had to be below the lowest temperature reached by the PCM during supercooling. Supercooling occurs as a statistical distribution and thus one might have to examine quite a few cycles to be reasonably certain that  $T_2$  were low enough. However, this requirement is not too stringent here, since even if the freezing were not fully completed the heating on the next cycle would still have been stopped when the PCM temperature reached it.

As a result of funding limits and the higher priority placed on the evaporator dome tests, NASA technical management requested that we not proceed with the PCM module test. All equipment was put into temporary storage for eventual shipment to NASA Lewis.

## Chapter V

### Evaporator Dome (Heat Pipe) Fabrication and Test

#### 5.0 Purpose and Approach

The other critical technology issue addressed in the research program was the fabrication and performance of the evaporator dome. The objectives were:

1. Fabricate two types of evaporator domes.
2. Test the operation of the domes at at least the nominal rated power level of the solar receiver of 38kW (equivalent to about  $32.5\text{W}/\text{cm}^2$  on the surface of a 29cm or 11.4" diameter hemisphere). If possible, test the evaporator to a level of about  $60\text{W}/\text{cm}^2$ , representative of the peak solar intensity on the receiver dome.

In the event, it was possible to only partially achieve the first objective and not to achieve the second. Two evaporator domes were successfully fabricated, but they were both of the screen wick design. A radiation source able to meet the difficult challenge of providing at least the equivalent of the nominal flux solar input was assembled and successfully tested. As in the rest of the program, given the technical hurdles to be overcome, early assessments of the time and cost required to meet the objectives were proved to have been significantly underestimated.

The approach for testing the receiver domes is illustrated schematically in Figure 5.1. A dome is welded into each end of a stainless steel cylinder, which is then placed over the heat flux source. Sodium evaporates from the wick, then condenses on the walls of the cylinder, which is radiating heat to the surroundings. The liquid falls down the walls and into a shallow pool at the base of the dome, whence it is drawn back up into the wick. The dome at the top end is highly insulated to avoid condensation and dripping onto the bottom one. Heat loss from the walls is regulated by a movable insulation box. (It had originally been planned to use a gas-gap calorimeter, but the cost was exorbitant.) The loss rate was to be determined using an IR thermometer and an estimate of convective losses. A similar camera was to be used to monitor the surface of the dome for localized overheating that would be an indication of incipient burnout of the wick. Such a failure would have been of concern not only to indicate wick performance but also as an essential safety measure to warn of melt-through and air-sodium contact. The cylinder would just be turned end for end to test the other dome.

Details of the intended test plan are discussed later in this chapter. A note on nomenclature; at various points in this report the test cylinder which includes the evaporator domes is referred to as a heat pipe, but since the cylinder does not use a wicking mechanism to return sodium to the evaporator (e.g. the walls are not covered by screen), it is not strictly a heat pipe. However, because of the wick on the domes neither is it a pure reflux device. It thus became common usage to refer to it as a heat pipe.



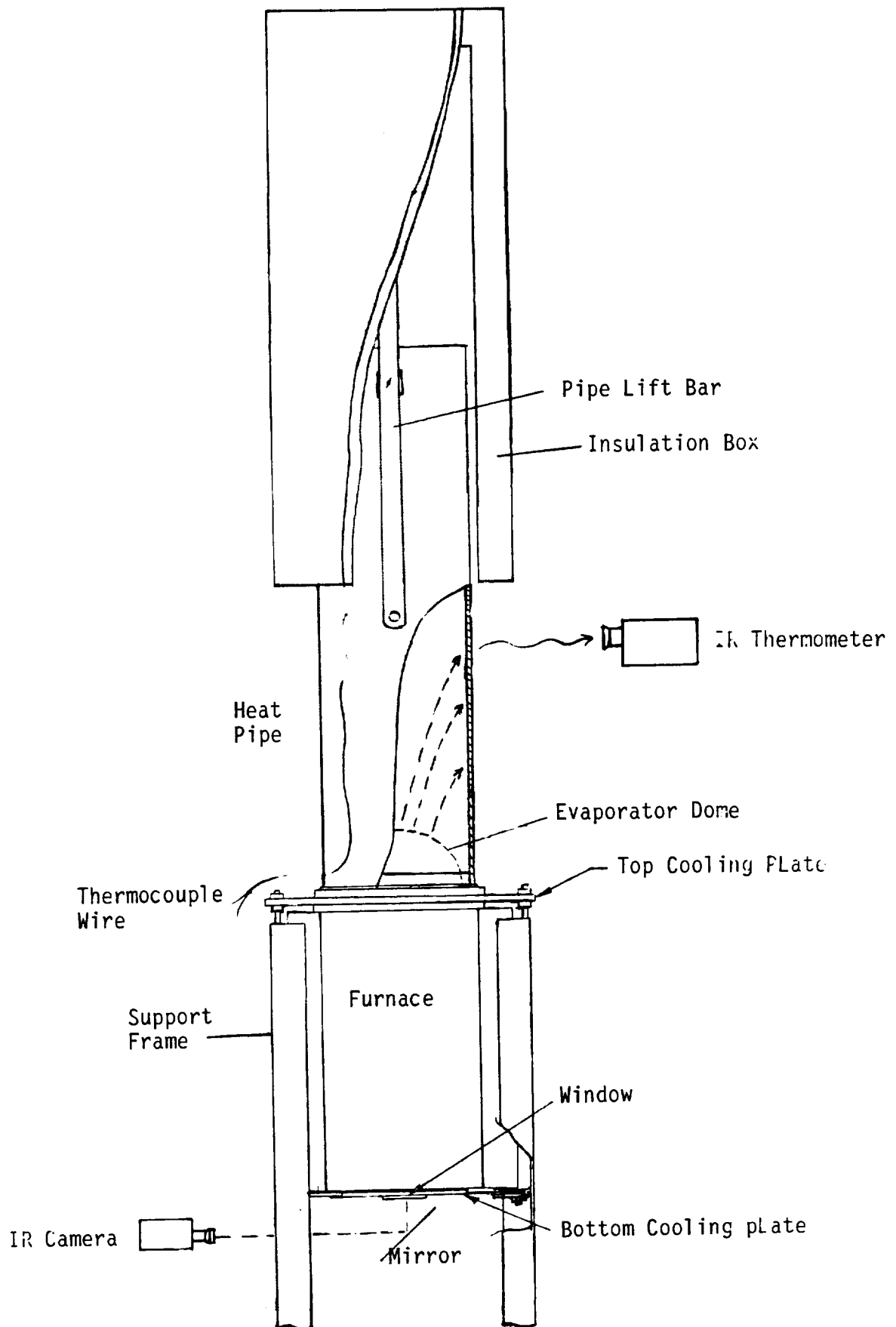


Figure 5.1 Heat Pipe Test Concept

## 5.1 Evaporator Dome Designs

### 5.1.0 General Remarks

The detailed design of the evaporator dome wicks is described in the following sections. All of them were conceived as 'composite' wicks; they both use several layers of fine 400 mesh screen at the evaporator surface to achieve high pumping capability and a different type of material underneath to reduce sodium flow losses. The common evaporator mesh results in a common pumping capability, which is discussed in this section.

The pressure difference across the meniscus at the screen is given by

$$P_v - P_l = \frac{2\sigma\cos\theta}{r_e}$$

where the vapor and liquid pressures are  $P_v$  and  $P_l$  and  $\sigma$  is the surface tension. The contact angle  $\theta$  and effective bubble radius  $r_e$  will drop from the entrance to the apex of the screen as the value of  $P_l$  drops due to flow losses as well as gravitational head, if present. This is illustrated in Figure 5.2, (derived from Ref. 10), where it is seen that as the liquid pressure drops the menisci are gradually drawn into the screen. It is generally assumed that the maximum pumping capability is given by letting  $r_e$  be defined as half the mesh spacing, i.e.,

$$r_e = \frac{1}{2M}$$

where  $M$  is (for example) 400 wires/inch, and that the contact angle is zero degrees. The rationale for this definition of  $r_e$  is that at the limit adjacent bubbles end up touching each other at a ninety degree angle, behind the screen. If these assumptions are applied to the present design, then we obtain a maximum value of the pumping capability  $P_v - P_l$  of  $1.291 \times 10^4 \text{ Pa}$  (0.127 atm.) at 1073K.

Several notes should be appended to this estimate. First, when the wire diameter is of the same order as the wire separation, it appears that the maximum pumping capability may be given with  $r_e$  defined as half the distance between wires ( $1.905 \times 10^{-5} \text{ m}$  or 0.00075"). Here that would increase the pumping capability by 2/3.

Second, however, another consideration may countervail this result. Due to the multiple layers of 400 mesh, the meniscus may not in most areas be able to draw fully behind the screen, effectively preventing  $r_e$  from becoming as small as first considered. But the present author suspects that the multiple layers will result in a complex liquid-vapor interface with an effective value of bubble radius considerably smaller - and thus a pumping capability considerably larger - than with one layer of screen.

The planned size of the domes (inner measurements) was 29cm (11.4") diameter, but

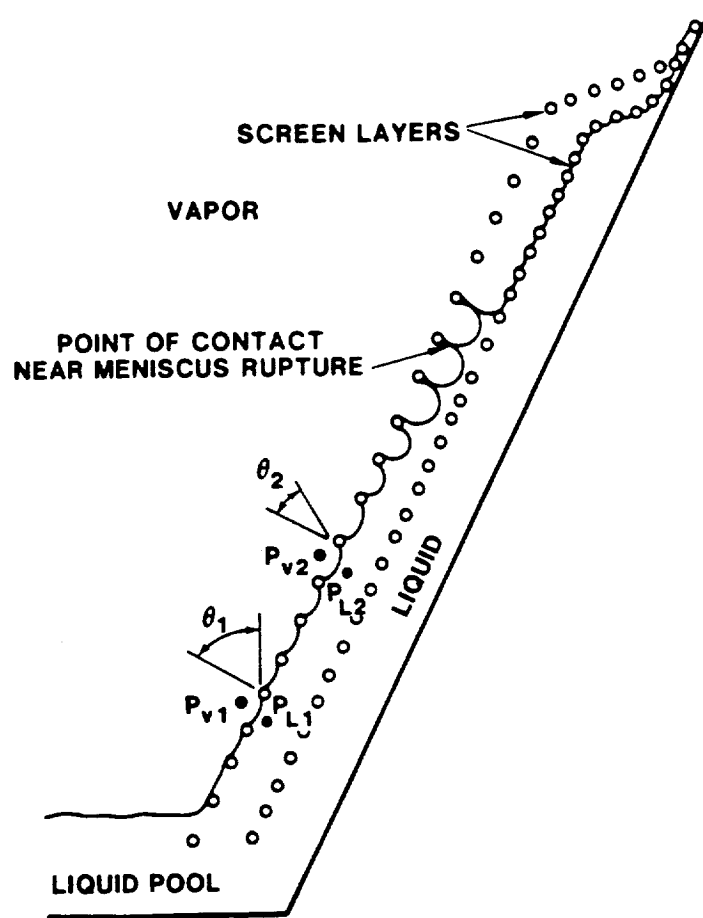


Figure 5.2 Variation of Meniscus Shape along  
Liquid-vapor Interface on a Screen  
Wick (Adkins, Ref. 10, p. 10)

the final height of 13cm (5.1") was slightly less than the radius due to caution in the forming process.

### 5.1.1 Screen Wick Designs

#### 5.1.1.1 Components

Two types of screen wicks were planned and fabricated. Both are composite designs, having a fine surface mesh for sodium pumping and a wider mesh below to reduce pressure losses as the sodium flows along the dome surface. These wicks are referred to as Assemblies 1 and 2, and have the following stacking sequences, starting at the bottom (inconel plate) side;

##### Assembly 1

1. Inconel 617 sheet, .127cm (0.050") thick
2. Four layers of 100 (wire/inch) mesh, Ni 200, wire diameter 0.0114cm (0.0045")
3. One layer of 100 mesh, Ni 200, calendered by about 25%
4. Two layers of 400 (wire/inch) mesh, stainless 316, wire diameter 0.00254cm (0.001")

##### Assembly 2 (nominal gauges of materials identical to Assembly 1)

1. Inconel 617 sheet
2. One layer of calendered 100 mesh, Ni200
3. Three layers of uncalendered 100 mesh, Ni200
4. One layer of calendered 100 mesh, Ni200
5. Three layers of calendered 400 mesh, stainless 316

The assemblies are shown schematically in Figure 5.3 . The successive layers of a particular mesh were laid down at 45° angles to one another to avoid interlocking of wires. 'Calendering' is the flattening of the screen by a particular amount; it has the effect of increasing the area touching adjacent plates or screens, thus potentially increasing the effectiveness of sintering. Using multiple layers of the fine mesh at the surface reduces the chance of a defect (larger pore size) causing locally reduced pumping, reduced sodium flow and dryout that could result in dome melting.

Assuming that the nominal thickness of a mesh is given by twice the wire thickness times the calendering factor, the thickness for both assemblies is about 0.119cm (0.047").

Performance of these assemblies is now estimated.

#### 5.1.1.2 Characteristics

In addition to the pumping wick capability discussed earlier, several other important parameters may be identified. Please note that these estimates cannot substitute for

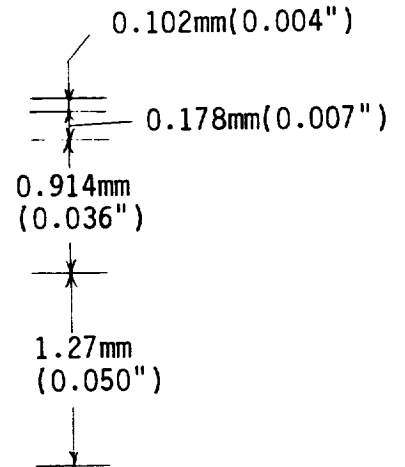
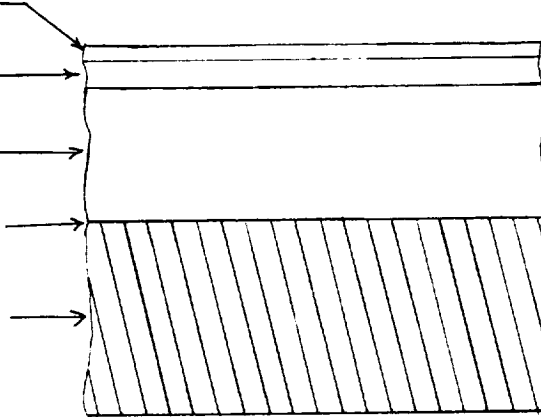
2 layers 400 mesh  
Stainless 316

1 layer calendered  
100 mesh Ni200

4 layers 100 mesh  
Ni200

Ni layer, 0.013mm  
( $\frac{1}{2}$  mil)

INCONEL 617



a. Assembly 1

3 layers 400 mesh  
Stainless 316

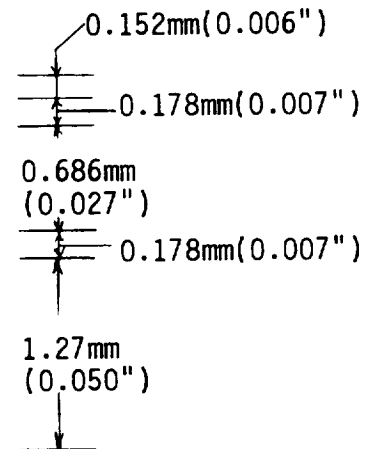
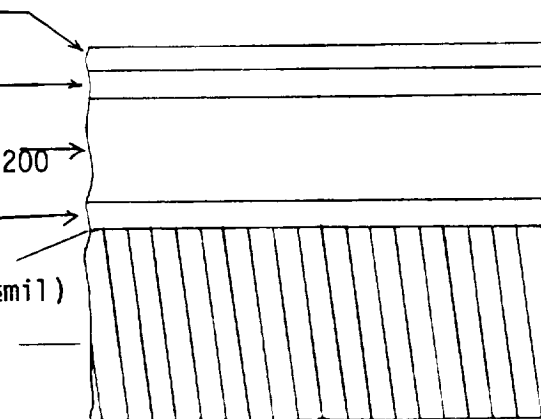
1 layer calendered  
100 mesh, Ni200

3 layers 100 mesh Ni200

1 layer calendered  
100 mesh, Ni200

Ni layer, 0.013mm ( $\frac{1}{2}$ mil)

INCONEL 617



b. Assembly 2

Figure 5.3 Screen Wick Assemblies

actual testing of the screen.

First, consider the superheat ( $\Delta T_{sp}$ ) developed across the wick. (It is assumed that sodium flow rates are slow enough that a pure conduction estimate can be made.) This value may be formulated as

$$\Delta T_{sp} = q \sum_m \frac{t_m}{k_{em}}$$

where  $t_m$  and  $k_{em}$  are the thickness and effective thermal conductivity of a layer  $m$  (which may consist of several layers of a particular material) and  $q$  is the heat flux per unit area across the dome. The conductivity is an effective one since it must combine the contributions of both the metal screen and the sodium. Adkins in Ref. 10 presents an approximation for  $k_e$  which in the present nomenclature is

$$k_{em} = k_l \frac{[(k_l + k_w) - (1 - \epsilon_m)(k_l - k_w)]}{[(k_l + k_w) + (1 - \epsilon_m)(k_l - k_w)]}$$

given a porosity of  $\epsilon_m$  for layer  $m$ ,  $k_w$  for the wick conductivity in that layer and  $k_l$  the sodium conductivity. Later in this report, the porosity of individual screen layers is calculated to be

100 mesh	61.23%
100 mesh, calendered	48.51%
400 mesh	66.17%

Here screen layers of a particular porosity and material are bunched together in calculating  $k_e$  using the thermal conductivities near the heat pipe operating temperature of 58 W/m·K for sodium, 23 W/m·K for Ni and 60 W/m·K for stainless 316 (both of the latter values from Touloukian, Ref. 19). This results in  $k_e$  - 43 W/m·K for the 400 mesh layers and 59 W/m·K for the others. Assuming a thickness of twice the wire diameter times the calendering factor reduction for each layer and that  $q = 30.4 \text{ W/cm}^2$  (40 kW total input) gives a superheat of 6.3 K for Assembly 1 and 6.4 K for Assembly 2. This means that the superheating will exceed our limit of 10 K if the peak fluxes are about double the average value.

Adkins also presents an empirical expression for estimating the permeability,  $\kappa_w$ , of screen wicks with diameter  $d$ , namely,

$$\kappa_w = d^2 \frac{\epsilon^2}{122(1 - \epsilon)^2}$$

where  $\epsilon$  is porosity. After averaging together the porosities of the 100 mesh calendered and uncalendered screens (weighting by thickness) the result is a porosity

of  $1.333 \times 10^{-10} \text{m}^2$  for Assembly 1,  $1.064 \times 10^{-10} \text{m}^2$  for Assembly 2. The permeabilities of the 400 mesh evaporator screens are an order of magnitude lower at  $1.339 \times 10^{-11} \text{m}^2$ , so flow through them will be negligible.

Finally, for operation in 1g conditions, the self-priming height is of interest. This is just the height to which the sodium will be drawn by capillary action when the dome is put into a pool of the liquid metal. For a liquid surface with radii of curvature  $r_1$  and  $r_2$ , this height is

$$h = \frac{\sigma \cos \alpha}{\rho_l g} \left( \frac{1}{r_1} + \frac{1}{r_2} \right)$$

For sodium at 1073K and both radii set at the single value of half the wire separation in the 100mesh,  $h$  is as high as 1.74m if the contact angle  $\alpha$  is close to zero degrees.

Performance of the screen wicks is summarized in Table 5.1.

### 5.1.2 Electroformed Wick Design

The second wick design selected replaced the 100 mesh wick with channels on the surface of the dome. The concept is illustrated in Figure 5.4, which shows two layers of 400 mesh stainless 316 overlaying a 0.0254cm (10mil) high, interlocking diamond pattern that is electrochemically deposited (electroformed) onto the surface of an 0.0762cm (0.030mil) Inconel 617 plate. The screen was to be sintered onto the plate before hydroforming the entire assembly. Due to problems with the electroforming step (described later) fabrication of this design was not completed.

Compared with the screen wicked domes, the thickness of the sodium flow layer was less, and thus superheating of sodium would be less. Since the conductivities of the sodium and the nickel at the operating temperature are virtually equal (we assume here  $59 \text{W/m}\cdot\text{K}$ ) the temperature rise is very simple to calculate as 2K at the average flux level for 40kW overall power level (this includes the effect of the 400 mesh layers). Moreover, even at the doubled peak flux estimate this leaves substantial margin before reaching the 10K limit.

The 1-g wicking limit may be found by taking the radii of curvature at the widest point in the flow path ( $l_w$ ) in the figure. Assuming a  $0^\circ$  contact angle gives a value of 0.51m.

## 5.2 Evaporator Dome Fabrication

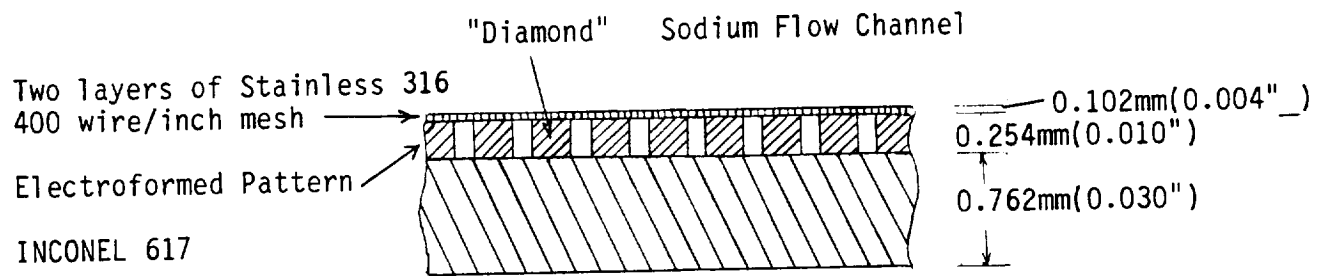
### 5.2.1 Screen Wick Dome Fabrication

A significant amount of development was required to fabricate the screen wick domes. In outline, the process was;

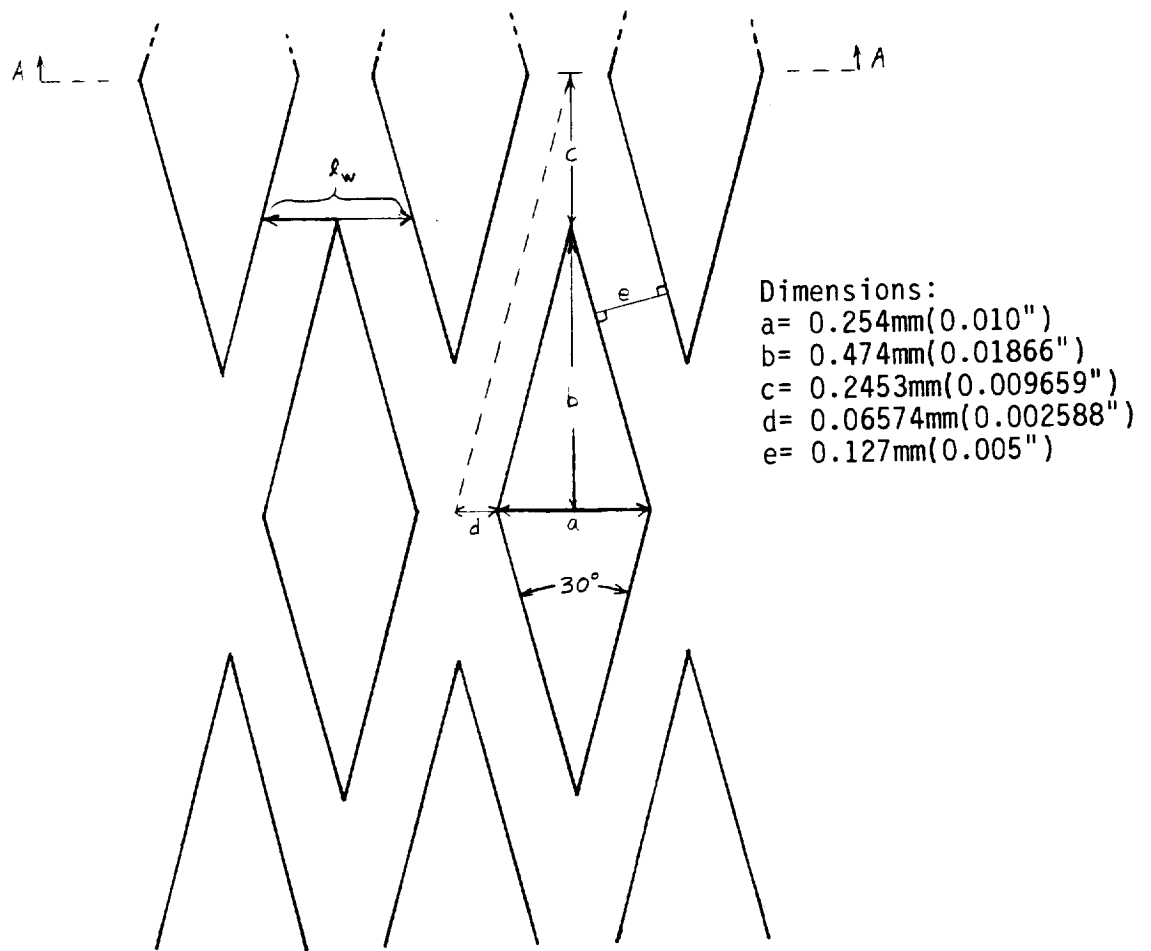
Table 5.1 Screen Wick Evaporator Performance

	<u>Assembly 1</u>	<u>Assembly 2</u>
Evaporator Wick Pumping Capability (Pa)	$1.291 \times 10^4$	$1.291 \times 10^4$
Superheating (degrees K)		
at 30.4 w/cm <sup>2</sup>	6.3	6.4
at 60.8 w/cm <sup>2</sup>	12.6	12.8
Permeability (m <sup>2</sup> )	$1.333 \times 10^{-10}$	$1.064 \times 10^{-10}$
Maximum Wicking Capability (m)	1.74	1.74





a. Cross-Section of Stacking (Through Section A-A below)



b. Electroformed Pattern

Figure 5.4 Electroformed Wick Design

- a. Application of Ni layer on IN617 plate.
- b. Stacking and sintering of wick layers.
- c. Impregnation of wick with paraffin.
- d. Hydroforming of dome.
- e. Cleaning of wick and stress-relief anneal.
- f. Cut-back of wick.

An attempt to hydroform the dome in one step failed due to the work hardening of the Inconel alloy. A series of tests resulted in a process repeating parts c, d and e three times so that the dome was formed in stages.

The process is discussed in more detail below:

#### 5.2.1.1 Application of Ni Layer on IN617 Plate.

This was recommended by the Facet Company as an aid to sintering the screens to the plate. A 0.5 mil layer was deposited on the surface of the IN617 plate by a local vendor. To insure proper adhesion had occurred we performed a bend test on the alloy; in one case there had been an unsatisfactory deposition.

#### 5.2.1.2 Stacking and Sintering of the Wick Layers.

Early, subscale tests of hydroforming our screen wick layers showed a tendency for the top 400 mesh material to rip near the base of the dome. In an attempt to avoid this on the full scale system it was decided to sinter the mesh layers together and to the adjacent dome.

The screen layers were cut as 48cm (19") diameter circles and laid onto the plate. As each was put down, it was spot welded to the surface within 0.6cm (1/4") of its perimeter. These screens were not perfectly flat, but the major deviations could be eliminated by the use of a hand held pressure plate (of the screen diameter but only a few inches wide) and proper sequencing of the welds. The rest of the deviations were eliminated in the sintering process, which consisted of raising the piece to ~1464K (21750F) under high pressure for several hours. (The details of the process are proprietary to Facet Inc., of Greensboro, NC, but it is clearly of the general type known as a 'hot isostatic press').

Facet performed the layup and welding as well as the sintering of the screens. Problems were noted with one of the first two sintered stacks that they completed (Assembly 1 type): first, the 400 mesh layers were missing; second, there was an approximately 0.5cm diameter area where it appeared that a metal had melted into the screen, though it did not look like it was wholly blocking the pores. Also, there were several scratched lines on the screens, though none that had changed the pore sizes.

Sanders staff should have visited and surveyed their facility before allowing them to proceed with fabrication; we did visit them before they prepared a substitute for Assembly 1 (which had been destroyed in an early hydroforming attempt; see below). It was obvious that contamination of the screen with foreign material could easily occur at their facility if they did not fully understand the requirements. There were

small metal chips and fragments present on the work tables. It also did not help that the work areas available to their engineering (as opposed to manufacturing) staff were in flux. That is not to say that their facilities were inadequate to the task; overall they were impressive and appeared well organized. But an early visit would have been able to clarify ambiguities in their understanding of the requirements. A member of our engineering staff was able to supervise the layup of the replacement assembly and prevent contamination.

#### 5.2.1.3 Impregnation of the Wick with Paraffin.

Other researchers have encountered difficulty in forming screened wick domes while preventing large losses in fluid permeability through the coarse mesh layer. For example, D.R. Adkins of Sandia Laboratories measured a loss in permeability by a factor of ten (Ref. 20). To counter this crushing effect in the present program paraffin was frozen into the screen. Early testing on subscale screens (without a baseplate) showed little or no displacement of the wax out the edges during the forming.

Application of the wax to the screen must be done with care to avoid air bubbles. Given the peculiarities of wax behavior development of a precise process would have required considerable time and effort. Nonetheless, it is believed that the results were good. To keep track of the efficiency of the technique the screen was redipped back into the wax; a poor fill would result in the appearance of numerous air bubbles along the surface.

The final process was:

1. Prepare a tank of melted wax at a temperature of about 65-70°C (150-160°F). The tank used was designed for vertical dipping of the plate.
2. Preheat the side of the plate not covered with sintered screen using a heat gun. This will promote wicking of the wax through the screen while reducing the chances of bubbles next to the relatively high thermal mass plate.
3. With its surface held vertically, lower the plate into the wax. This should be done slowly enough that the wax wicks up ahead of the fluid line.
4. Let the plate soak in the wax for about ten minutes.
5. Pull the plate out and turn it horizontally as rapidly as possible to minimize wax dripping out of the screen.
6. Set the plate down, screen side up, over a fan. The air flow from the fan will cause the wax to cool from the back (plate side) to the front of the screen, so that voids will not be trapped as the wax cools and shrinks. In parallel, molten wax should be poured on any areas that are not covered with at least a thin layer of it (whether a liquid or a solid). It will be seen that as the wax freezes it tends to shrink down into the screen; to prevent voids in the screen we supply fresh wax.
7. As the excess wax freezes on the surface, it can be scraped off with a plastic sheet that is relatively stiff but not so hard as to damage the screen. When

removing a heavy layer of wax it will often be found that it is still liquid below. Until it freezes, this liquid should not be removed since the wax below it, in the screen, may still be molten and require a continued supply to fill voids.

8. Clean off the completely frozen wax until it is down to the surface of the screen.
9. To check the effectiveness of the impregnation, the plate can be redipped into the wax. This doesn't have to be done as slowly as the first time. With a poor impregnation, small bubbles will be seen coming out of the edge of the screen. However, this is unlikely if the procedure was carefully followed, and a redip is probably most useful when first becoming familiar with the process.

#### 5.2.1.4 Hydroforming of Dome.

A great deal of effort was required to obtain a successful hydroforming of the Inconel plate with sintered screen. The stages of the hydroforming process are outlined in Figure 5.5.

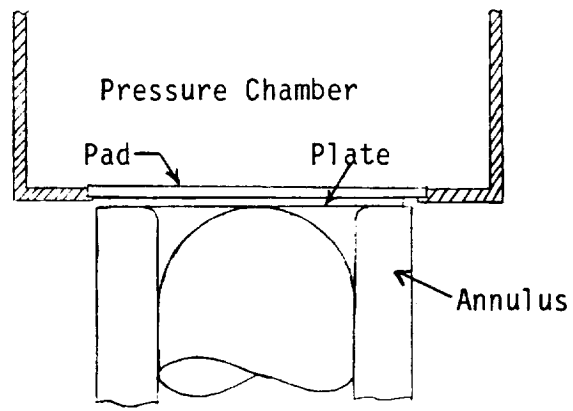
A circular plate is placed on an annular platform and evenly subjected to anywhere from several tens to several thousands of psi from a flexible pad on the underside of the pressure chamber above. At this point, the hemispherical ram used to produce the desired shape is at a neutral position with its peak at the level of the annulus. The pressure from the pad causes the metal to partly deform down over the surface of the ram, drawing in metal from the sides.

Then the ram is forced up through the center of the annulus to the selected height. This causes the pressure behind the pad to rise; the machine may be set to prevent it from exceeding a desired level.

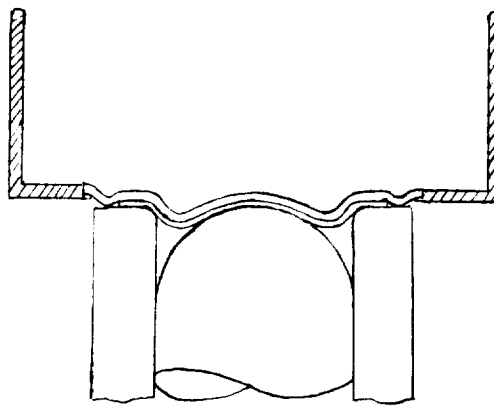
Several factors enter into having a successful forming. First one must start with a pad pressure high enough that wrinkling is prevented when the plate metal is drawn in from the annulus and up and over the ram. On the other hand an excessively high pad pressure can prevent the metal from drawing in easily enough and lead to breakage, either at the start as it flexes downward, or during ram operation if this flexed reservoir of metal is depleted. Second, work hardening of the metal can also result in breakage, as was discovered in our attempt to produce the Inconel dome in one hydroforming step. Third, surfaces must be clean of solid debris to prevent local deformation or scraping of the plate. Lubrication is also required to allow the plate to flow over the other surfaces, but excess lubrication can cause local impressions in it by trapping oil bubbles.

To provide added protection of the screen wick, it was covered by an 0.102cm (0.040") 6061-T4 aluminum plate during hydroforming. This material is much more pliable than the Inconel, but hard enough to prevent the screen from sticking to it. Lubrication on each of the facing surfaces of the plates and under the Inconel was provided by a vegetable oil, instead of the regular sulfur containing oil that might have affected later annealing. The regular oil was applied to the top surface of the aluminum.

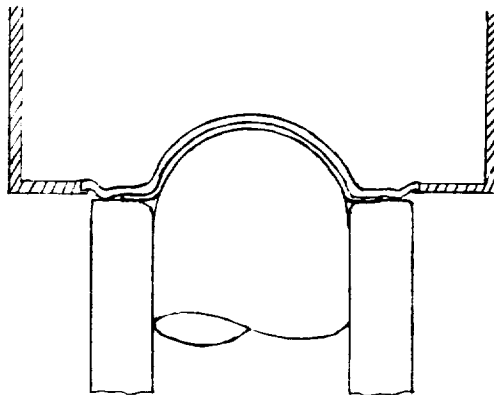
Subsequent to each forming step the dome was subjected to a stress relief vacuum



1. Starting Condition



2. Pressurization



3. Forming

Figure 5.5 Hydroforming Process

anneal at 1900°F (1311K) for 1/2 hour followed by an argon quench. According to INCO technical staff, this should be sufficient for our heat pipe operating temperature. Before each anneal, the screen was cleaned of wax using a hot water spray followed by a degrease.

Table 5.2 lists the hydroforming parameters used. Note that a final anneal was performed after the last forming, to ease stress on the dome before being welded into the heat pipe tube.

#### 5.2.1.5 Cutback of Wick

After the final forming and anneal the flanges on the domes were cut back to the required size for welding into the test cylinder. Then the wick had to be cut to a smaller diameter. One of the surplus aluminum domes from the forming process was cut to this diameter, then a scribe was used to mark the screen.

To reduce blockage of the wick passages by metal bent during cutting, the wick layers were cut one or more at a time, by hand, using an Exacto knife. (The 400 mesh layers were too tightly sintered together to cut individually.) Each layer was then carefully pulled off of the one below.

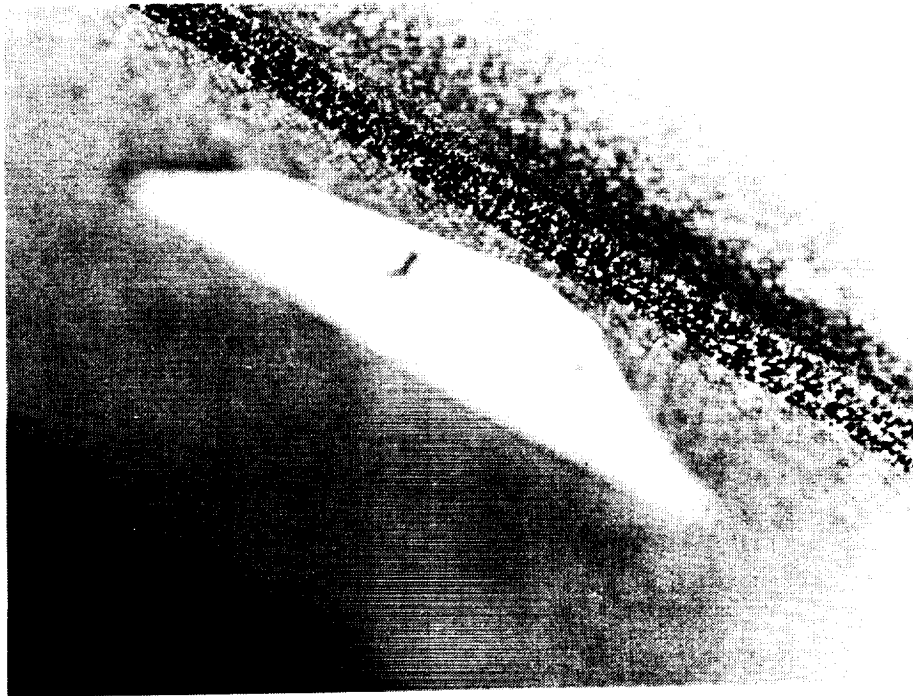
For Assembly 1 this proceeded relatively smoothly. On Assembly 2, however, the bottommost layer of screen (100mesh) could not be pulled off by hand. At one point heating of a small area with a torch was tried, at another, sanding it off. In the end, what worked was chiseling it. It is likely that the greater adhesion of this screen was due to the calendaring, which would have allowed it to sinter to the inconel over a greater area than that for the corresponding layer in Assembly 1.

The edges of the wicks for the two assemblies are shown in Figures 5.6 and 5.7. (Please note that by error the labels visible in the photos were reversed, e.g. A2 is actually Assembly 1) Part a of Figure 5.6 shows an edge typical of most of the circumference of Assembly 1. There is some blockage from the wire cutting process. The dot pattern on the inconel which extends from the edge and becomes blurred as it approaches the camera is caused by the spots where the screen had sintered to the plate. An idea of the scale may be obtained by considering that the screen thickness in this region was close to its initial (calculated) value of 1.19mm (0.047"). Part b of the figure shows a part of Assembly 1 where the screen had become detached from the plate.

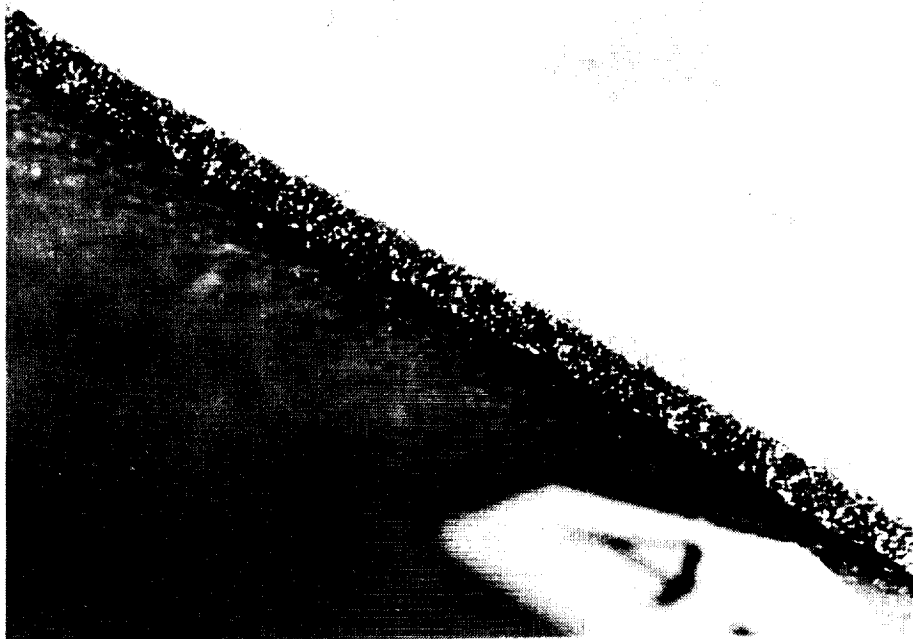
When the edge photos were taken of Assembly 2, the bottom layer of screen had not yet been removed. Much of the edge along the circumference appeared similar to that of Assembly 1, as can be seen in Figure 5.7a. But along most of the circumference there were anomalies worse than in Assembly 1, such as that shown in part b of the figure. These apparently occurred when removing the excess wick material; a particular layer's wires might have been cut from those of the adjoining screen that was to remain in place, but it could still pull on the screen sintered to it below, and that screen could then tug and distort the adjoining screen. This kind of anomaly along the edge was worse in Assembly 2 since the screen just above the lower calendared screen was harder to pull off. It did not appear that the separation from the plate shown in Assembly 1 or the gaps within the screen shown in Assembly 2 extended into the area of the dome itself. (This was based upon a visual survey rather than measurement, but it is considered likely since the pulling of the screen

Table 5.2 Hydroforming Parameters

	Stage I			Stage II			Stage III		
	Ram Displacement	Pad Pressure (psi)		Ram Displacement	Pad Pressure (psi)		Ram Displacement	Pad Pressure (psi)	
		"Charging"	Final		"Charging"	Final		"Charging"	Final
Assembly 1	1.0"	500	2000	3.4"	600	7500	5.1"	600	12,200
Assembly 2	1.0"	500	2200	3.4"	600	7500	5.1"	600	12,200



a. Good Adhesion

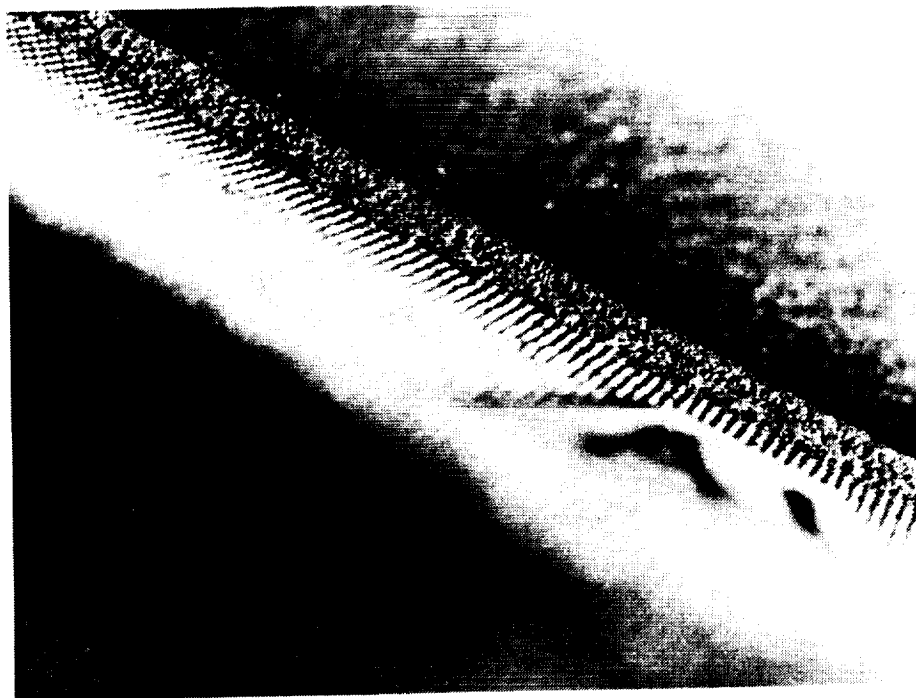


b. Separated

Figure 5.6 Edge of Formed Wick on Assembly 1



ORIGINAL PAGE  
BLACK AND WHITE PHOTOGRAPH



a. Normal Area



b. Disturbed Screen

Figure 5.7 Edge of Formed Wick on Assembly 2

was fairly localized.) If either had occurred in that ( high energy flux) area, the greater local depth of sodium during testing could cause superheating and bubble formation with possible burn-through.

Partial blockage of the screen edge by the cut and bent wires should not be a problem during heat pipe operation as long as a pool of sodium remains in the annulus near the cylinder wall; the liquid would just enter the screen through the small holes but large area of the 400 mesh.

#### 5.2.1.6 Dome Condition

The finished domes are shown in the photograph, Figure 5.8. Assembly 1 is at the right and Assembly 2 at left. The light patterns are due to the reflection within the screen. The circular marking at the apex of Assembly 1 is a stain from the permeability test described in the next section. Overall, the screen appeared to be in remarkably good condition. The deformation had caused some 'orange skin' effect on the inconel, visible on the concave surface of the domes.

#### 5.2.1.7 Evaluation of Screen Wicked Domes

Two measurements were made to evaluate the quality of the fabricated domes and provide information for future analyses of the heat pipe receiver.

In the first, the thickness of the screen and substrate dome was measured along a meridional line from the hemisphere apex, then compared with the metal thickness of an earlier formed bare Inconel dome to derive the screen depth. These results are summarized in Table 5.3 and Figure 5.9. For comparison, the thickness of the prehydroformed assemblies are both calculated as 1.194mm (0.047"). In accord with the recommendation of the manufacturer it was assumed that a screen thickness was given by twice the wire diameter times a calenderizing factor, where appropriate. (The latter was 75% according to the sintering vendor.) The actual screen thickness after sintering but before hydroforming should have been measured but was not.

Evidently, the worst screen crushing occurred for both domes at a distance of about 7.6cm (3") from the apex, amounting to about 22% of the initial value; at the center it was about 17%. These results are considerably better than the 50% crushing obtained by Adkins at the Sandia Laboratories after hydroforming of a (somewhat coarser) screen wick without wax impregnation (Ref 20).

The data for the wicked dome thickness was obtained by using two opposing spheres; for the bare dome it was a sphere and a flat plate. At a given point the normal line was determined by adjusting the dome's angle until the lowest value appeared on the digital readout; these are the values recorded. The measuring equipment actually read to another digit (in inches) beyond that shown, so presumably its inherent accuracy was better than  $\pm 1$  mil. Given this situation it would be inappropriate to assign a conventional plus or minus accuracy value to the data. Using the experience gained during multiple measurements at a given point, it was concluded that the recorded values for total thickness may be high by 1-2 mils ( $2.54\text{-}5.08 \times 10^{-2}\text{mm}$ ) at most, and thus the derived screen thicknesses may be high by a maximum of 2-4 mils ( $5.08\text{-}10.2 \times 10^{-2}\text{mm}$ ). In addition there were a few localized depressions in the screen, evidently where wax had not penetrated as effectively prior to one or another hydroforming step. The worst of these resulted in a screen compression of about 5

ORIGINAL PAGE  
BLACK AND WHITE PHOTOGRAPH

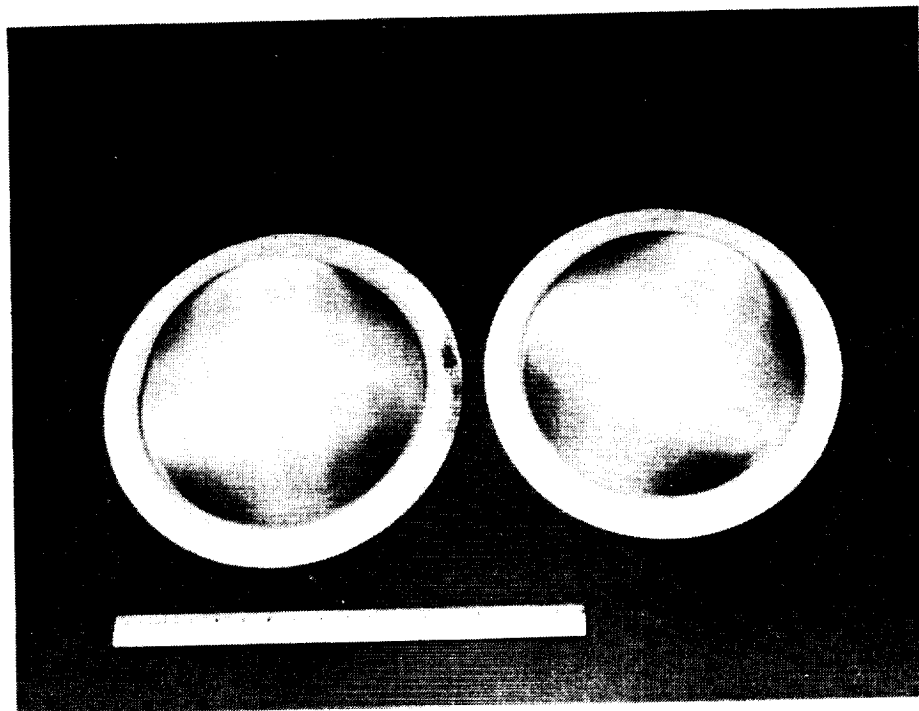


Figure 5.8 Domes Formed (Assembly 1  
at right, Assembly 2 at left)

Table 5.3 Measured Dome Thickness and Derived Screen Thickness

(measured in inches)

Distance from Apex		Bare Dome		Assembly #1				Assembly #2			
				Total		Screen		Total		Screen	
cm	in	mm	in	mm	in	mm	in	mm	in	mm	in
0.0	0.0	1.168	0.046	2.184	0.086	1.016	0.040	2.159	0.085	0.991	0.039
2.5	1.0	1.143	0.045	2.210	0.087	1.067	0.042	2.134	0.084	0.991	0.039
5.1	2.0	1.118	0.044	2.159	0.085	1.041	0.041	2.159	0.085	1.041	0.041
7.6	3.0	1.168	0.046	2.108	0.083	0.940	0.037	2.108	0.083	0.940	0.037
10.2	4.0	1.041	0.041	2.184	0.086	1.143	0.045	2.159	0.085	1.118	0.044
12.7	5.0	1.092	0.043	2.210	0.087	1.118	0.044	2.210	0.087	1.118	0.044
15.2	6.0	1.067	0.042	2.210	0.087	1.143	0.045	2.210	0.087	1.143	0.045
*17.8	7.0	1.067	0.042	2.261	0.089	1.194	0.047	2.438	0.096	1.372	0.054
*20.3	8.0			2.286	0.090			2.337	0.092		
*"mid-curve"		1.143	0.045	2.286	0.090	1.143	0.045	2.489	0.098	1.346	0.053
Error bars		$\pm 0.025$ -0.051	$\pm 1-2$ mil	$\pm 0.025$ -0.051	$\pm 1-2$ mil	$\pm 0.051$ -0.102	$\pm 2-4$ mil	$\pm 0.025$ -0.051	$\pm 1-2$ mil	$\pm 0.051$ -0.102	$\pm 2-4$ mil

"Mid-curve" refers to about 45 degrees along the curve between the dome and the flange.

\* Screen may have separated from surface.

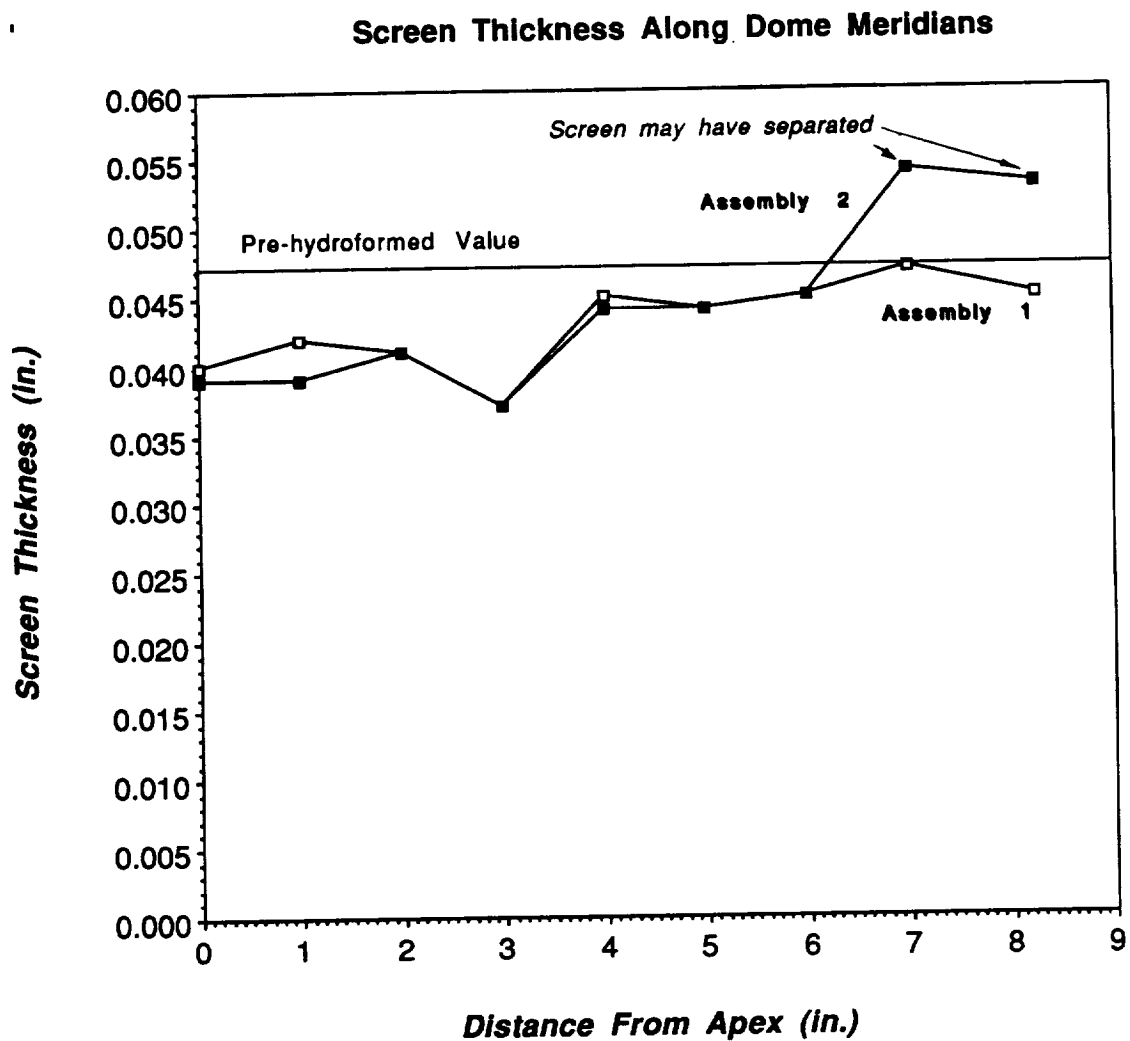


Figure 5.9 Screen Thickness After Forming

mils below the local mean surface.

The second measurement made was of dome permeability using the technique and formulation derived by Adkins. The equipment was set up as in Figure 5.10 adapted from one of his documents (Ref. 20). In principle this test is simple. Fluid (methanol or isopropanol) is added to the basin until it wicks up to the level of the inverted transparent vessel at the top of the dome. This vessel is sealed to the wick using a soft gasket material and downward pressure rather than a semi-liquid sealant that would be difficult to clean off. A vacuum is applied that is adequate to fill the vessel with liquid just to the level of the tube leading off to the graduated cylinder. An excessive vacuum results in air being drawn across meniscus at the wick surface and up into the vessel.

The measurements made during the test are of volume flow rate,  $\dot{V}$  (ml/sec or m<sup>3</sup>/sec) and the pressure "head"  $H_L$  (m) required to sustain this flow rate through the wick. The latter quantity is the measured "head" being drawn (in meters of methanol) after subtracting out the height 'h' that the fluid must climb from the liquid surface to the connecting tube into the graduated cylinder. Data were taken in 'sequences' that represented flow rates and pressures read sequentially as a graduated cylinder was filled.

Combining these measurements with the known viscosity of the fluid,  $\nu_l$  and the gravitational constant  $g$ , Adkins obtained the following formulation for the product of permeability and wick thickness (assuming this thickness is constant along the flow path),

$$\kappa_w \delta_w = \frac{\nu_l \dot{V}}{2\pi g H_L} \ln \frac{\tan(\alpha_o/2)}{\tan(\alpha_i/2)}$$

The angles  $\alpha_o$  and  $\alpha_i$  are shown in the figure (the radius of curvature of the domes are slightly larger than half the base diameter since they were formed to 12.95cm height rather than 14.48cm).

In practice several difficulties were encountered. First, lower or higher flow rates for a given pressure sometimes occurred, evidently a result of leaks in the pressure line attachments. Second, after performing the tests we learned that the methanol viscosity could be substantially decreased by contact with PVC plastic. It is not clear whether such contact occurred in our work. In any case time constraints prevented us from performing any more tests. With these provisos we present the data in Table 5.4, which does not include readings taken when bubbles were seen entering the inverted vessel or test sequences that showed significantly lower flow rates than others with the same or lower pumping pressure. Both phenomena indicate an air leak in the system. The reason for the downward trend in the value of  $\kappa_w \delta_w$  within each sequence is not clear, but it probably indicates a systematic error. The error bars shown in the table are based only upon estimates of accuracy in reading the data from the measuring devices.

The value of  $\kappa_w \delta_w$  is greater for Assembly 2 than Assembly 1, a result that is opposite to that expected (for the close values of  $\delta_w$  for the 100mesh) based upon the

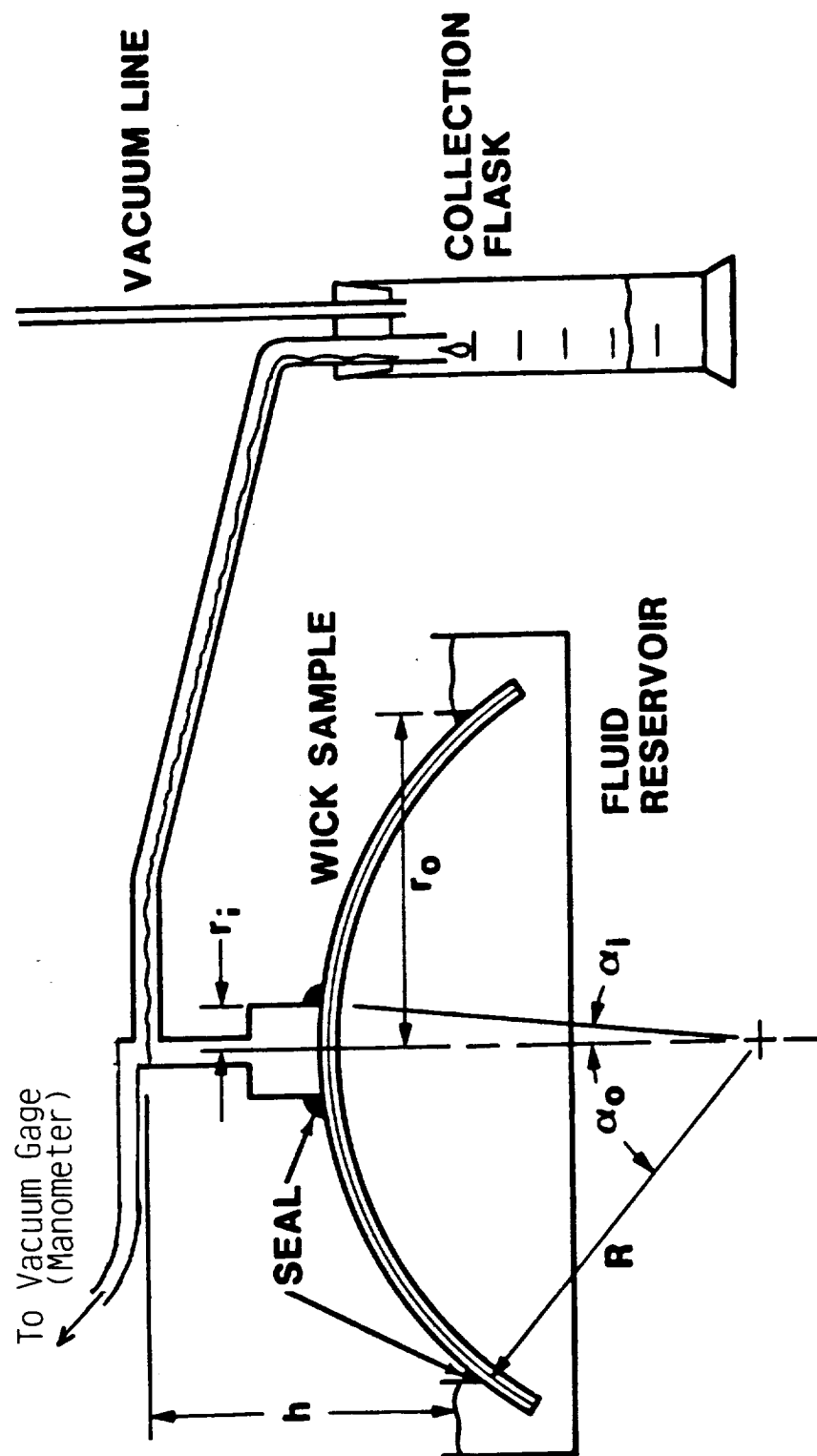


Figure 5.10 System for Measuring the Permeability of a Dome-shaped Wick [Ref. 20]

Table 5.4 Product of Permeability and Thickness of Screen Wicks

Assembly	Test Sequence	Temperature $t_C$	Kinematic Viscosity $m^2/s$	Measured Head Drop $(H_L)m$	Measured Volume Flow Rate, $V \text{ m}^3/sec$	$Ks \text{ (m}^3\text{)}$
1	1	16	$8.176 \times 10^{-7}$	0.1914 0.2026 0.2553 0.2553 0.2553	$0.4255 \times 10^{-6}$ $0.4211 \times 10^{-6}$ $0.3960 \times 10^{-6}$ $0.3738 \times 10^{-6}$ $0.3960 \times 10^{-6}$	$51.1 \pm 9.5 \times 10^{-15}$ $47.8 \pm 8.8 \times 10^{-15}$ $34.9 \pm 6.2 \times 10^{-15}$ $33.7 \pm 6.2 \times 10^{-15}$ $35.7 \pm 6.3 \times 10^{-15}$
	2			0.2673 0.2673 0.2673 0.2673 0.2673	$0.6667 \times 10^{-6}$ $0.6154 \times 10^{-6}$ $0.5000 \times 10^{-6}$ $0.5714 \times 10^{-6}$ $0.5714 \times 10^{-6}$	$58.1 \pm 7.1 \times 10^{-15}$ $53.6 \pm 6.9 \times 10^{-15}$ $43.6 \pm 6.4 \times 10^{-15}$ $49.8 \pm 6.7 \times 10^{-15}$ $49.8 \pm 6.7 \times 10^{-15}$
2	1	10	$8.763 \times 10^{-7}$	0.1863 0.1863 0.1863 0.1736 0.1704	$0.5474 \times 10^{-6}$ $0.5128 \times 10^{-6}$ $0.4762 \times 10^{-6}$ $0.4301 \times 10^{-6}$ $0.3960 \times 10^{-6}$	$72.8 \pm 12 \times 10^{-15}$ $68.2 \pm 11 \times 10^{-15}$ $63.3 \pm 11 \times 10^{-15}$ $61.4 \pm 12 \times 10^{-15}$ $57.5 \pm 12 \times 10^{-15}$
	2			0.1768 0.1768 0.1895 0.1927 0.2022	$0.5263 \times 10^{-6}$ $0.5000 \times 10^{-6}$ $0.5000 \times 10^{-6}$ $0.4878 \times 10^{-6}$ $0.5000 \times 10^{-6}$	$73.7 \pm 12 \times 10^{-15}$ $70.1 \pm 12 \times 10^{-15}$ $65.4 \pm 11 \times 10^{-15}$ $62.7 \pm 11 \times 10^{-15}$ $61.3 \pm 10 \times 10^{-15}$
Reading Error				$\pm 0.01112 \text{ m}$	$\pm 0.0500 \times 10^{-6} \text{ m}^3/sec$	Calculated from values at left

**Notes:**

1. Direct measurements were at most to three digits accuracy, but more are shown as a result of units conversion or derived value; (i.e. Head drop was measured in inches of water and flow rate from a cylinder graduated in cubic centimeters).
2. Temperature measurements were not made frequently. The temperatures tended to be low because of evaporation under a ventilated hood. The difference between 16 degrees C and 10 degrees C would represent about  $6 \times 10^{-15} \text{ m}^3$  for the highest value of  $Ks$  shown.



calculated values of permeability in section 5.1.1.2. Of course, this may also represent a flaw in the empirical model used there. For example, that model is based upon the meshing of 'normal', uncalendered screens. With calendered ones there may be less tortuosity of the flow path and less reduction of flow resistance.

An interesting comparison of the results can be made with those of Adkins (Ref. 20). Using the earlier calculated values of permeability ( $1.333 \times 10^{-10} \text{m}^2$  for Assembly 1 and  $1.064 \times 10^{-10} \text{m}^2$  for Assembly 2) and the corresponding values of thickness for the 100 mesh wicks (1.092mm or 0.043" and 1.041mm or 0.041") gives  $\kappa_w \delta_w$  of  $146 \times 10^{-15} \text{m}^3$  and  $111 \times 10^{-15} \text{m}^3$  respectively. Comparing these with the measured data, the value of  $\kappa_w \delta_w$  apparently has been reduced by a factor of 2.5 to 4.3 for Assembly 1 and 1.5 to 1.9 for Assembly 2. Adkins's results showed a reduction of this quantity by a factor of 10 in his screen hydroformed without wax impregnation.

### 5.2.2 Electroformed Wick

It had originally been intended to manufacture a dome with the electroformed wick described earlier for installation into one end of the heat pipe test cylinder. The contractor for this work was Electroformed Nickel, Inc. (ENI) of Corona, CA. They encountered significant problems in fabricating the wick. As in the case with the screen wick fabrication, they should have been visited at the beginning of the process. The failure to do so reduced our chances of success with this inherently more challenging process. Eventually, considering the situation, historical difficulties with the technology, and rapidly escalating time and budget estimates, the electroformed wick was abandoned.

The first step of the nickel deposition process was to produce a photographic master pattern for the diamond shaped 'posts' that would cover the entire plate. The basic pattern in rectangular coordinates was reproduced in twelve sectors to complete a full circle, Figure 5.11. This approximation reduced the complexity of developing the master; the vendor did not have to add a correction factor between each post to account for the curvature around the entire circle. Nonetheless, more than one try was required to obtain the desired pattern with the fully nested diamond geometry.

Next, two Inconel 617 plates were sent with the master from ENI to their subcontractor for deposition of a 'resist pattern'. Upon receiving back the plate, ENI proceeded with nickel deposition. Two defects in succession became apparent. First, there had been an excess of Ni deposited. This resulted in 'spillover' of the metal above the top of each diamond and onto the resist pattern. As a result, the diamonds took on a rounded appearance. Second, when ENI attempted to grind off this excess, the pattern ripped off of the Inconel. They found that they were easily able to remove the pattern from the other plate using a chisel. Clearly, adhesion was inadequate.

ENI and Sanders personnel then considered plans to recover from these difficulties. For the excess deposition the solution discussed was to increase the resist pattern height in the channels from 10 to 12 mils to avoid spillover. ENI prepared anode shields to improve the evenness of the deposited layer over the plate by avoiding local current concentrations in the deposition bath.

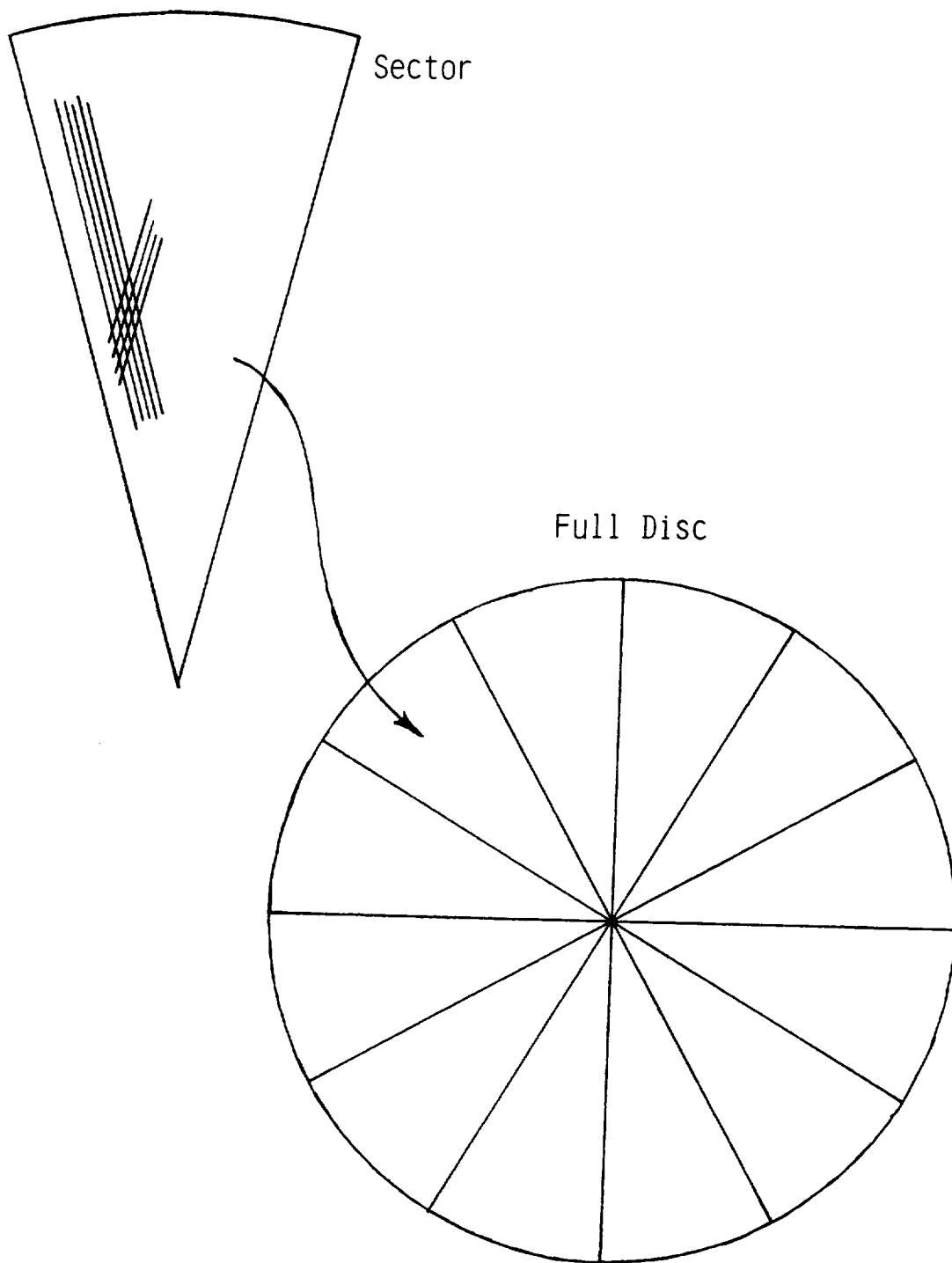


Figure 5.11 Repeated Electroform Pattern

The problem of pattern adhesion was more complex. They discussed their recommendations in a detailed letter, included as Appendix A; the essentials are summarized here.

The starting Inconel 617 had first been subjected to anodic removal of a thin layer so that subsequent electrodeposition would not be distorted by the cold worked grain structure of the metal. After this treatment the alloy has a matte appearance and an oxide layer. These oxides were removed in a 'cathodic acid activation treatment' (hydrogen scrub) to reduce the surface to pure active (bare) metal suitable for deposition of the Ni diamond pattern. The sulfides from this treatment could not be permitted to be carried over to the electrodeposition bath, and thus a brief water rinse had to be performed. Though brief, the rinse could have permitted oxides to form again on the surface, thus reducing the effectiveness of bonding of the diamond pattern. (They were also concerned that the cathodic treatment might have caused damage to the photo resist pattern.)

They suggested two alternatives to alleviating the problem. One would have resulted in an identical procedure except for using a sulfamic acid rinse instead of a water rinse. In the other, the Inconel would have been coated with a 0.5 mil layer of pure Ni prior to the application of the photo resist. This would have allowed the metal to be treated as pure Ni for the oxide removal and electrodeposition steps. Since nickel forms a simpler and much weaker oxide layer than Inconel (indeed, the Inconel is formulated to have a strong protective oxide), the whole process would have been simplified.

Although it would have been technically interesting to investigate these solutions it was clear that a morass of time and cost escalation might have resulted.

### 5.3 "Heat Pipe" Cylinder

#### 5.3.1 Design and Construction

The purpose of the heat pipe cylinder was to provide a means of testing the evaporator domes at the lowest possible cost. This was done by incorporating design features that were felt to be essential while omitting those that were of lesser value or excessive refinement. Because of time and money constraints no fully detailed structural/thermal analysis was made of either the vessel alone or integrated with the evaporator domes.

Figure 5.12 depicts the completed cylinder with both end domes welded on. The tube itself was rolled and welded from 1/8" stainless 316L. This processing was performed by a local vendor, who had welded along the outside of the seam. Sanders technicians and technical staff were displeased with the unevenness and degree of oxidation of this weld. It was rewelded at Sanders on the inside of the seam, wire brushed to remove oxidation and helium leak checked.

Three filling tubes were welded into the cylinder as suggested by Horace Neely of ETEC. At the time a particular filling procedure was being discussed with them which would have required this number of tubes. Neely sent the tube material

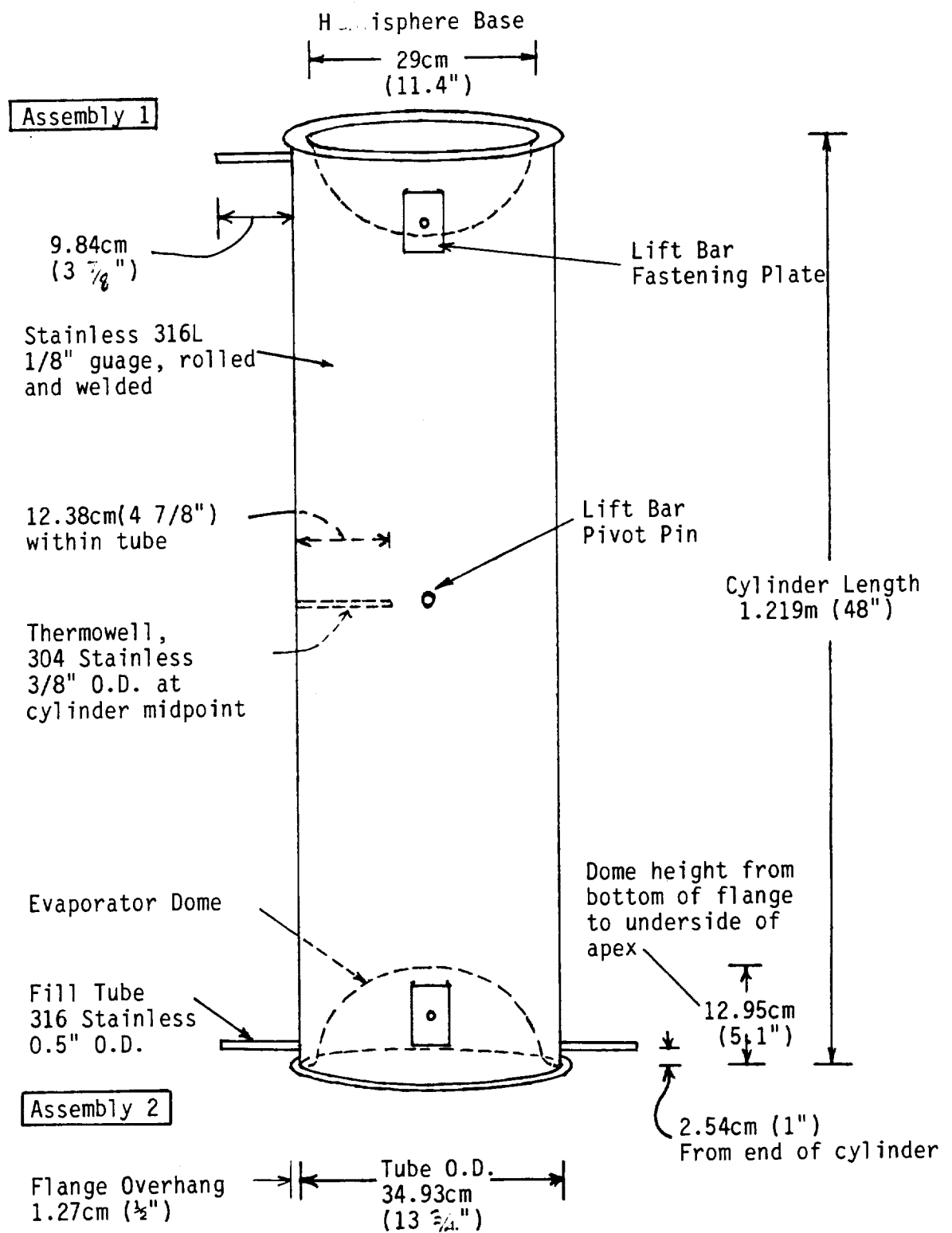


Figure 5.12 Heat Pipe for Evaporator Dome Test

(stainless 304L, 0.035" wall, 0.5" OD), which he stated was what they preferred for pinching and welding, although it was later discovered that they had little or no experience in doing this with a vacuum inside a container. To avoid a crevasse suitable for attack by sodium oxide, the suggestion of Don Ernst of Thermocore was followed by welding the tubes along the inside joint. Each of the tubes is centered one inch from the respective end of the cylinder. A visual mnemonic was adopted by placing Assembly 2 in the end with the two fill tubes 180° apart, and Assembly 1 in the other end with the single tube.

No pressing reason was seen for the use of thermowells within the cylinder chamber was seen; under nominal conditions, the heating of the cylinder can be monitored by thermocouples welded or strapped to the side. (Both ETEC and Thermocore maintained that it was likely that thermocouples attached to the cylinder before filling would detach during the various handling steps of that process. Neither of the personnel contacted at these companies thought that welding bare wire thermocouples to the cylinder after it was sodium filled would be a problem.) Nonetheless, under certain anomalous conditions - e.g. the development of a significant thermal gradient between the sodium vapor and the wall due to the presence of noncondensable gasses - it would be helpful to try to measure the vapor temperature. Thus, a single thermowell was installed at the halfway point of the cylinder (Stainless 304, 3/8" O.D. 0.050" wall, 4 7/8" length). Unfortunately, given the well's location, the Sanders welder found it impractical to weld at the inner joint, so there is a crevasse present there.

The photograph shown in Figure 5.13 details the construction at the inside surface of the cylinder end. In addition to the weld line of a fill tube and part of that of the cylinder several of the angle irons are shown. They are 316 stainless, cut back and rounded at the edges where they rest against the flat flange of the dome. Their visible welds to the cylinder were accessible for wire brush cleaning of oxides, but in the small gap between them and the cylinder wall that was not possible. Instead, a 1/8" hole was drilled through each to promote cleaning by liquid sodium flowing through the hole and the unwelded gaps visible in the photograph. In this cleaning process, oxygen entering the sodium has the potential of causing deleterious effects elsewhere in the system; without the circulation, there might be weld corrosion from the relatively stagnant sodium trapped in the gaps. (Ideally, the contaminated sodium would be drained before a final charge were released into the cylinder. The effect of the small amounts of oxide present here is likely to be negligible, though whether this would be true for many thousands of hours of operation is uncertain. See the section on sodium filling for amplification.)

The reason for adding the angle pieces to the cylinder can be understood with the aid of Figure 5.14 showing a cross-section through a radial slice of either dome near the cylinder wall. Each dome is welded to this wall at the outer edge. Since the cylinder is normally evacuated, there will be an atmosphere of pressure pushing the dome into it. (Actually, at the nominal operating point of 1035K, the sodium vapor pressure of about 0.35atm partly counteracts this, but the vapor pressure becomes negligible with a drop of only 150 K.) Without the angle piece, this pressure would cause the flange to pivot around the inner edge of the cylinder wall, inducing tensile stress in the weld. Given the budget for completing the cylinder, it was not possible to perform a complete analysis of this joint stress, but an estimate by the Sanders mechanical analysis section indicated that conditions were close to In617 yield stress of about 39ksi. This did not include consideration of differential thermal expansion between

ORIGINAL PAGE  
BLACK AND WHITE PHOTOGRAPH

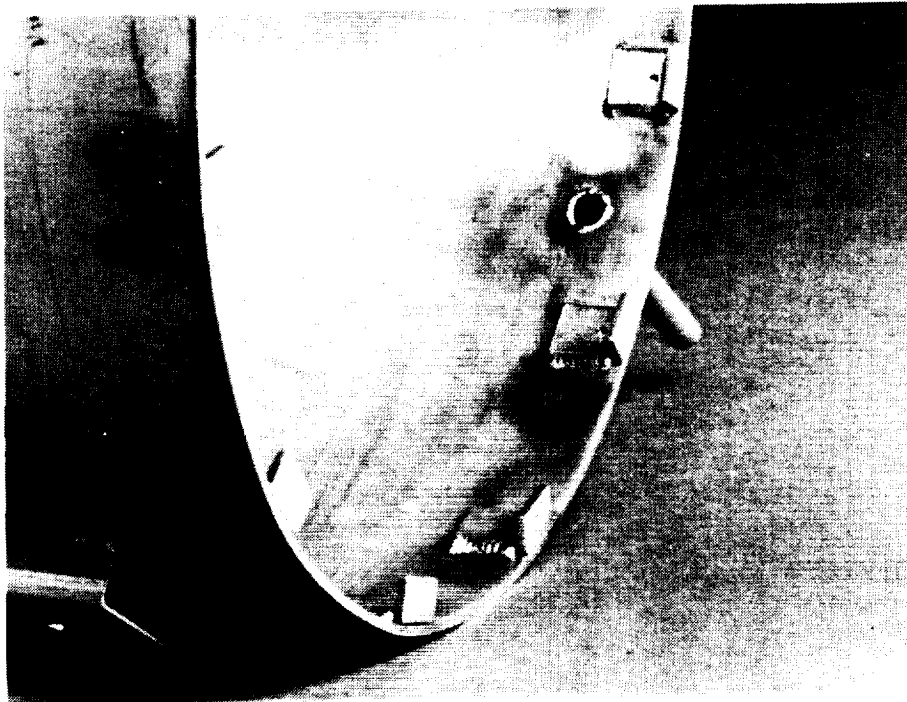


Figure 5.13 Detail of Heat Pipe Cylinder End

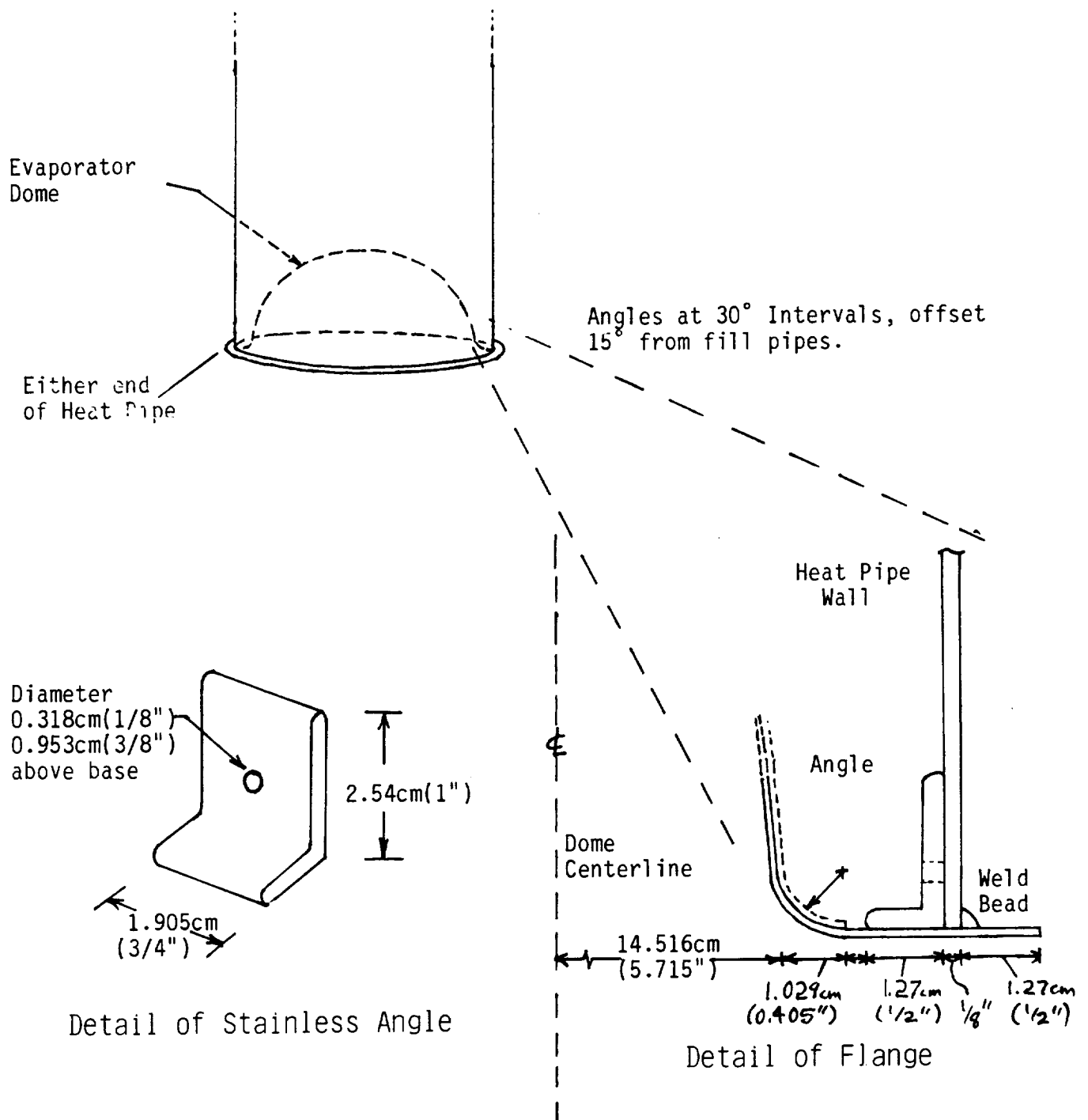


Figure 5.14 Details of Dome Flange in Heat Pipe

the Inconel and the stainless. Using the INCO data book and Touloukian's data on 300 series stainless, the difference should be about 0.4% at 10500K - approximately 0.159cm (1/16") over the dome's diameter (Ref 21). The function of the angle pieces was to reduce the strain on the outer weld; they rest against the dome flanges without any mechanical or welded attachment there.

The cylinder was again helium leak checked after the thermowell, fill tubes and angles were welded into place. What sort of surface cleaning is needed before sodium filling apparently depends who does the filling. ETEC had suggested an acetone cleaning followed by an argon backfill, but Thermocore was relatively unconcerned with the as-received surface condition, indicating that their processing would compensate. For reference, the final surface exposures of the heat pipe components are summarized in Table 5.5. The permeability test left a circular stain at the top of Assembly 1 but not on Assembly 2. This stain occurred where a foam rubber seal had been applied to the screen and did not come off during the following solvent washings. Retrospectively, it appears that the difference between treatment of two assemblies was that number one was exposed to isopropanol during our early attempts to get the permeability test to work; this may then have degraded the seal sufficiently to cause the stain. While it seems unlikely that this residue would cause permanent harm, a rinse with isopropanol should be used to remove it.

### 5.3.2 Estimation of Heat Pipe Sodium Fill Requirements

Several factors must be kept in mind when determining the quantity of Na to be used in the heat pipe test rig. The basic requirements are that there be adequate sodium to saturate the two wicked domes, fill the void space as vapor, and form a condensate film running continuously down the walls.

The void space vapor is the smallest of these contributors. Using the perfect gas law at 1040 K and 0.4 atm vapor pressure of Na gives a requirement of 12.1 gm (equivalent to about 16 cm<sup>3</sup> when condensed at that temperature).

The wire fractional volume can be used to find the liquid volume needed for a saturated screen. We start here with the wire volume per unit area,  $V_L$ , for a given layer of screen and assume that the layer thickness is small compared to the dome radius. Then we have

$$V_L = 2 \frac{A_w f}{S_c}$$

where  $A_w$  is the cross-sectional area of an individual wire and  $S_c$  the spacing between wires (i.e., the inverse of the number of wires per unit length). The quantity  $f$  accounts approximately for the bending of wires due to interweaving, and may be expressed as

$$f = \frac{1}{\cos \theta}$$

where

$$\theta = \tan^{-1} \frac{d}{S_c}$$



Table 5.5 Surface Exposure and Cleaning Steps of Heat Pipe Components

Evaporator Domes

Assembly 1		Assembly 2	Cylinder
Final Vacuum Anneal, Ar flush	Final Vacuum Anneal, Ar flush	Exposed to methanol in permeability test.	Degreased in Trichlorethane, wiped down in Acetone. Some hand contamination near ends during final assembly, He leak check using diffusion pump line at 10 <sup>-6</sup> torr after overnight pump down.
Exposed to Isopropanol and methanol in permeability test			
Degreased in Trichlorethane.	Degreased in Trichlorethane.		Back filled with Ar (weld quality).
Washed in methanol, then acetone, dried with air hose* and heat gun.	Washed in methanol, then acetone, dried with air hose* and heat gun.		
Overnight pumpdown for He leak check (see right).			

\* Note: Air hose was not oil trapped.

Here  $d$  is the individual wire diameter (see Figure 5.15). Essentially, the formula for  $V_L$  treats each set of parallel wires in a layer as a unit, and accounts for the whole layer by the factor of two.

Table 5.6 shows data for the wires used in the stacked screens. Dividing the wire volume per unit area by the total volume per unit area (i.e. the thickness) gives the fractional wire volume,  $(1 - \epsilon)$  and thus the screen porosity  $\epsilon$ . The calendering effect is approximated by assuming that as the wires are crushed, they will just fill in the empty volume of the screen (rather than increasing the overall screen area) until the wire volume fraction is 100%. Thus, the wire fraction will increase by  $1/0.75$  for a 25% calendered screen.

The empty volume of a stacked screen is given by

$$V_s = \left[ \sum_n \epsilon_n t_n \right] A_s$$

where the summation is over the layers and the area of the screen  $A_s$  is here the area of the hemisphere plus the small lip at the edge, about 230 in<sup>2</sup>. Assuming a full hemisphere, (of 11.4" diameter) and no screen collapse, gives a little more sodium volume than actually needed. Recalling the stacking components

Assembly 1: 4 uncalendered 100 mesh  
               1 calendered 100 mesh  
               2 uncalendered 400 mesh

Assembly 2: 3 uncalendered 100 mesh  
               2 uncalendered 100 mesh  
               3 uncalendered 400 mesh,

the results are void volumes of 6.465 in<sup>3</sup> (106 cm<sup>3</sup>) and 6.290 in<sup>3</sup> (103 cm<sup>3</sup>) for Assemblies 1 and 2 respectively. It is assumed that both wick assemblies remain saturated with sodium though only one is being used as an evaporator at any one time.

The third primary component of sodium in the tube is the wall condensate, which is assumed to be a continuous film layer. The simplest analysis presented by Rohsenow is that illustrated in Figure 5.16 (Ref 22). (A more elaborate analysis includes an interface resistance between gas and vapor, but while this effect can be significant for liquid metals, it is only so at low pressures. Rohsenow also gave verbal assurance of the reasonableness of the simple approximation in this case to the present author.) Liquid condenses uniformly along a vertical plate with an increasing thickness with vertical drop. Given a laminar flow, the temperature distribution will be nearly linear, and is assumed so. For narrow, tubular condensation area there might be rapid gas flow and consequent shear stress along the liquid-vapor interface; with the large diameter tube used here the effect can be neglected. Ignoring momentum changes, Rohsenow derives the expression for film thickness

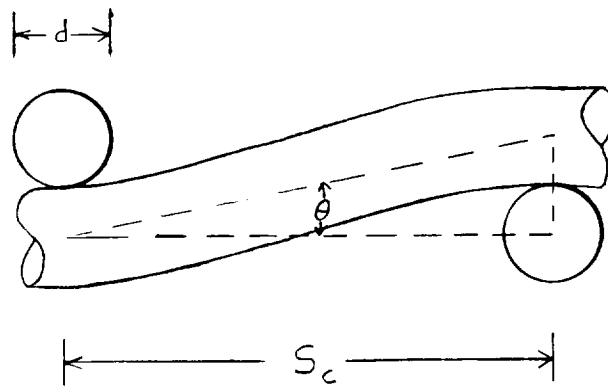


Figure 5.15 Parameters for Screen Evaluation

Table 5.6 Geometric Characteristics of Wire Screens

Mesh Type		d		S <sub>c</sub>		θ (degrees)	f	A <sub>w</sub>		V <sub>L</sub>			Void Fraction
Wires /cm	Wires /in	cm	in	cm	in			cm <sup>2</sup>	in <sup>2</sup>	cm <sup>3</sup> /cm <sup>2</sup>	in <sup>3</sup> /in <sup>2</sup>		
39.37	100	0.01143	0.0045	0.0254	0.01	24.23	1.097	1.026x10 <sup>-4</sup>	1.590x10 <sup>-5</sup>	8.862x10 <sup>-3</sup>	3.489x10 <sup>-3</sup>		61.23
39.37 (calendered)	100												48.31
157.48	400	0.00254	0.001	0.00635	0.0025	21.80	1.077	5.067x10 <sup>-6</sup>	7.854x10 <sup>-7</sup>	1.719x10 <sup>-3</sup>	6.767x10 <sup>-4</sup>		66.17

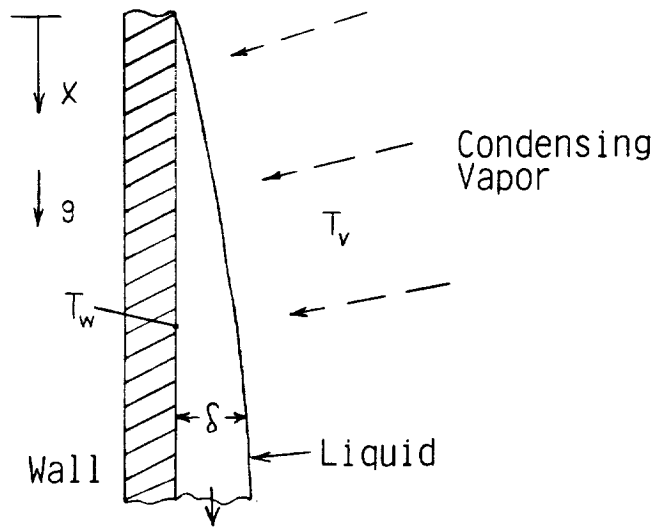


Figure 5.16 Condensation on Wall[Ref.22]

$$\delta = \left( \frac{4k_l \mu z (T_v - T_l)}{g \rho_l (\rho_l - \rho_v) h_{fg}} \right)^{\frac{1}{4}}$$

with  $\delta$  a function of distance "z" down the wall. The liquid thermal conductivity, dynamic viscosity, density and heat of vaporization are  $k_l$ ,  $\mu$ ,  $\rho_l$  and  $h_{fg}$  respectively, while  $\rho_v$  is vapor density (small compared to that of the gas) and  $g$  is just the gravitational constant. For the present case ignore  $\rho_v$  and express the temperature drop across the film,  $T_v - T_l$  (where  $T_l = T_w$  here), in terms of the flux ( $W/m^2$ ) radiated from the outside of the tube,  $q$ , i.e.

$$(T_v - T_w) = q \frac{\delta}{k}$$

and

$$\delta = \left( \frac{4\mu q z}{g \rho_l^2 h_{fg}} \delta \right)^{\frac{1}{4}}$$

or

$$\delta = \left( \frac{4\mu q}{g \rho_l^2 h_{fg}} \right)^{\frac{1}{3}} z^{1/3}$$

since the effective thermal resistance across the sodium and wall will be small compared to that by radiation to the outside world,  $q$  is set at a desired average value determined by the maximum heat loss required from the cylinder (i.e. we assume a cylinder of uniform temperature). For the cylinder as designed, with a stainless steel emissivity,  $\epsilon$ , of 0.7 after some high temperature exposure to air, the result is

$$q = \sigma \epsilon (T_w^4 - T_{bk}^4) = 4.611 \times 10^4 \text{ W/m}^2$$

where the wall ( $T_w$ ) and background ( $T_{bk}$ ) temperatures are 10400K and 3000K respectively and  $\sigma$  is the Stefan-Boltzman constant. (With surface area of about  $1.3m^2$  this gives 60 Kw dumped by radiation alone). Using values of the constants (Ref 11) of viscosity  $1.79 \times 10^{-4} \text{ kg/m-sec}$ , liquid density  $757 \text{ kg/m}^3$  and heat of vaporization  $3.975 \times 10^6 \text{ J/kg}$  one obtains

$$\delta \cong (1.14 \times 10^{-4} z)^{1/3} \text{ (in meters)}$$

which gives  $d=0.122 \text{ mm}$  at the bottom of the 48 inch tall tube. To be conservative, this thickness is applied over the entire height, resulting in a requirement for  $160 \text{ cm}^3$  of sodium at 1040K.

The total sodium volume requirement is now  $385 \text{ cm}^3$ . Increasing the peak flux to result in 80Kw total power output (at 1118K with  $\epsilon = 0.7$ ) increases the value of  $d$  by about  $(4/3)^{1/3}$  or 1.1 to  $d = 0.134 \text{ mm}$ . Then the condensate sodium value goes to  $176 \text{ cm}^3$  and the total volume to about  $400 \text{ cm}^3$ . In addition, one should add to this the maximum quantity of sodium that might become trapped due to condensation in the stubs of the fill tubes. Assuming that the three originally 4" long  $1/2"$  OD tubes are pinched off at half that length, they add another  $20 \text{ cm}^3$  volume.

To avoid the complication of liquid sodium plumbing and handling systems during

the dome test, the plan was to have the heat pipe filled and sealed before being returned to our facility. Since the fill quantity is determined by the maximum liquid condensation layer, as well as other margins, there will always be some sodium remaining in an annular pool around the base of the dome. An excessive heat flux entering the dome could result in pool boiling, a phenomenon which is both difficult to model and a detriment to evaluating the performance of the evaporator dome alone.

Our objective was to reduce the heat flux to the pool so as to reduce the chance of boiling. Rich Diver of Sandia has noted (personal communication) that even a depth of 1-2 inches of sodium should not be a problem if the net incoming flux to the pool can be kept at about 10 w/cm<sup>2</sup> or less.

For the practical purpose of the testing, it had been intended to use a configuration like that shown in Figure 5.17, where an annulus of fibrous insulation protects the pool from direct impingement of furnace radiation. The depth shown - under one inch (and equivalent to about 210 cm<sup>3</sup>) - is the maximum expected if the screen domes are assumed to be always saturated with sodium. Note as well that there would actually be some loss of energy from the flange of the dome into the copper cooling plate.

### 5.3.3 Fill Technique Issues

#### 5.3.3.1 General Considerations

One of the most difficult questions to be considered in this program has been the selection of a technique for loading sodium into the test cylinder. The interaction of sodium with various species and metals is far from being well understood. One may find oneself weighing a variety of opinions largely dependent on the empirical experience of their authors in not necessarily analogous situations. The present writer attempts to extract the important issues in the context of the methods suggested by several vendors.

First, some general remarks on sodium properties. Due to its high reactivity, the free state of the element is not found in nature (Ref.23). The same reference notes that although sodium generally wets well on many solids, it does not easily wet stainless or carbon steels. To achieve good wetting of container walls and evaporator screens, Adkins (Sandia Laboratories) has followed a rule of allowing molten sodium to soak into the screen for at least a day before attempting to operate the system. (This was after baking off adsorbed water and volatiles for 48 hours at 540°C with a pumping station at 10<sup>-7</sup> torr.)

There is not necessarily a direct connection between this wetting and the stripping of chromium oxide from the metal, although such stripping should eventually occur (Jack DeVan at ORNL). Oxygen from this or other oxides (such as those produced as weld residues) or from other surface contaminants then goes into solution. Where concentrations are high-- such as at weld crevasses-- rapid metal corrosion may occur. If the concentration is high enough, corrosive sodium oxides may precipitate. (Among the a priori assumptions for the preparation of the heat pipe to be filled is that moisture is effectively removed. Water will react very rapidly with sodium to produce sodium hydroxide and hydrogen.)

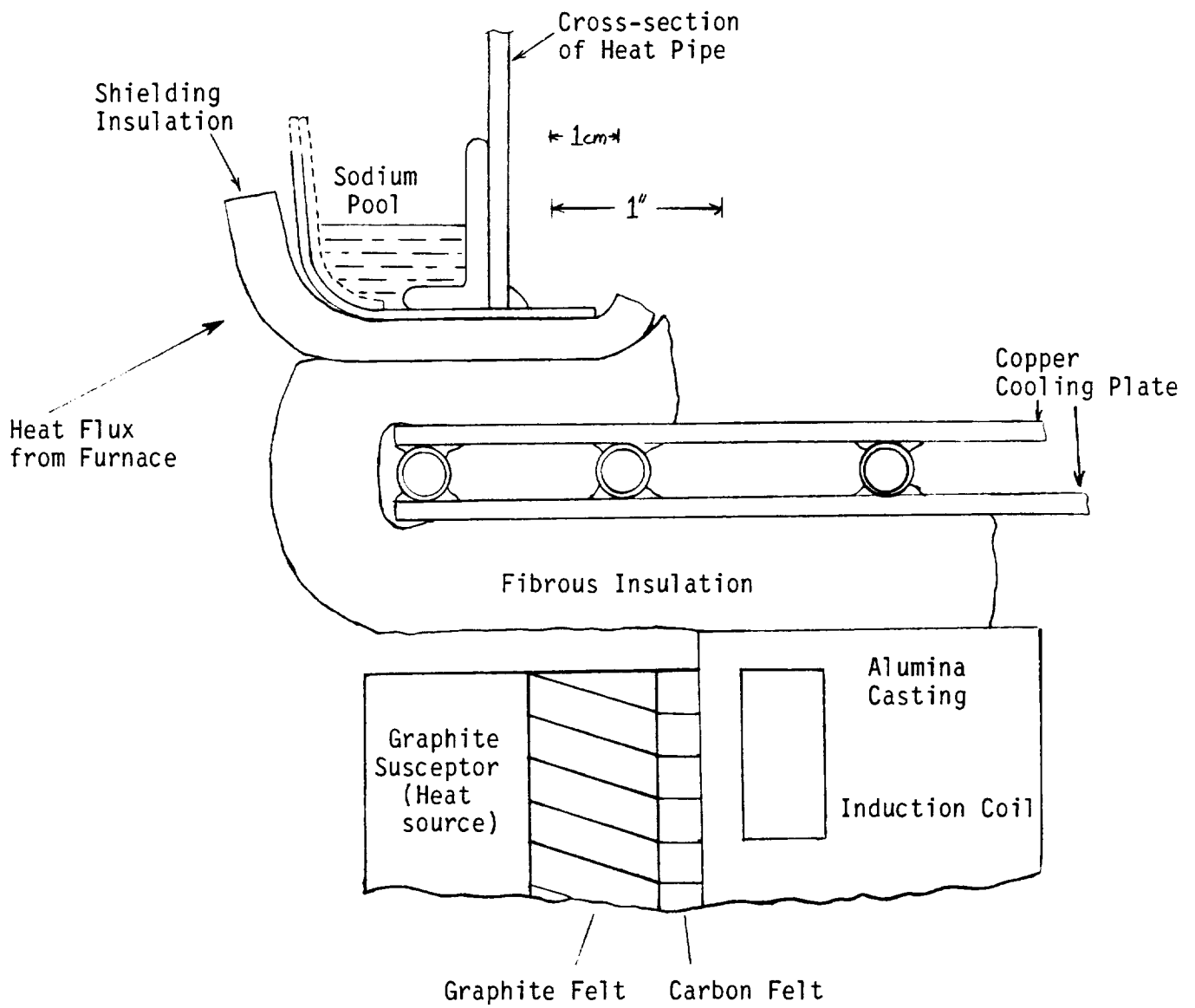


Figure 5.17 Protection of Pool Annulus by Insulation  
(Radial cross-section of furnace and heatpipe)



Another important consideration is useful to note at this point. Although a heat pipe and a liquid cooling loop may both employ sodium, the required flow rate in a heat pipe is very much less. This is simply because of the much greater amount of heat absorbed per unit mass by evaporating sodium than by typical temperature rises of the liquid (e.g., a temperature rise of 1000°K absorbs an energy per kg sodium of a little over 1/4 that required to vaporize the same quantity, Ref. 112). Thus, corrosive processes which depend upon high sodium transport rates -- such as Ni solution in the liquid in hot regions and redeposition in colder ones -- will be much alleviated in the heat pipe.

In liquid loops this transport can cause clogging of pipes within minutes. (ETEC has had considerably more experience with such loops than with heat pipes.) DeVan has not seen this effect in heat pipes (he also notes in passing that the solubility of metals in the sodium is not affected by oxygen concentrations).

The issue of the maximum permissible oxygen contamination level in the sodium is one of some controversy. DeVan suggests that the level should be "well below" 100ppm to prevent localized corrosion of the evaporator screen (This is the purity level of the sodium after chemically equilibrating with the container). Such attack can occur within a matter of hours due to the tendency for oxygen in the system to build up at the evaporator surface. On the other hand, Thermocore claims successful operation of heat pipes at contamination levels of the order of 100ppm for tens of thousands of hours.

Although there is no clear-cut explanation for this seeming contradiction, consider the following as a possible rationale:

For a given overall level of starting surface contamination, it may be that a critical figure of merit for gauging the likelihood of evaporator corrosion will be the relative total internal area of the evaporator vs. that of the container as a whole (here we define 'total internal area' for an evaporator to be the sum of the areas of all the wires internal to the screen). This quantity affects how 'concentrated' the surface contaminants become at the evaporator, since that component is the gateway through which all sodium in the system must pass.

In the case at hand -- the barewalled test cylinder with screened evaporators -- this figure of merit should be relatively high when compared to a heat pipe of similar overall dimensions, since the latter would have walls covered with screen. Thus one would anticipate that the test cylinder's evaporator would be less sensitive to contamination than the similarly dimensioned heat pipe. Moreover, the operating time of the cylinder will be relatively short. Given these observations, there is probably a reasonably high likelihood of tolerating the oxygen contamination levels claimed by Thermocore for the testing of the evaporator. However, for long-term operation, and particularly for the complete heat pipe receiver, the present author believes it prudent to call for oxygen levels that meet the 'well below 100ppm' criterion.

Before turning to details of candidate preparation and fill procedures, another consideration should be mentioned. The extremely high heat transport capability of the heat pipe, which is the characteristic making it a very close to an isothermal object, is dependent upon the free condensation of vapor upon 'cold' surfaces. The presence of a noncondensable gas in the chamber will create large thermal gradients.

An example of such a gas might be argon, which is typically used to push sodium through sodium flow systems. Argon could also be entrained in a frozen sodium 'bomb' (used to add a precise quantity of the liquid metal to the container) which originated in a sodium flow system. Thermocore has developed noncondensable gas removal as an essential part of its heat pipe filling technique.

As discussed by Rohsenow (Ref.22, pp.11-25 to 11-29), even when present in small amounts, the noncondensable gas will build up to a locally high density at the wall and cause the condensation to become diffusion-limited. (He gives the example of air contaminating steam to 5-10% by mass and resulting in a reduction of the heat transfer coefficient by a factor of 5-10. However, we note that the temperature drop across the sodium condensing on our cylinder walls is only of the order of 0.1K to start with.)

### 5.3.3.2 Preparation for Filling

In discussions with ETEC, Thermocore, Sandia and ORNL, the following were discussed as possible processing steps before adding the required charge of liquid sodium:

#### --Hydrogen Reduction

This is a step that would be used to remove oxides from the surface of the container. Both ETEC and Thermocore mentioned this treatment as something that would be done only if large amounts of oxides were present; for example, ETEC cited the case of a metal that had been subjected to an air quench resulting in a completely blackened surface. DeVan noted that one would have to be very careful to remove the hydrogen from the system afterwards. Thermocore stated that they use a post-reduction vacuum firing to remove hydrogen dissolved in the metal and water produced in the reduction. With only small areas of weld oxides in our container (from the final weld of the domes on either end) hydrogen reduction is unnecessary.

#### --Vacuum Outgassing at Elevated Temperature

In this operation species (such as water) are desorbed from the surface by raising the temperature of the container to at least 500°C while maintaining a vacuum. ETEC had proposed doing this using a  $10^{-3}$  torr mechanically pumped vacuum line in the originally proposed 'Option 1'. (The actual pressure in the container will be somewhat higher over typical timespans due to the relatively small size of the exit holes.) ETEC offered to perform this operation for higher cost using a diffusion pumped line at  $10^{-5}$  torr, but DeVan suggested that this would not result in a significant difference in the results. He also believed that, based on past experience, vacuum outgassing would likely provide adequate treatment to the container prior to addition of sodium for our evaporator test purposes. (Implicitly he was also assuming that the sodium started with purity better than 100ppm oxygen.)

Thermocore's version of this involved baking out the entire container in a vacuum furnace at  $10^{-4}$ - $10^{-5}$  torr and at a temperature greater than the operating point of the heat pipe. As noted above, Sandia baked their containers at 540°C for 48 hours with a vacuum line at  $10^{-7}$  torr, then proceeded to sodium filling.

The present author believes that some version of vacuum outgassing is an essential

step.

#### --Sodium Flow or Rinse

This technique takes advantage of the high chemical activity of the sodium by using it as a cleaning agent. It would be very good at removing adsorbed impurities from the wick and oxide contaminants as well as improving wetting. Practical versions use one or more rinse steps. ETEC's 'Option 2' proposed a double rinse using their 'argon-pushed' sodium flow system followed by a purity analysis of the dumped sodium. They claimed that the starting sodium purity would be of the order of 1ppm oxygen. It is expected that sodium would remain in the evaporator wicks after the rinse, thus reducing the quantity of material needed in the filling. DeVan held that a vacuum outgassing followed by a sodium rinse and confirmation of low oxygen levels would provide good assurance of a long lifetime system.

#### 5.3.3.3 Filling and Sealing

Following one or more of the above treatments would be the sodium filling itself. Due to the small mass of sodium required compared with that of the cylinder, it is probably impractical to use a weight-change method of measurement. Sandia tried such a method but in the end resorted to using a known volume container from which to flow sodium into the test vessel. The latter technique was also proposed by ETEC.

Before sealing the container one should be certain that, as much as possible, it is free of any contaminants (such as noncondensable gasses) that might have accumulated during the entire preparation and filling process. The possibility of argon trapped in the sodium has already been mentioned; ETEC said that they used 'Airco high purity' gas, but the details need to be better defined. Another issue that arose with ETEC was the possibility of inadvertent recontamination of surfaces in moving the container between different facilities. To address these concerns, discussions had begun with ETEC concerning the possibility of performing another elevated temperature vacuum outgassing after filling. If this were performed at 600K it could result in evaporation of several grams of sodium into the pumping system over four hours; at 400K the rate would be thousands of times lower, but about 500K might be advisable in analog with the initial cleaning step noted above. Sandia has performed this step at 400K for a full day.

ETEC had discussed their method of measuring sodium purity. It involved precipitating out sodium oxides by cooling sodium that had flowed or been rinsed from the chamber, so it would require some form of the rinsing process.

After the initial degassing of the empty container, Thermocore would backfill it with argon, then taken it to the filling station. There, it would be evacuated and heated to 2000C+ to remove the gas and the sodium would be 'metered in.' (We did not get to the point of discussing how this would be done. Also, Thermocore emphasized that details of their process were proprietary.) Starting impurity of the sodium would be about 100ppm oxygen. The next part of the process would be to actually operate the cylinder as a heat pipe for several hours at at least the intended operating temperature, while continuing to pump out noncondensable gas. Evidently, they have a method of doing this without pumping out a lot of the sodium at the same time. (While this step would be performed at the operating temperature of the heat

pipe, it would be at lower than operating power since the tube would be insulated rather than radiating freely.) Again, they expected final oxygen levels to be about 100ppm. Their method for actually measuring this, however, would require welding a vanadium wire into the container. This wire would have to be cut out to perform the measurement and in the process the chamber would be exposed to air.

The final step in the entire process is sealing the container. Originally, ETEC had recommended -- and Sanders had purchased -- two high temperature Swagelok valves. However, after the test configuration was developed where the valves might remain at very close to the operating temperature of the heat pipe (i.e. within the insulation box, see following sections), ETEC became concerned that the valves would not be adequate. The alternative was to pinch off and weld the fill tubes while maintaining a vacuum. ETEC indicated that they would have to do an extra research program to learn how to do this, as their previous experience had only been with pinching off containers that retained argon pressurization. DeVan stated that considerable effort had been required to develop the vacuum pinchoff method used at ORNL. Thermocore regularly performs this type of sealing in their heat pipe manufacturing.

## 5.4 Furnace

### 5.4.1 Requirements

The purpose of developing a high temperature furnace was to provide a source of energy to simulate the solar flux required for operation of the cavity heatpipe. At full power, this amounts to about 40kW through a 28 cm diameter aperture, which is the same as 65 W/cm<sup>2</sup> at the aperture or 32.5 W/cm<sup>2</sup> over the actual dome surface (assuming a full hemisphere).

Desireable but not required features were: an ability to approximately double fluxes through the dome to simulate the actual peak of the solar distribution; a capability to be used in future endurance tests for several thousand hours during Phase II of the program.

The temperature requirement of about 2000 K for the furnace is demonstrated by Figure 5.18 as a function of source and dome emissivities. The latter will depend upon the oxidation state of Ni alloy, but a value of 0.7 is a reasonable possibility. As shown, the view factor of the heat source is also a strong influence.

### 5.4.2 Design Options

Major heat sources evaluated along with the original rough "turn-key" cost estimates are listed in Table 5.7. Based upon these considerations, silicon carbide resistance heaters and induction furnaces using graphite susceptors were the prime options. Although the former had an advantage in simplicity (e.g., no special atmosphere required) it had other significant problems such as short lifetime of the heater rods and marginal capability to reach our power requirements.

Thus, induction heating was chosen for the present application. ( In the end, the supplier chosen was not able to produce a 'turn-key' system, and the costs in Sanders's labor plus auxiliary equipment well exceeded the estimate.) Direct inductive heating

Require high temperature source to drive sufficient power into dome. Depends upon geometry due to view factors.

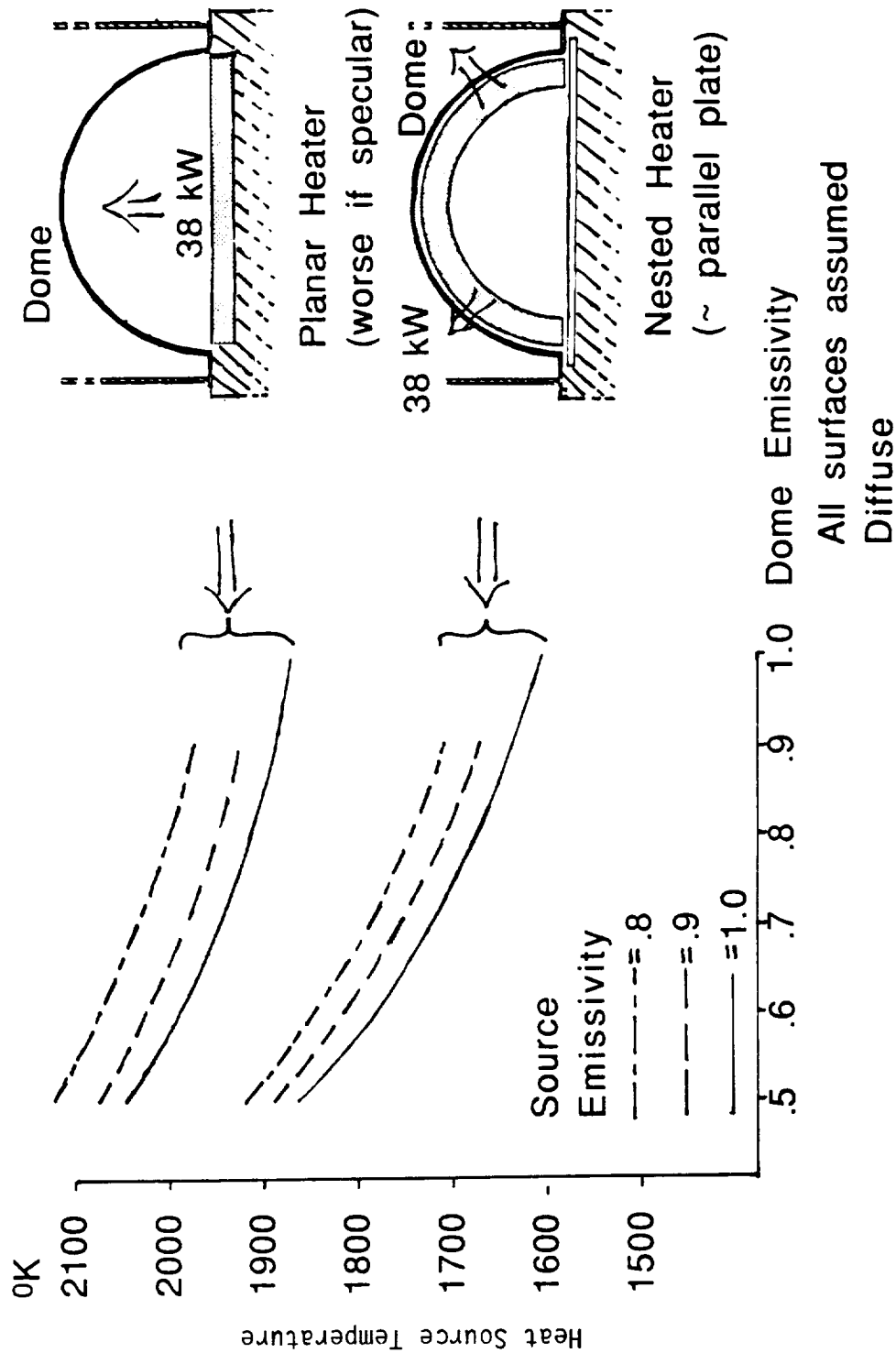


Figure 5.18 Heat Source Performance

Table 5.7 Major Options for Heat Sources

<u>Heat Concept</u>	<u>Attainable Flux On Hemisphere (<math>w/cm^2</math>)</u>	<u>Key Issues</u>	<u>Rough Cost</u>
Silicon Carbide resistance	28 to 34 use of cavity only	Marginal power capacity occasional rod replacement	\$13-18K
Refractory metal resistance (Ta,W,Mo)	uncertain	Required vacuum furnace for acceptable life. Thermacore proposes Argon purge.	\$14-100K
Graphite Resistance	33 or more	Argon atmosphere required but less stringent than refractory metals.	\$20-25K
Induction with Graphite Dome or cylinder susceptor	33 or more	Argon atmosphere	\$15-20K
Solar: GIT	40 avg, 60 peak	Downward cavity ideal but site no longer supported	\$100-150K
SNLA/TBC	>100	Tracking complicates procedures and presents a greater performance challenge	~\$30K

of the dome was rejected as it would have required a high frequency, high cost power supply. Figure 5.19 shows two versions of the indirect method using the common technique of heating a graphite susceptor. The method using graphite and induction coil "nested" within the dome incurs cost penalties in fabrication as well as having relatively low efficiency electrical coupling. With the cylindrical graphite susceptor we create a black-body cavity source, which with uniform wall temperature and an insulated lower end appears to the dome as thermally identical to the planar heat source shown in Figure 5.18

### 5.4.3 Selected Furnace Design

Figure 5.20 shows the furnace (at left) and adjacent electrical box ('work station') that provides 10 KHz to the induction coil. The steel framework uses electrical insulators at the holes to prevent a closed path that would allow induced currents. Power to the work station is supplied from a 100 kW capacity motor-generator running off of three phase 440 VAC. Two additional electrical boxes are used, one for providing starting current to the motor-generator, the other ('control station') for controlling power to the inductor.

Several thermocouples monitor the furnace and water line temperatures. (Instrumentation is discussed in the next section). Circulating water is provided to the upper and lower copper plates and to the induction coil. The coil is imbedded in the cast alumina ceramic forming the body of the furnace. To prevent rapid oxidation of the graphite susceptor, argon gas is first flushed through and then leaked in during operation.

The next illustration, Figure 5.21, is a cutaway view. The graphite susceptor is supported by a low density "Fiberform" graphite insulation block and centered within the casting by layers of graphite and carbon felt (purchased from Fiber Materials Inc., of Biddeford, Maine). Both were selected, after extensive consultations, on the basis of their excellent thermal insulation properties, ability to withstand as high a temperature as the inductor, compatibility with the inductor and significantly lower cost when compared with oxide fiber insulators.

The inductor itself is of Union Carbide CS type graphite. It must be placed within the casting so as to couple properly with the induction coils. Encur Inc. of Keyport NJ designed and adjusted the coils and the capacitors in the work station so as to provide near uniform heating of the inductor. They also supplied the work station, water generator, starter box and control station on a rental basis. Besides providing inductive power, the copper coils also absorb heat conducted out from the susceptor.

The upper and lower water cooled copper plates also absorb heat from the furnace; the upper one provides thermal insulation of the 1000K heat pipe from the 2000 K furnace. These plates can provide insulation of exterior metals from the inductive effects of the coil if they are allowed to form a closed loop electrical path so that they create an opposing field. However, in accord with Encur's concern about overheating of the plates, they were initially fabricated with a radial slit to prevent such a closed loop. Later, it proved useful to create a loop on the upper plate by closing this loop, thus reducing inductive heating above it (see later section).

Our original design called for the use of the graphite Fiberform insulation at the top of the furnace (Figure 5.22a). As a result of the qualification testing, this was

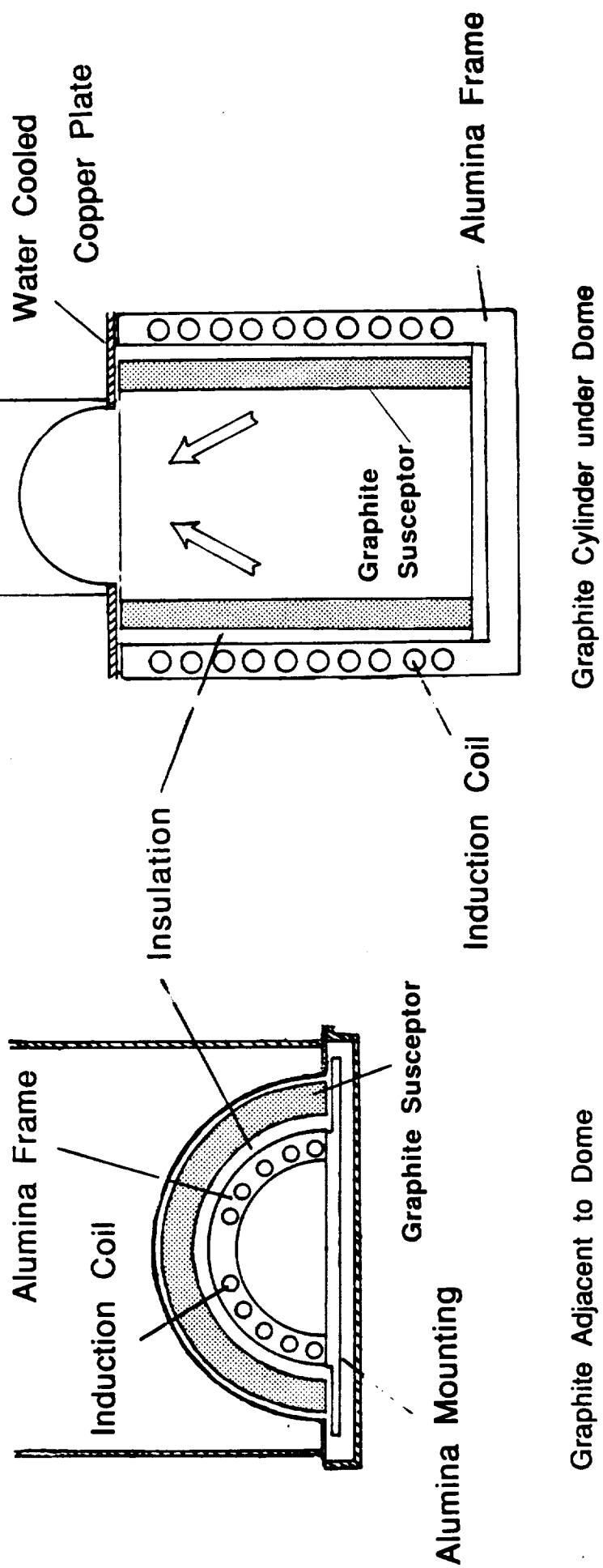


Figure 5.19 Induction Furnace Options



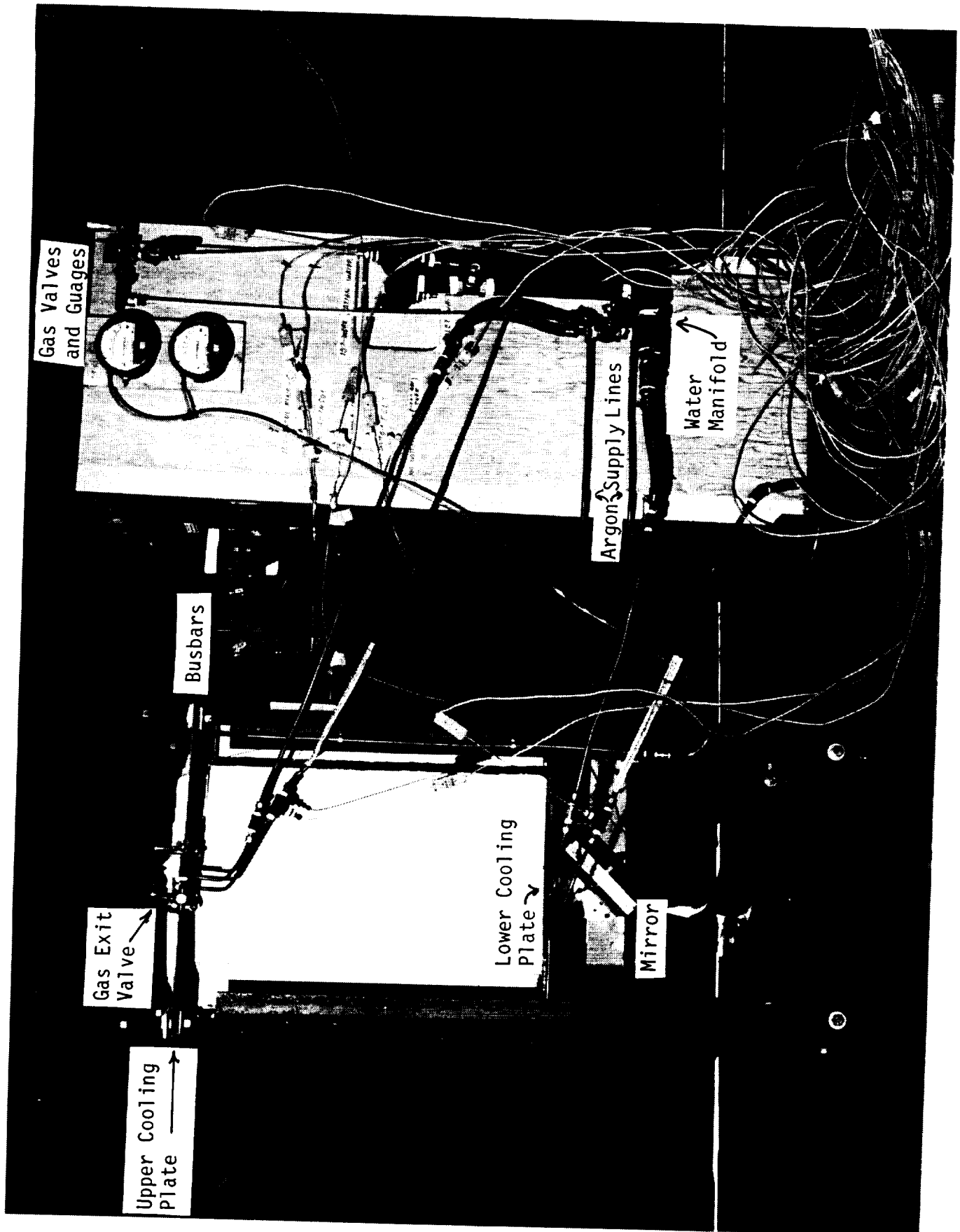


Figure 5.20 Furnace and Look Station in Frame

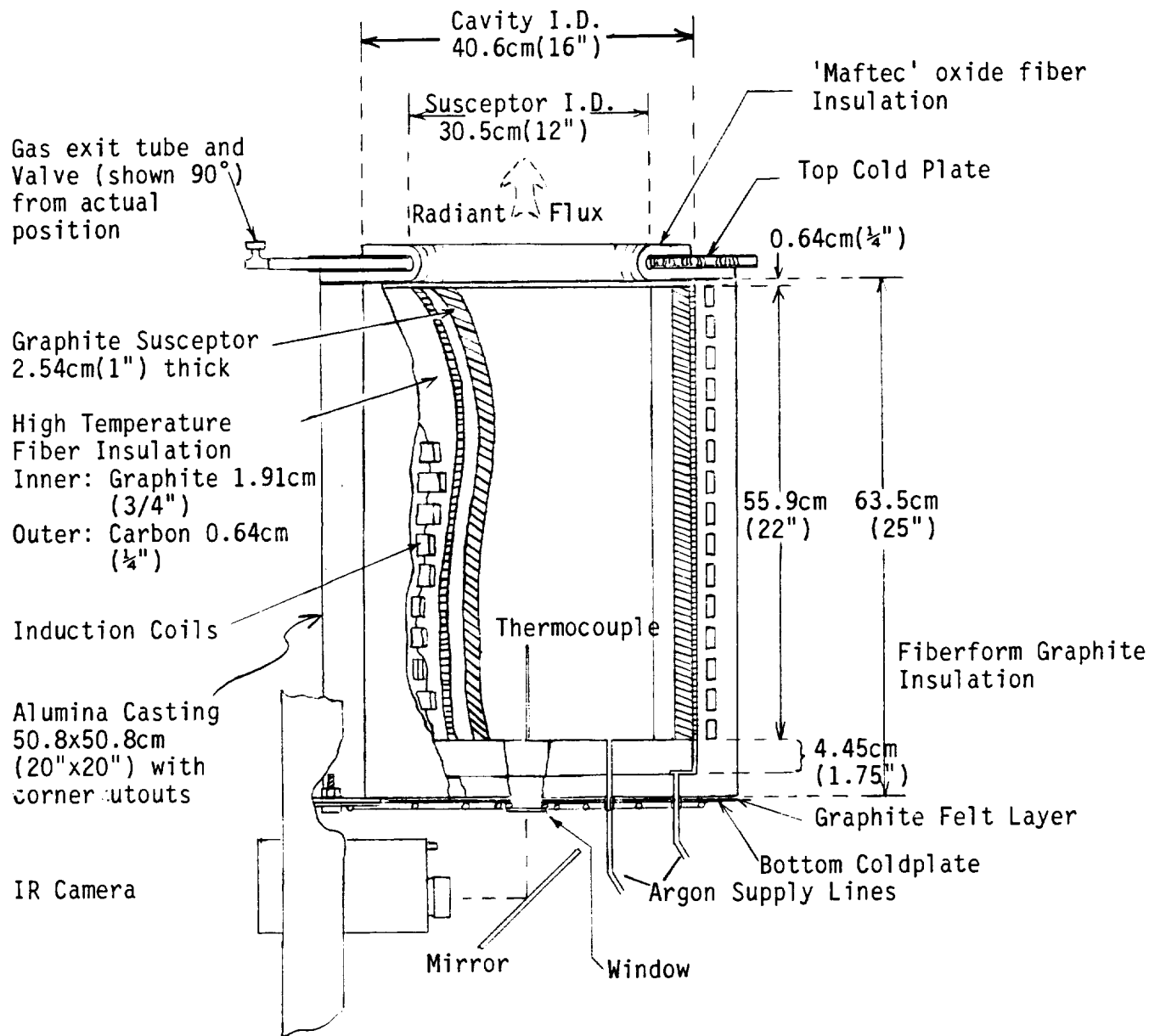
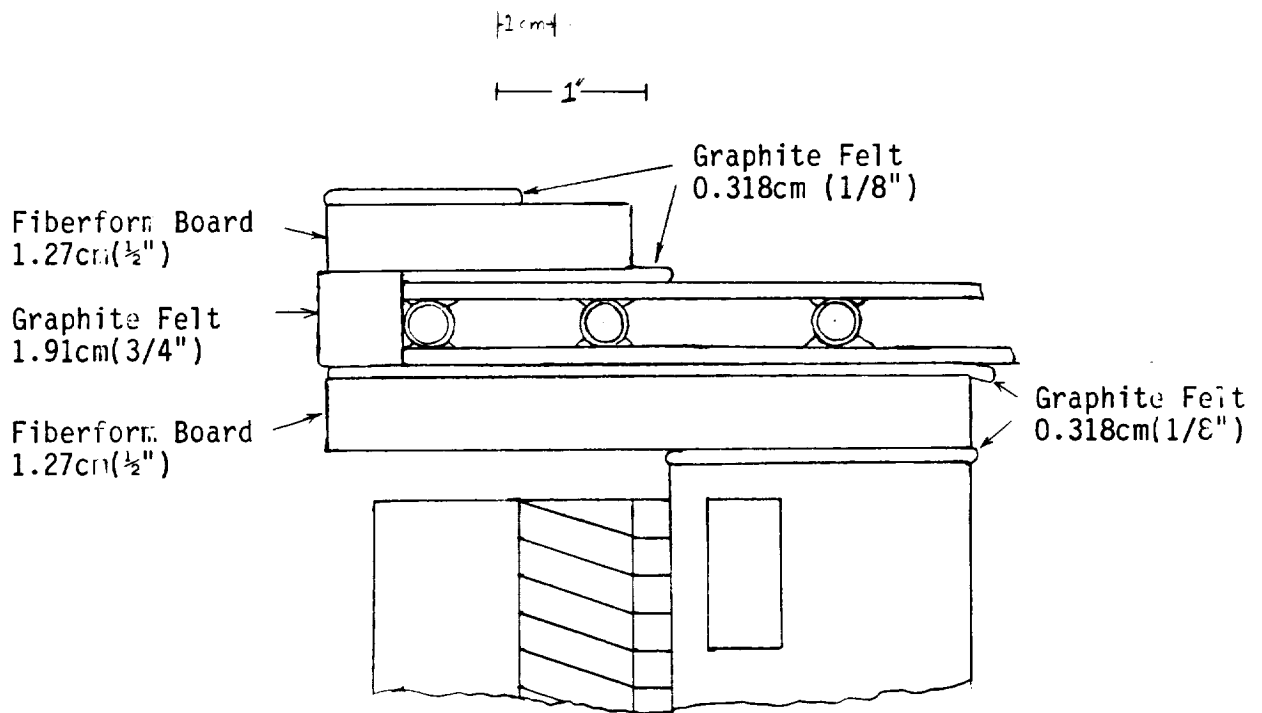
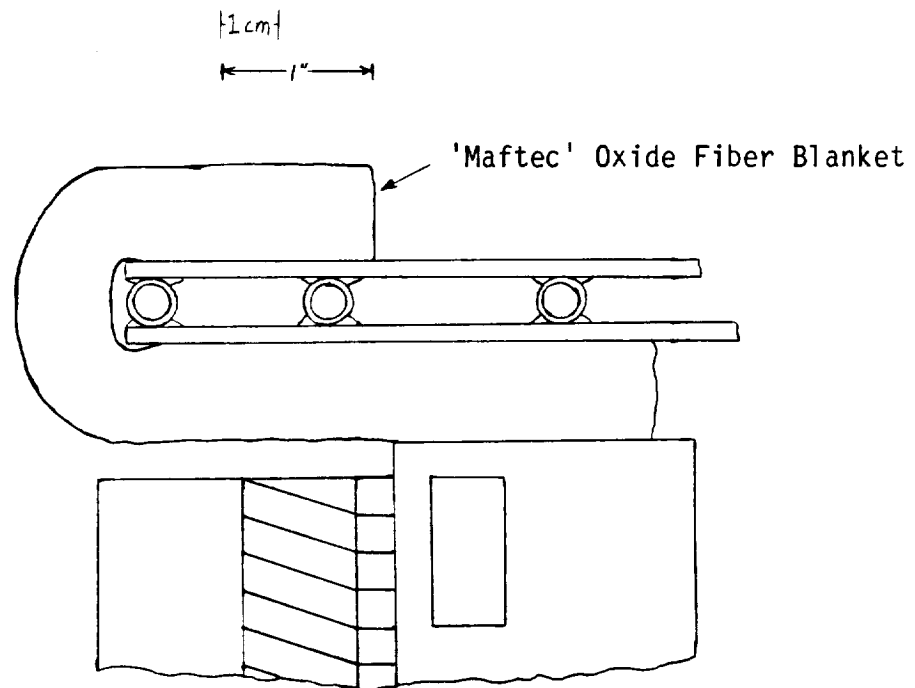


Figure 5.21 Cutaway View of Furnace



a. Original Design



b. Modified Design

Figure 5.22 Change in Furnace Insulation

changed to an oxide fiber blanket (Figure 5.22b). Eight sections of a Johns - Manville alumina blanket were cut to fit around the top hole, but later the mullite-based 'Maftec' fiber (produced by the same manufacturer), which has a higher melting point, was obtained. (Due to the reduction in scope of the program, neither substitute for the fiberform was tested.) Alumina blanket, when used as a cover over the top of the furnace, had hardened during our highest temperature tests.

Argon gas is conveyed to the furnace through fittings mounted in the lower copper plate. Each fitting transitions to a ceramic tube which then enters through holes drilled in the alumina casting. One tube enters the furnace within the inner radius of the susceptor, and gas then flows directly in through a hole in the Fiberform board insulation. Relatively little pressure is required to flush this center part of the furnace, but one also must prevent oxidation of the outer surface of the susceptor as well as the insulation packed around it. A separate line is provided which directs gas first through the alumina casting and then into channels carved in the underside of the Fiberform that lead to its edges at points spaced by 180°. There, the gas can escape into the approximately 3.2mm (1/8") gap between the outer edge of the fiberform disc and the alumina casting, and penetrate up into the fiber insulation surrounding the susceptor. One-eighth inch graphite felt is used to seal the copper plate to the somewhat uneven under surface of the alumina casting as well as a gap filler between the bottom of the fiberform disc and the alumina. Graphite felt or alumina blanket is used throughout the furnace to make it as gas tight as possible.

To allow a rapid argon flush of the furnace a valve on a ceramic tube is provided. This tube enters through the upper copper plate at the gap in the water lines and is sandwiched by the radially slitted copper. In practice it was found that the valve was only opened during the initial flush and that the steady state, low pressure argon flow used during furnace operation just made up for leakage. (The startup checklist for the furnace, including the empirically deduced gas flush requirements, is given in Appendix B.) The circular window at the underside of the furnace was obtained as surplus from within Lockheed Sanders. Based upon a transmission test, it is believed to be a spinal-type material, with a dip in transmissivity to about 12% at a wavelength of approximately 2.72  $\mu\text{m}$ . (By comparison, the peak output of the 1040 K heatpipe should be at about 3.5  $\mu\text{m}$ ). The window is sealed to the copper plate using a ring of alumina fiber rope.

#### 5.4.4 Instrumentation

Type K thermocouples were used except for measuring the center furnace temperature. That was performed by a W-5 Re/W-26 Re thermocouple in a molybdenum sheath, entering through the lower copper plate.

Water temperatures were measured at the exits of the upper and lower copper plates and at the work station and motor generator. (Water entering the work station also went through the induction coil). Water for all components passed first through a T-joint at the motor generator, and it is there that the entrance temperature was determined. Two thermocouples were located between the felt on the bottom copper plate and the alumina casting. Another entered at the top of the casting and extended down about 15.25cm (6") between it and the carbon felt outer insulator of the susceptor. Similarly, temperature was read between this outer insulator and the inner graphite one.

Signals from the thermocouples were carried via extension cable to the HP data logger, which provided material cold-point compensation resulting in direct read out of temperatures in  $^{\circ}\text{C}$  or  $^{\circ}\text{F}$ . The system could be adjusted to sample temperatures at up to one per second, and either print the output or show it on the screen.

The purpose of the IR camera was to view the absorber dome of the heatpipe during testing in order to monitor it for spots that would indicate wick dry out. (Such an event would necessitate quick removal of the heatpipe from the top of the furnace). The camera was a Lockheed Sanders owned AGA Thermovision, model 782 that used  $\text{LN}_2$  cooling, and it viewed the furnace interior via a gold plated front surface mirror. Although quantitative temperature readings from the camera would have been desirable, they would have been difficult to calibrate. A qualitative measure would have been sufficient to detect incipient evaporator failure.

Under normal operation the energy entering the camera from the dome would contain the combined effect of radiation (at an uncertain emissivity) and reflection (from the hottest surface of the furnace interior). While the latter contribution would not be uniform, it should be symmetric, thus, hot spots should be detectable, assuming that the camera is sufficiently sensitive. Nominally it can detect a variation of under 1% at  $300^{\circ}\text{C}$ . A very rough calculation (not integrated over frequency, but taken at the peak values only) shows that photon emission for a  $2000^{\circ}\text{C}$  temperature rise above  $1040\text{ K}$  would be about 6 % over the combined radiative and reflected background value (this also assumes  $\alpha = \epsilon = .66$ ). However, filtering required for the camera to view high flux would reduce its sensitivity.

#### 5.4.5 Qualification Testing

A series of tests were carried out to demonstrate the capability of the furnace to reach the required operating temperature of about  $2000\text{ K}$  and to check out the various parts. (These were done with a large amount of insulation covering the furnace opening). The first test was performed in conjunction with a technician from Encur Inc. to exercise the electrical system and check its ability to provide full rated power. Peak temperature reached was about  $1150\text{ K}$  but the furnace was not allowed to come to equilibrium.

In subsequent tests equilibria were reached at temperatures of  $1075$ ,  $1314$  and  $16950^{\circ}\text{C}$ , requiring power settings of  $10$ ,  $15$  and  $25\text{ kW}$  respectively; (the heat balance of the furnace is somewhat confusing and it is discussed below in a separate section).

Two possibly interrelated problems developed in the first tests with the original design that used fiberform boards as insulation sandwiching the upper copper plate and an open slit in this plate. Viewed through the mirror below, a 'hot spot' was seen on the insulation adjacent to the slit in the upper copper plate. Inspection of the fiberform boards showed corrosion had occurred along the slit line. One may hypothesize that induced current in the copper jumped the gap either by arcing or by going through the fiberform, producing locally higher temperature. An attempt was made to remedy the situation by opening the gap further and creating corresponding slits in the adjacent insulation boards. Each slit was then filled with Johns-Manville cerawool insulation. This time the fiberform started to burn slowly in the gap area and considerable damage occurred to the covering board. The fire extinguished itself

when the furnace temperature dropped sufficiently. To eliminate these problems all fiberform on top of the furnace was eliminated in favor of the oxide fiber blanket noted earlier.

We decided to test for the possibility of direct induction heating of the heatpipe. A stainless steel ring was set on top of the cold furnace, lying on a thin plastic board placed on the insulation. The objective was to use a ring similar in cross-section (and position relative to the furnace) to that of the ring originally planned to be used inside the heat pipe before we switched to the 'angle irons'. One thermocouple was inserted into a hole drilled into the ring and another put under the board and ring.

When the power to the furnace was turned to 25 kW (nominal on the meter) the result (Figure 5.23a) was that the ring core heated considerably faster than the area underneath it. Thus it was concluded that induction, rather than conduction, was the main source of heat to the ring. However, when the electrical conduction path around the copper plate was bridged and the test repeated, the temperature curves indicated that the opposite was true (Figure 5.23b). What occurred was that a current was induced in the copper plate that produced a magnetic field locally counteracting that from the main coil. It is recommended that a closed loop cooling plate be used to avoid direct induction heating of the heat pipe.

#### 5.4.5.1 Heat Balance of the Furnace

One of our objectives for the furnace was to determine its power losses as a function of core temperature, then to use this tabulation during heat pipe testing to determine heat pipe power performance. We also needed to see if the furnace would have sufficient power capability for our test goals.

To meet these objectives the furnace was operated with sufficient insulation covering the aperture to minimize losses there. Then, heat loss to the various cooling water lines was measured and checked with the power meter on the control station. (The induction coil itself absorbed essentially all the heat conducted from the side of the graphite susceptor; even at peak core temperature the side of the alumina casting only felt warm.)

According to Encur, (the induction system supplier) the power meter measured power into the induction coil, the cooling water of which also cooled the work station. Encur stated that the losses in the work station amounted to only a few percent of the total power, though in retrospect it might have been useful to try to separate this out in the cooling water measurements.

Table 5.8 shows the power measurements for three core temperatures. For two of the three cases the losses into the induction coil/ work station water line virtually match the settings on the power meter. However, the losses into the two cooling plates should also be a result of heat derived (by conduction or induction) from the main coil. Adding these in means that the losses exceed power read on the meter. In the third case we are closer to a match. Although some progress was made toward resolving this problem, time and cost constraints led to the pursuit of the alternative of using an IR thermometer to measure the radiant heat from the heat pipe.

It appears that there are about 53kW available for testing the heat pipe when the

**Inductive Heating Effect on Stainless Steel  
Rings (Open Loop on Copper Plate 11/21)**

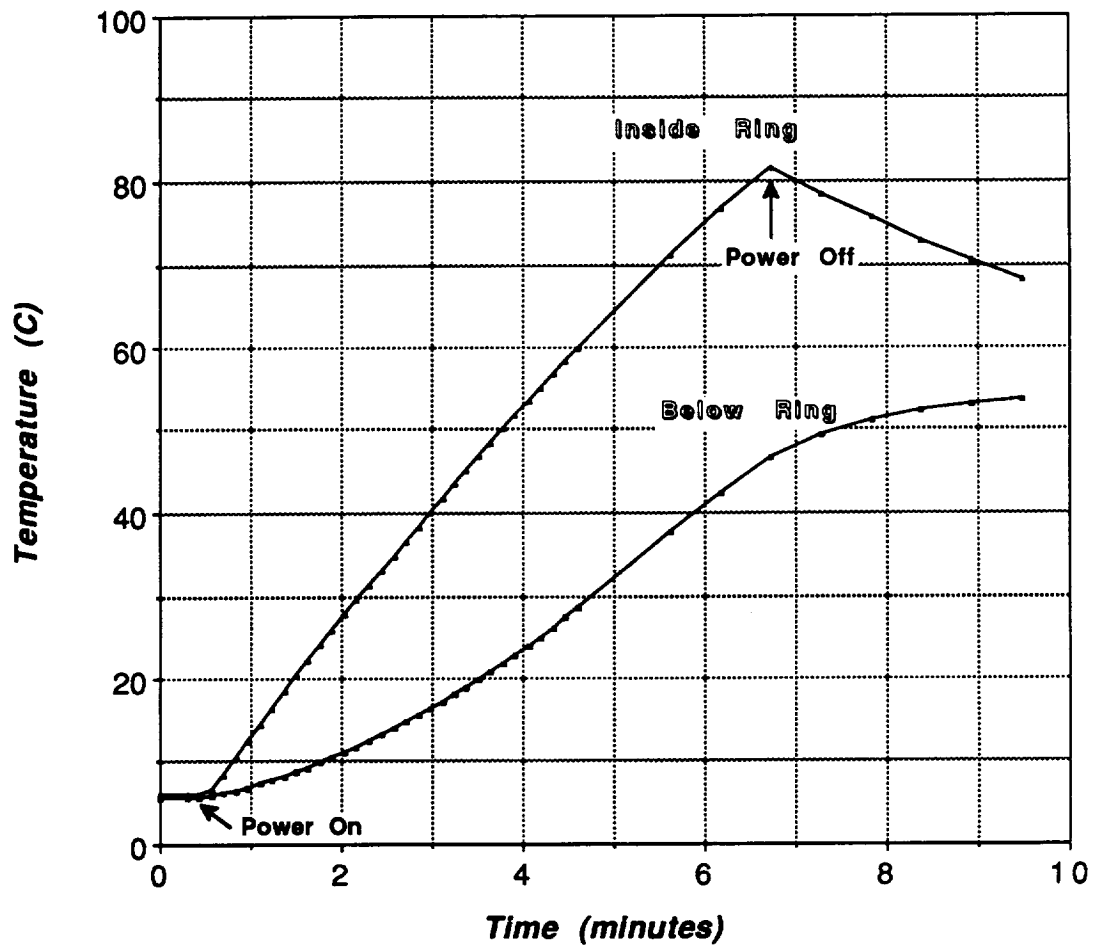


Figure 5.23a Inductive Heating Effect on Ring  
with Open gap on Copper Plate

Inductive Heating Effect on Stainless Steel  
Ring (Closed Loop on Copper Plate 11/22)

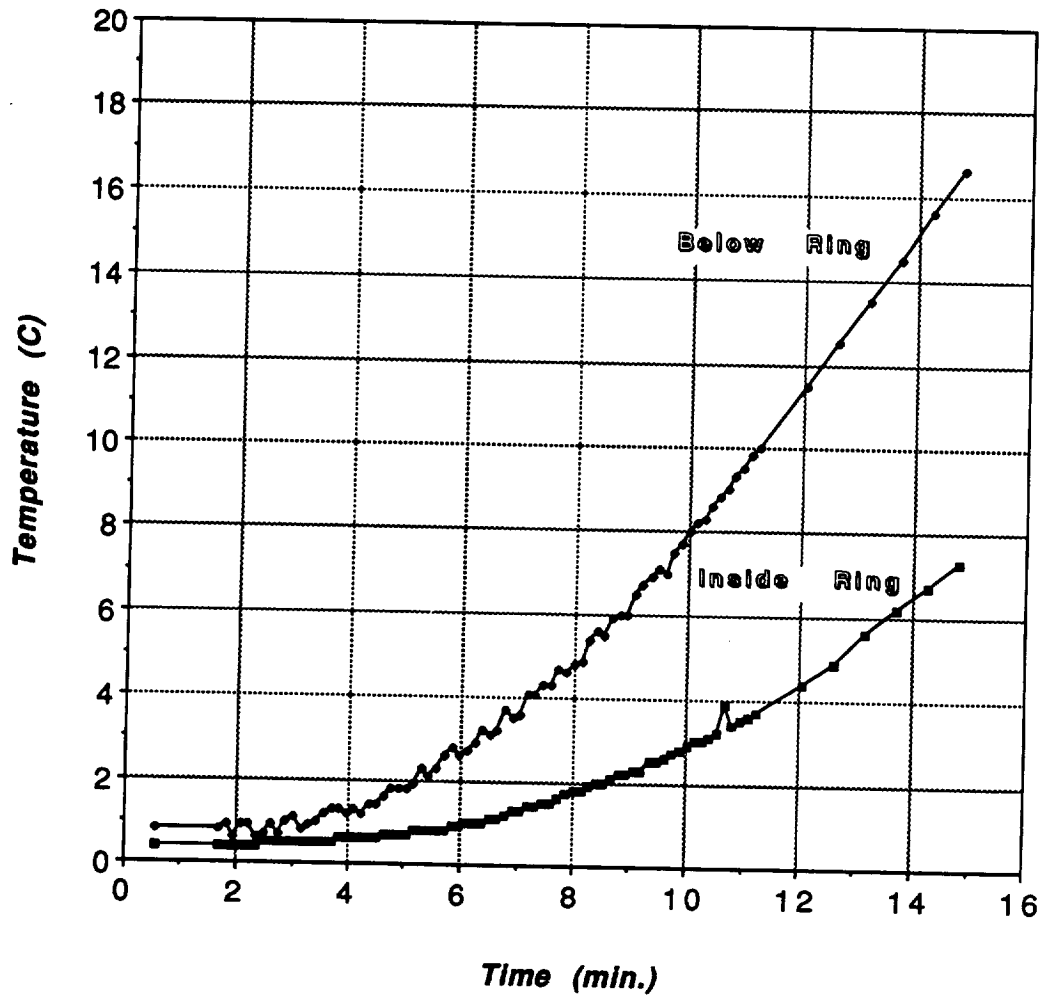


Figure 5.23b Ring Heating with Gap Closed on Copper Plate



Table 5.8 Furnace Power Measurements at Several Equilibrated Temperatures

(All water flow rates measured in GPM)

- a Core Temperature (Ar gas): 1695° C (1968K)  
Power on meter at control station: 25kW

Component	Cooling Water Temp (°C)		Temp Rise (°C)	Water Flow Rate		Power Dissipated (kW)
	In	Out		Cm <sup>3</sup> /sec	GPM	
Motor-Generator	10.0	12.4	2.4	1451	23	14.56
Work Station	10.0	20.7	10.7	567.8	9	25.40
Top Plate	10.0	23.9	13.9	82	1.3	4.7
Bottom Plate	10.0	14.4	4.4	105.3	1.67	1.94

32.10 Sub-Total without  
Motor-Generator  
46.65 TOTAL

- b Core Temperature (Ar gas): 1314° C (1587K)  
Power on meter at control station: 15kW

Component	Cooling Water Temp (°C)		Temp Rise (°C)	Water Flow Rate		Power Dissipated (kW)
	In	Out		Cm <sup>3</sup> /sec	GPM	
Motor-Generator	10.2	12.1	1.9	1451	23	11.52
Work Station	10.2	15.9	5.7	567.8	9	13.53
Top Plate	10.2	16.1	5.9	82	1.3	2.02
Bottom Plate	10.2	12.2	2.0	105.3	1.67	0.88

16.43 Sub-Total Without  
Motor-Generator  
27.95 TOTAL

- c Core Temperature (Ar gas): 1075° C (1348K)  
Power on meter at control station: 10kW

Component	Cooling Water Temp (°C)		Temp Rise (°C)	Water Flow Rate		Power Dissipated (kW)
	In	Out		Cm <sup>3</sup> /sec	GPM	
Motor-Generator	10.1	12.0	1.9	1451	23	11.52
Work Station	10.1	14.3	4.2	567.8	9	9.97
Top Plate	10.1	14.6	4.5	82	1.3	1.54
Bottom Plate	10.1	11.4	1.3	105.3	1.67	0.57

12.08 Sub-Total without  
Motor-Generator  
23.61 TOTAL

furnace is close to the previously calculated core temperature of about 2000K required for the nominal power throughput. Of course there would be some additional parasitic loss with the coil and motor-generator operating at a higher power level, even if the core temperature is unchanged; but it appears that this will not be critical. (It is unclear why the motor-generator loss increased between two of the cases shown but not between the other two, although it may just reflect inaccuracy in the measurement.) Raising the core temperature to push more power into the evaporator dome would of course increase the losses by conduction to the induction coil and cooling plates.

## 5.5 Planned Test Procedure

During the course of the program the objective was to develop a test procedure for the heat pipe that would accomplish our test goal at the lowest possible cost. Recall that the minimum objective was to operate the evaporator domes at least at the nominal power level of 38kW. The length of the heat pipe tube was set such that more than this amount would be lost by radiation alone at the nominal operating temperature of 1040K and an assumed emissivity of 0.7 (To dump just the nominal power at this emissivity requires a temperature of about 927K). The heat loss would then be regulated using the insulation shield, which was to slide up and down over the heat pipe.

Because of the difficulty encountered in obtaining consistent power use figures when comparing the power meters and the water lines, it had been intended to obtain better meters to independently check these figures. But the selected alternative to trying to untie this situation directly was to measure the heat pipe radiant loss using a separate IR thermometer viewing the cylinder surface and operated remotely from the control room. The actual emissivity of the surface would have been found by comparing the actual temperature, read from thermocouples on the cylinder, with that given by the IR thermometer at an assumed emissivity setting, and then adjusting that setting until the temperatures matched. The remaining problem would have been to account for convective heat losses. For the bare cylinder at 1040K natural convective losses (still air) may be a tenth that by radiation, but this could increase substantially if air currents were present in the room. Also, the insulation shield makes the analysis of these contributions more difficult.

The test scheme is illustrated in Figure 5.24. It consists of three basic phases:

### a) Startup

The insulation box fully covers the heat pipe (part a of the figure) as the power is turned on. Power is increased in small increments, each time allowing the thermocouples on the cylinder to reach equilibrium. When this equilibrium temperature is uniform, it is known that the cylinder is operating as a heat pipe. Power is raised until the uniform, equilibrium temperature reaches 927K. The surface of the dome is monitored using the underside IR camera. As in all phases of the test, if this camera shows a 'hot spot' the heating is aborted by triggering a 'scram' system that uses a counterweight to lift the heat pipe off of the furnace.



#### b) Rated Power Condition

The insulation box is moved up incrementally and in parallel the power is increased to maintain the temperature of the heat pipe. When the cylinder is fully exposed the side IR thermometer is used to check the emissivity using the method noted above. The power to the furnace (and consequently the pipe temperature) is adjusted until the combined loss by radiation (read from the camera) and by convection (if judged to be significant) meets the requirement of 38kW.

If the cylinder oxidizes rapidly enough that the emissivity quickly reaches the value of 0.7, the temperature of the cylinder will be below the nominal operating point of 1040K though the power level will be at 38kW. This condition may actually represent a more severe test of the sodium flow capability through the wick than at the nominal point since the liquid's viscosity goes up as its temperature goes down. On the other hand, the heat of vaporization also goes up with reduction in temperature, so the flow rate will be reduced. The thermal conductivity behaves similarly, so superheating across the wick is also lessened.

One way to test the evaporator at the nominal temperature as well as rated power would be to gradually lower the insulation shield over the cylinder until that temperature is reached, without changing the power setting on the furnace. Essentially this would be a test at both the nominal power and temperature, except that there would be some increase in parasitic losses in the furnace. This comes about since, at a given power setting, the furnace core temperature must rise to compensate for the dome's temperature increase, which radiates more energy back into the core.

#### c) Higher Power Conditions

Due to the power losses in the furnace and the uncertainties concerning them it is not certain just how much above the nominal power condition could be reached with the present equipment, but the almost doubling (about a factor of 1.85) of the flux level suggested earlier as a goal is clearly not attainable. If the power were available, the fully uncovered cylinder would have to be allowed to reach a temperature of 1079K to dump the energy (about 70kW) by radiation alone. At 1040K the uncovered cylinder would lose a total of 61kW by radiation.

A few notes on our safety measures are in order. Extreme care is required due to sodium's high reactivity with water, which produces hydrogen gas in a violent reaction. In air, sodium will spontaneously ignite at 120°C or less. The lab facilities were designed so that the furnace and instrumentation could be operated from an adjacent control room with a separate exit in case of emergencies. The only requirement for entering the test area would have been for a brief period every two hours to refill the reservoir of LN<sub>2</sub> that cooled the detector in the underside IR camera. The emergency 'scram' system, again operable from the control room, has already been mentioned. Finally, the heat pipe would normally operate at a sodium vapor pressure below atmospheric (about .35atm at 1050K), but this vapor pressure rapidly increases to 1 atm at just over 1150K, and given the dangers of sodium escape the temperature would not have been allowed to ever exceed this number.

Sodium melts at about 98°C, and as a consequence it is conceivable that at startup the fluid could evaporate from the wick and freeze out onto the cold upper walls of the cylinder. It is very unlikely that any substantial amount of sodium could freeze out before the entire cylinder were above the melting point. Nonetheless, an auxiliary

system for preheating the cylinder might be desirable. More realistically, such a system may be usefull when turning the cylinder around to test the other dome, since one wants to start out with the sodium pool at the dome being tested, and not have 'chunks' of melting sodium falling down from the other end.

## Chapter VI

### Conclusions

Regrettably, technical, cost and programmatic difficulties in this program prevented the completion of the primary tests planned. However, the preparatory steps for those tests resulted in several accomplishments:

1. A combination of theoretical evaluation and drop tower testing using single phase fluids suggested a configuration of phase change material containers that would likely prevent thermal ratcheting without the need for non-wetting surfaces. Zero-g testing with actual phase change is required to confirm this.
2. Effective and detailed procedures were developed to fabricate screen wicked sodium evaporator domes for the NASA advanced stirling receiver. Preliminary tests suggest a significant improvement in the quality of the resulting screen over previous work. The domes were designed to accommodate the required average heat flux at the focal point of the receiver without burnout.
3. A high temperature (2000K) induction furnace was designed, built and successfully tested to its nominal operating point. The furnace was to be used as a solar flux simulator in testing the evaporator domes.

The aforementioned difficulties in this program included the departure of two of the key personnel, which resulted in the necessity of the present author retracing the steps leading to the evaporator dome designs. As a result, the reasons for all the details of these designs may not have been fully explained here.

**Appendix A**  
**Letter on Electroforming Technique**

I wish to suggest two approaches which I feel confident will alleviate the problems:

1. If photo resist pattern is necessary prior to electroplated nickel bonding, follow the same procedure and substitute a sulfamic acid rinse for the water rinse prior to live (voltage pre-applied) entry into the nickel bath.
2. If a stike (very thin) nickel plate is permitted prior to photo resist application, activate the Inconel 617 and flash about 0.0005 inch of nickel as a bond layer on the substrate. This removes the rinsing entrapment caused by the photo resist pattern - particularly in regards to precipitates of the alloying metals such as molybdenum and chromium. Next, apply the photo resist and treat the substrate as "pure" nickel. Anodic treatment should be minimized due to the thinness of the nickel strike. Rinsing is not a serious problem in this process after the cathodic activation.

The criticality of the rinsing can be realized, if one considers the nature of nickel and nickel alloys such as Inconels. Nickel has good corrosion resistance, and it forms a relatively weak oxide layer in a short time span. Inconels are especially formulated to form strong protective oxide layers immediately as is the case with 300 series CRES alloys. Maintaining a reducing acid film on such materials between cathodic activation and the initiation of the plating process will inhibit oxide layer formation and assist in the formation of high integrity metallurgical bonding.

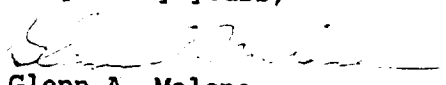
We would advise the conduct of a brief, yet concise, development effort whereby:

1. A more dependable and compatible bonding process be demonstrated and verified using the nickel preplate technique and/or the acidified post-cathodic rinse.
2. Improve the metal plate distribution and control by anode and cathode conformal box shields.

We also suggest improvements in electroform pattern cross-sectional profiles by high speed lapping processes rather than sanding or grinding. This will inhibit the formation of edge drag and subsequent fine burrs or distortions.

Your forwarding of test samples would initiate the aforementioned development effort.

Very truly yours,

  
Glenn A. Malone  
General Manager

GAM/sm



**Appendix B**  
**Checklist for Furnace Startup**

## Procedure / Checklist for Furnace (No Heatpipe)

### Prestartup:

- ☐ a. furnace sealed: window, plates
- ☐ b. gas exit valve open full
- ☐ c. thermocouples attached and working
- ☐ d. no shorting of thermocouple wires to frame or other parts
- ☐ e. two full Ar tanks available
- ☐ f. open full on insulation flush valve, closed on cavity flush
- ☐ g. turn Ar to 20 psi and flush 10 minutes
- ☐ h. open cavity flush valve
- ☐ i. turn Ar pressure to 5 psi
- ☐ j. flush 5 minutes
- ☐ k. close gas exit valve
- ☐ l. set Ar flow for 0.5" water

If IR camera to be used: ☐ is LN<sub>2</sub> available?

### Induction Startup:

- ☐ a. main and field switches off, field power pot at zero
- ☐ b. water on for all components: valve position      other: describe and record date
  - ☐ motor generator      full open
  - ☐ workstation
  - ☐ upper plate
  - ☐ lower plate
- ☐ c. set up ten second sampling on HP screen
- ☐ d. turn on main breaker
- ☐ e. turn on MG set at starter box: must wait 1 minute to turn on field coil
- ☐ f. print temperatures on HP
- ☐ g. turn on field
- ☐ h. set pot to desired power level
- ☐ i. start time

### Shutdown:

- ☐ a. field pot to zero
- ☐ b. field off
- ☐ c. MG off
- ☐ d. MG water off
- ☐ e. other water flows down ( exit temps not above 500C)
- ☐ f. check adequate gas for overnight cool down
- ☐ g. set HP to print out every half hour

## References

- 1 Baraona, Cosmo R. "Space Station Power System", Space Photovoltaic Research and Technology 1986: High Efficiency, Space Environment and Array Technology. Proceedings of a conference held at NASA Lewis Research Center, 7-9 October 1986, NASA CP-2475, 1986.
- 2 McKenna, R., Niggeman, R., and Thollot, P. "Solar Dynamic Power for Space Station" IECEC 84154, Proceedings of the Inter-Society Energy Conversion Engineering Conference.
- 3 Mendelson, I. ed., Design and Fabrication of Brayton Cycle Solar Heat Receiver., Final Report, NASA CR-72872. General Electric Nuclear Systems , Space Systems, Cincinnati, Ohio, July 1971.
- 4 Namkoong, D., Measured Performance of a 1089K (1500°F) Heat Storage Device for Sun-Shade Orbital Missions NASA TND-6665, February 1972.
- 5 Misra, Ajay K., and Whittenberger, J. Daniel, "Fluoride Salts and Container Materials for Thermal Energy Storage Applications in the Temperature Range 473 to 1400K", NASA TM-89913, N87-24026, 22nd Inter-Society Energy Conversion Engineering Conference, August 10-14, 1987.
- 6 Lurio, Charles A., The Feasibility of Using MgF<sub>2</sub> for Phase Change Heat Storage in a Spacecraft Solar Thermal Power System, Ph.D. Thesis, Massachusetts Institute of Technology, July 1988.
- 7 Kesseli, James B., Saunders, Roger I., and Batchelder, G., The Advanced Heat Receiver Conceptual Design Study, Final Report. NASA CR-182177, October 1988.
- 8 Harrison, R.W., and Hendrixson, W.H., Compatibility of Columbium Base Alloys with Lithium Fluoride, NASA CR-1526, General Electric Company Space Division, Cincinnati, Ohio, March 1970.
- 9 Misra, A. K., Whittenberger, J. D., Identification of Salt - Alloy Combinations for Thermal Energy Applications in Advanced Solar Dynamic Power Systems, NASA TM-88889, 1986.
- 10 Adkins, Douglas R. Analysis of Heat Pipe Receivers for Point Focus Solar Concentrators, Sandia Report SAND-88-0093, Sandia National Laboratories, Albuquerque, NM, October 1988.
- 11 Dunn, P.D., and Reay, D.A., Heat Pipes , Third Edition, Pergamon Press, Oxford, 1982.
- 12 Vargaftik, N.D., Theories on the Thermophysical Properties of Liquids and Gasses Second Edition, Hemisphere Publishing Company, Washington DC, John Wiley and Sons, New York, 1975.
- 13 Wichner, R.P., et. al., Thermal Analysis of Heat Storage Canisters for Solar Dynamic Space Power System, Manuscript submitted for presentation at the ASME Solar Energy Division Conference, Golden, Colorado, April 10, 1988.
- 14 Shankar, N. and Subramanian, R. Shankur, "The Stokes Motion of a Gas Bubble

Due to Interfacial Tension Gradients at Low to Moderate Marangoni Number"  
Journal of Colloid and Interface Science, Vol. 123, No. 2, June 1988.

- 15 Weingartner, S., Blumenburg, J. and Lindner, F. "Space Power Thermal Energy Storage - Planned Experiments for Phase Change Material Tests in Microgravity" Space Power Vol. 8, Nos. 1 and 2, 1989.
- 16 Concus, Paul and Finn, Robert, "Continuous and Discontinuous Disappearance of Capillary Surfaces", Variational Methods for Free Surface Interfaces, Concus and Finn, Eds, Springer - Verlag Inc., 1987.
- 17 Myshkis, A. D. et al, Low Gravity Fluid Mechanics, Springer-Verlag, Berlin, 1987, (Translation of Gidromekhanika Nevesomosti, Nauka, Moscow, 1976.)
- 18 Siegal, Robert and Howell, John R., Thermal Radiation Heat Transfer, Second Edition Hemisphere Publishing Corp, New York, 1981.
- 19 Touloukian, Y. S. et al, Thermal Conductivity, Metallic Elements and Alloys, Plenum Publishing Company, New York, 1970.
- 20 Adkins, Douglas R. "Measuring Flow Properties of Wicks for Heat Pipe Solar Receivers", Proceedings of the 12th Annual ASME Solar Energy Conference, April 1-4, 1990, Miami, Florida.
- 21 Touloukian, Y.S. et al, Thermal Expansion - Metallic Elements and Alloys, Plenum Publishing Corp., New York, NY, 1975.
- 22 Rohsenow, Warren M., Harnett, James P. and Ganic, Ejup N., eds., Handbook of Heat Transfer Fundamentals, Second Edition, MacGraw-Hill, New York, 1985.
- 23 Lemke, Charles H., "Sodium and Sodium Alloys", Kirk-Othmer Encyclopedia of Chemical Technology, Third Edition, Volume 21, John Wiley & Sons, Inc., New York, 1983 pp 181-204.